CHARACTERIZATION AND MODELLING OF SAGCM InP/InGaAs AVALANCHE PHOTODIODES FOR MULTIGIGABIT OPTICAL FIBER COMMUNICATIONS

by

Changlin (Forrest) Ma

B.Sc. Peking University 1984

M.Sc. The University of British Columbia 1987

THESIS SUBMITTED IN PARTIAL FULFILMENT OF
THE REQUIREMENTS FOR THE DEGREE OF
DOCTOR OF PHILOSOPHY

in the School
of
Engineering Science

SIMON FRASER UNIVERSITY

April 1995

APPROVAL

Name: Changlin (Forrest) Ma

Degree: Doctor of Philosophy (Engineering Science)

Title of Thesis: **Characterization and Modelling of SAGCM InP/InGaAs Avalanche Photodiodes for Multigigabit Optical Fiber Communications**

Examining Committee:

Dr. V. Cuperman
Chair, Professor
School of Engineering Science
Simon Fraser University

Dr. M. J. Deen
Senior Supervisor, Professor
School of Engineering Science
Simon Fraser University

Dr. R. H. S. Hardy
Senior Supervisor, Professor
School of Engineering Science
Simon Fraser University

Dr. S. Stapleton
Supervisor, Associate Professor
School of Engineering Science
Simon Fraser University

Dr. M. Thewalt
Supervisor, Professor
Department of Physics
Simon Fraser University

Dr. M. Parameswaran
Internal Examiner, Assistant Professor
School of Engineering Science
Simon Fraser University

Dr. M. Svilans
External Examiner, Scientific Staff
Advanced Technology Laboratory
Bell Northern Research, Ottawa

Date Approved: 10 April 1995

PARTIAL COPYRIGHT LICENSE

Title of Thesis/Project/Extended Essay

"Characterization and Modelling of SAGCM InP/InGaAs Avalanche Photodiodes for Multigigabit Optical Fiber Communications"

Author:

(signature)

Changlin (Forrest) Ma
(name)

April 10, 1995
(date)

ABSTRACT

In this thesis, an extensive investigation on a state-of-the-art photodetector, planar separate absorption, grading, charge, and multiplication (SAGCM) InP/InGaAs avalanche photodiode (APD) with partial charge sheet in the device periphery is conducted.

First, a simple, innovative, and non-destructive technique for extracting two critical device parameters, multiplication layer thickness x_d and integrated areal charge density σ_{charge}, is invented. Both x_d and σ_{charge} are crucial for the SAGCM APDs to meet the design requirements, and both vary significantly over a wafer with available fabrication technology. The technique involves innovative uses of punchthrough and breakdown voltages obtained from DC photocurrent measurements. The systematic uncertainties, arising from the neglect of ionizations in the absorption and charge layers, and from different ionization rates in InP reported in the literature, are considered in detail. The random errors caused by uncertainties from experiments and other device parameters are also investigated. The combined error for x_d is $< \pm 0.05$ μm, and for σ_{charge} is $< \pm 3\%$. The technique is verified by other independent measurements.

Second, a general theoretical model for the temperature dependence of the breakdown voltage V_{br} in any type of InP-based APD is developed. The experimental results show that V_{br} for the SAGCM InP/InGaAs APDs is approximately a linear function of temperature from -40 °C to 110 °C, with a temperature coefficient η_{exp} between 0.13 and 0.16 V/°C. The physical model developed also predicts that V_{br} indeed varies linearly with temperature, and the temperature coefficient η_{the} is 0.155 V/°C. In addition, the model successfully explains the small variation of η_{exp} among the SAGCM APDs. Good agreement between the physical model predictions and published experimental results for InP-based APDs is also obtained.

Thirdly, photogain (M) versus bias voltage (V) characteristics are studied both experimentally and theoretically. The photogain is shown to be self-calibrated, which makes it possible to compare theory and experiment in any InP-based APDs accurately for the first time. An empirical formula for Si and Ge APDs is proved appropriate for the InP/ InGaAs SAGCM APDs. The calculations of the M-V characteristics and its temperature dependence based on a physical model were in good agreement to the experimental results.

Finally, dark current low frequency noise (LFN) is also investigated. It is found that the dark current multiplication shot noise is proportional to M^{γ} with γ from 2.75 to 2.95. Flicker noise is also observed in some of the SAGCM APDs and it is believed to be due to leakage currents from surface/interface imperfections/defects.

DEDICATION

To my dear wife Jing and my loving parents

ACKNOWLEDGEMENTS

It is a pleasure to express my deepest appreciation to my senior supervisor Prof. M. J. Deen for his encouragement, suggestion, patience, and constructive criticisms. He has gone extra miles to set up this very interesting and challenging project for me, and provided invaluable advice and guidance throughout this research.

I owe a special debt to Dr. L. E. Tarof of Bell-Northern Research (BNR), for providing the devices, their detailed information, and numerous in-depth technical discussions. As a leading expert in this field, he shared with me many of his exciting ideas and deep understandings, which makes it possible for me to finish this thesis in less than 3 years. Mr. J. Yu of BNR has also made many valuable contributions to this thesis, and is highly appreciated.

I also would like to thank my co-senior supervisor Prof. R. H. S Hardy, who was instrumental in giving me this academic opportunity. His understanding, guidance, and encouragement are greatly acknowledged.

I wish to thank other members of my supervisory committee Prof. S. Stapleton for guidance and encouragement, and for reviewing the manuscript carefully, and Prof. M. Thewalt for constructive questions and suggestions. I also wish to thank Prof. A. Parameswaran for being the internal examiner, Dr. M. Svilans of BNR for being the external examiner, and Prof. V. Cuperman for chairing my thesis examining committee.

Special thanks are due to Prof. C. Bolognesi and Mr. S. Whitemore for reviewing the manuscript carefully and making many valuable suggestions. Thanks are also due to my colleagues during this project, the other members of the Prof. M. J. Deen's research group - A. Raychaudhuri, Z. X. Yan, J. Chen, T. Hardy, P. Kolev, W. Kwan, J. Liang, M. Margarit, and X. J. Zhao for their valuable comments during our biweekly group meeting.

I would like to thank BNR organization, and in particular the management - Drs. G. Chik and G. Ribakovs, for making it possible for me to conduct this project in collaboration with BNR.

I am specially indebted to the help received from Mr. J. Yu, Mr. D. McGhan, and Ms. K. Fox during my 1993 summer visit to BNR. I also would like to thank other members of Advanced Technology Laboratory, specially to Mr. T. Baird, Mr. R. Bruce, Dr. D. G. Knight, and Dr. M. Gallant.

Finally, I owe a debt of gratitude to my wife Jing for her patience and understanding. A mere "thank you" really cannot make up for the hardship she suffered during this period.

The financial support from Centre of System Sciences (CSS) of SFU, Simon Fraser University, Natural Science and Engineering Research Council (NSERC) and Micronet is acknowledged.

TABLE OF CONTENTS

LIST OF TABLES

LIST OF FIGURES

LIST OF ACRONYMS

AGC	automatic gain control
APD	avalanche photodiode
BER	bit-error rate
C-V	capacitance-voltage
DD	direct detection
EDFA	Eribium-doped fibre amplifier
E/O	electrical to optical
GBW	gain-bandwidth product
GR	generation-recombination
HBT	heterojunction bipolar transistor
HEMT	high electron mobulity transistor
IM	intensity modulation
IR	infrared
LED	light emitting diode
LFN	low frequency noise
MESFET	metal-semiconductor field field transistor
MOCVD	metal-organic chemical vapor deposition
MQW	multiquantum well
MSM	metal-semiconductor-metal
NRZ	non-returned to zero
O/E	optical to electrical
OEIC	optoelectronic integrated circuit
PIN	p-i-n photodiode
PLEG	preferential lateral extended guard
PMMA	polymethyl-methacrylate
PMT	photomultiplier tube
RF	radio frequency
RIE	reactive ion etching
SAM	separate absorption and multiplication
SAGCM	separate absorption, grading, charge, and multiplication

SAGM	separate absorption, grading, and multiplication
SIMS	secondary ion mass spectroscopy
SL	superlattice
SNR	signal to noise ratio
WCE	wet chemical etching

LIST OF SYMBOLS

B	bit rate
D_c	chromatic dispersion of optical fibre
D_m	material dispersion parameter
D_n	electron diffusion coefficient
D_p	hole diffusion coefficient
E_g	bandgap energy
E_i	threshold energy for impact ionization
E_{io}	threshold energy for impact ionization at 0 kelvin
E_r	average optical phonon energy
E_{ro}	optical phonon energy at 0 kelvin
F	excess noise factor (Chap. 2)
F	electric field
F_{br}	electric field in the multiplication layer at breakdown
F_{end}	electric field at the interface between the buffer and substrate layers at breakdown
F_{heter}	electric field at the heterointerface between the grading and boost layers at breakdown
F'_{heter}	electric field at the heterointerface between the boost and absorption layers at breakdown
F_n	excess noise factor in the case of pure electron injection
F_p	excess noise factor in the case of pure hole injection
I_d	dark current
I_{diff}	diffusion dark current
I_{do}	primary dark current
I_{du}	un-multiplied leakage dark current
$I_{g\text{-}r}$	GR dark current
I_p	photocurrent

I_{po}	primary photocurrent
J_n	electron current density
J_p	hole current density
k	k-factor in the excess noise formula
k_{eff}	k-factor in the excess noise formula in the case of electron injection
k'_{eff}	k-factor in the excess noise formula in the case of hole injection
L	repeater spacing
M	multiplication (gain, photogain)
$\overline{M}$	average multiplication
M_n	multiplication in case of pure electron injection
M_p	multiplication in case of pure hole injection
n	refraction index
n_i	intrinsic carrier density in semiconductor
N_D	doping concentration in the absorption and multiplication layers
N_G	doping concentration in the grading layer
N_{InGaAs}	doping concentration in the boost layer
$\overline{P}_{rec}$	average receiving power of an optical receiver for a certain BER
$\overline{P}_{tr}$	average transmitting power of an optical transmitter
r	power coefficient in the Miller formula
R	responsivity
S_f	noise power in A^2/Hz

t_{absorp}	thickness of the absorption layer
$t_{grading}$	thickness of the grading layer
t_{InGaAs}	thickness of the boost layer
t_{InP}	thickness of the charge layer
t_{mesa}	etching depth in the periphery region
$t_{undoped}$	thickness of the unintentionally doped layers (the buffer and absorption layers)
T	temperature
V	bias voltage
V_{ann}	bias voltage at which the electric field starts to penetrate the boost layer in the periphery region
V_B	theoretical breakdown voltage
V_{bi}	build-in voltage
V_{br}	experimental breakdown voltage
$V_{depleted}$	bias voltage at which the buffer layer is completely depleted
V_M	bias voltage at which the multiplication is M
V_{mesa}	bias voltage at which the electric field starts to penetrate the boost layer in the central active region
V'_{mesa}	bias voltage at which the electric field starts to penetrate the absorption layer in the central active region
x_j	p^+ diffusion depth
x_d	thickness of the multiplication layer
y_{active}	the diameter of the active region in our APDs

α	impact ionization for electrons
α_1	impact ionization for electrons in InP
α_2	impact ionization for electrons in InGaAs
β	impact ionization for holes
β_1	impact ionization for holes in InP
β_2	impact ionization for holes in InGaAs
α_{dB}	attenuation coefficient in decibels in optical fibre
γ	power coefficient in the multiplication noise formula (Chap. 7)
λ	optical wavelength (Chaps. 1 & 2)
λ	carrier free path (Okuto-Crowell theory)
λ_c	optical long cut-off wavelength
σ	rms spectral width of an optical pulse
σ_λ	rms spectral width of an optical source
η	quantum efficiency
η_{exp}	experimental absolute temperature coefficient of breakdown voltage
η_{the}	theoretical absolute temperature coefficient of breakdown voltage
σ_{active}	integrated areal charge density in the charge, grading and boost layers in the active region
$\sigma_{periphery}$	integrated areal charge density in the charge, grading and boost layers in the periphery region
σ_{charge}	integrated areal charge density in the charge layer
$\sigma_{grading}$	integrated areal charge density in the grading layer
σ_{InGaAs}	integrated areal charge density in the boost layer
τ	carrier transit time
τ_n	electron lifetime in p-type semiconductor
τ_p	electron lifetime in n-type semiconductor
ζ	relative temperature coefficient of breakdown voltage

Chapter 1 Introduction

In this thesis, I describe extensive characterization and modeling of a specific type of state-of-the-art InGaAs/InP avalanche photodiode (APD), utilized in current and future multigigabit optical fibre fiber communication systems. In this chapter, a short introduction to optical fibre communications [1][2][3] is given by considering the general system architecture, the major advantages over other technologies, and the historical developments of the technology. The general design requirements for optical receivers are discussed. Finally, the motivations of this investigation and the outline of this thesis are presented.

1.1 Optical fibre communications

1.1.1 General system

An optical fibre communication system as shown in Figure 1.1 is similar in its basic concept to any type of communication systems (i.e., its purpose is to convey the signal from the information source to the destination). In an optical fibre communication system, the information signal is converted from electrical form to optical form (E/O) by modulating an optical carrier of an optical source, such as laser or light emitting diode (LED). Then the signal is transmitted through an optical fibre that can be as long as few hundred kilometers; finally it is converted back into electrical form (O/E) by an optical receiver.

In an electrical communication system, the optical transmitter and receiver in the optical fibre communication system are replaced with an electrical transmitter (modulator) and receiver (demodulator), respectively. The modulator converts the information signal into a form of propagation suitable to the transmission medium, such as a pair of wires,

coaxial cable, or RF/microwave link. The demodulator transforms the modulated signal into the original information signal.

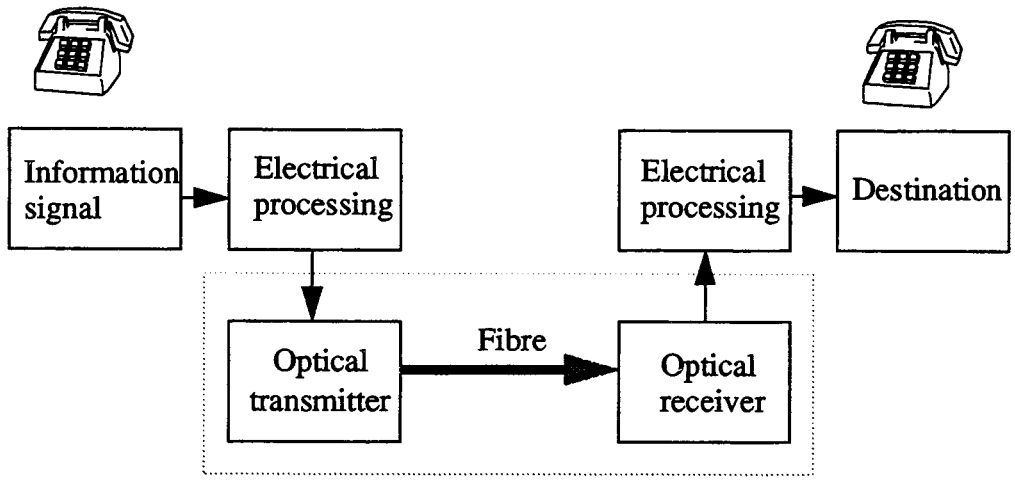

Figure 1.1 An optical fibre communication system.

Optical fibre communications use the superb advantages of optical fibre, mainly low attenuation and huge bandwidth. The optical fibre is made of silica glass with the optical refractive index being slightly lower in cladding than in core, resulting in light propagation in the core through total internal reflection. Generally speaking, an optical fibre can support many propagation modes. With reduced core diameter and other optimizations, monomode fibres, which have better characteristics than multimode fibres, can be fabricated, and they are the most popular fibres for long-haul optical fibre communications. In monomode optical fibres, the dominant mechanism of attenuation is impurity scattering within the 1.0 - 1.6 μm wavelength range. With advancements in impurity control of optical fibres, today's commercial monomode optical fibres have almost achieved the theoretical attenuation limit of ~ 0.16 dB/km at 1.55 μm. Optical fibre communications benefit from an inherently huge bandwidth since the frequencies of the optical carriers are in the order of 10^{14} Hz. Since the wavelengths for zero dispersion and lowest attenuation in reg-

ular (standard) optical fibers are 1.3 μm and 1.55 μm respectively, then most optical fiber communication systems operate at either of these two wavelengths.

Optical fibre communication may be either analog or digital (binary), as in the case of electrical communication. Analog optical fiber communication is limited to applications of short distance and lower bandwidth, such as cable TV. Compared to digital optical fiber communication, analog optical fiber communication is less efficient; that is, a far higher signal to noise ratio (SNR) is required and thus is difficult to achieve due to the inherent quantum noise associated with photon statistics. For example, the required SNR for cable TV is 40 dB. In addition, the linearity required for analog modulation is not readily provided by semiconductor optical sources, especially at higher frequencies. The unavoidably high quantum noise and vast wide bandwidth available in fibre optics make the digital format a natural choice. Historically, the installation of optical fibres followed the process of digitizing telephone systems.

Optical carrier modulation is in the form of intensity modulation (IM), in which the intensity of the optical carrier is modulated by the power of the information signal pulse, and accordingly, optical detection is in the form of direct detection (DD). The more sensitive method of coherent modulation and detection still faces some technical difficulties, and at present it is not economical. In this thesis, unless otherwise specified, a digital, IM/DD, and long haul (with repeater spacing up to 100 km) optical fibre communication system is assumed.

1.1.2 System considerations

In long-haul digital optical fibre communication systems, repeaters are used along the communication route to regenerate optical pulses in order to extend the communication distance. Similar to digital electrical communications, the major system considerations for

optical fibre communications are bit rate B and repeater spacing L. Depending on the operating wavelengths (0.85, 1.3 or 1.55 μm), B and L are limited either by attenuation or dispersion.

An optical pulse propagating in an optical fibre loses power because of attenuation. Optical output power P_{out} from a fibre of length L (km) can be related to input power P_{in} by

$$P_{out} = P_{in} 10^{-(\alpha_{dB} L)/10}, \tag{1.1}$$

where α_{dB} is the attenuation coefficient in decibels (dB/km). Considering an optical transmitter with maximum average power $\bar{P}_{tr}$ (mW) and an optical receiver with sensitivity $\bar{P}_{rec}$ (mW), which is proportional to B, the maximum repeater distance L limited by attenuation is given by

$$L = \frac{10}{\alpha_{dB}} \log \frac{\bar{P}_{tr}}{\bar{P}_{rec}}. \tag{1.2}$$

An optical pulse, which is unavoidably chromatic, also spreads out in transmission since the spectral power of the optical pulse associated with different wavelengths travels with different speeds (medium dispersion). In regular monomode optical fibres, one of the dominant dispersion mechanisms is material dispersion caused by the variation of refractive index n with wavelength λ, and this is quantified by the material dispersion parameter $D_m = \frac{\lambda}{c}\left|\frac{d^2 n}{d\lambda^2}\right|$ where c is the speed of light. Another dispersion mechanism is waveguide dispersion caused by the propagation of a significant fraction of the optical power in the cladding. The combination of these two dispersions is called chromatic dispersion D_c. For an optical source with root mean square (rms) spectral width σ_λ, the rms pulse broadening σ after transmitting a distance L is given by

$$\sigma = \sigma_\lambda L D_c. \tag{1.3}$$

The maximum bit rate B due to chromatic dispersion can be estimated from $B = 1/4\sigma$,

therefore the repeater distance L is limited by dispersion, and it is given by

$$L = 1/4\sigma_\lambda B D_c. \tag{1.4}$$

It is obvious that the bit-rate•distance product, B•L, is independent of both B and L.

If σ_λ is so small that the limiting rms spectral width is due to finite time duration of the optical pulse, then the minimum value of σ is given by [3]

$$\sigma = \lambda\sqrt{\frac{D_c L}{2\pi c}}. \tag{1.5}$$

Therefore

$$L = \frac{\pi c}{8\lambda^2 D_c B^2}, \tag{1.6}$$

and in this case B^2•L rather than B•L is independent of both B and L.

Table 1.1 Component parameters of optical fibre communications at 1.3 and 1.55 μm.

λ (μm)	α_{dB} (dB/km)	D_c (ps/nm·km)	$\overline{P}_{tr}$ (dBm)	$\overline{P}_{rec}$ (dBm)[a]	σ_λ (nm)
1.3	0.4	2	0	-40	0.25
1.55	0.25	15	0	-40	0.03[b]

a. At 1 Gb/s.
b. External modulated.

Using typical values of previously described parameters in Table 1.1, and eqn. (1.2), eqn. (1.4) or eqn. (1.6), the attenuation limits and dispersion limits on the repeater spacing L as a function of the bit rate B for regular monomode optical fibres at 1.3 and 1.55 μm wavelength are displayed in Figure 1.2. The attenuation and dispersion are limiting factors at bit rates lower and higher than 5 Gb/s, respectively. If the laser is directly modulated at 1.55 μm, D_c will be ten times larger than when it is externally modulated, and the attenuation would be the limiting factor even at 0.5 Gb/s. Note that the above calculations are estimates only, and power budget and rise time analysis are required for detailed system design.

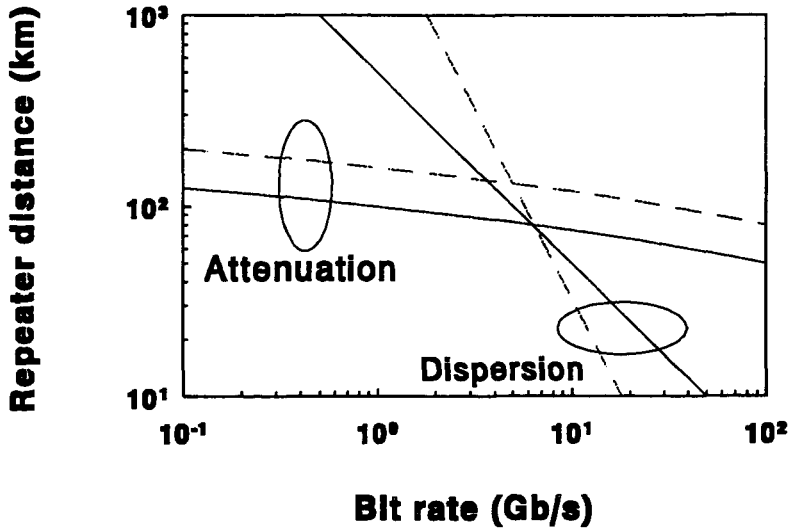

Figure 1.2 Repeater spacing versus bit rate using distributed feedback lasers and regular monomode optical fibres. The solid lines are for 1.3μm, and the dashed lines for 1.55 μm.

1.1.3 Historical perspective

Kao and Hockham [4] in 1966 may be credited for having laid the foundation for modern optical fibre communications even though the attenuation of optical fibres was 1000 dB/km at visible wavelengths at that time. The attenuation was successfully reduced to 20 dB/km by 1970, and to 2 dB/km by 1975 for visible wavelengths (0.85 μm). By the mid-1980s, optical fibres having attenuation less than 0.4 dB/km at 1.3 μm and less than 0.25 dB/km at 1.55 μm were commercially available. These three wavelengths (0.85, 1.3 and 1.55 μm) with lower attenuation are so-called first, second, and third transmission windows, and they were used by first, second, and third generations of optical fibre communication systems, respectively.

The first generation optical fiber systems used multimode fibres with core diameter of 50 μm, GaAlAs-GaAs lasers as sources operating at 0.85 μm and Si APDs as detectors.

Such systems have been installed since 1980, but were obsolete by the mid-1980s. The bit rate used was up to 150 Mb/s with the repeater spacing up to 10 km.

The second and third generation systems used monomode fibres, InGaAsP-based lasers as sources operating at 1.3 μm or 1.55 μm, respectively, and InGaAs/InP PINs or APDs as detectors. Such systems have been used exclusively since 1985 in all high capacity, long-haul, trunk route over-continental and underwater communication systems. The bit rate is up to 2.5 Gb/s with the repeater spacing up to 80 km.

A fibre amplifier uses rare-earth ions to dope the fibre core as gain medium. Erbium-doped fibre amplifiers (EDFAs) with high gain and low noise at 1.55 μm were demonstrated in 1987 [5][6]. This development has revolutionized the field of optical fibre communications. The attenuation at 1.55 μm is not a serious design problem where EDFAs are utilized, even for underwater multigigabit communication systems, and the repeater spacing is dispersion-limited. One expensive option for reducing dispersion at 1.55 μm, is to use dispersion shifted fibre (DSF), which has both minimum dispersion and minimum attenuation at 1.55 μm. Unfortunately, reliable fibre amplifiers with high gain and low noise operating at 1.3 μm remain to be demonstrated.

1.1.4 Major advantages of fibres over metallic transmission media

Here, the major advantages of optical fibres over metallic media are briefly discussed.

1. Huge bandwidth and low attenuation

   Light is a much higher frequency electromagnetic wave (10^5 GHz) than RF/Microwave (up to 10 GHz in coaxial cables). The attenuation is 10 to 20 dB lower than the popular RG-19/U coaxial cable at 500 MHz. It is easy to transmit over 100 km at 5 GHz, or over 300 km at 500 MHz in optical fibres without repeaters. By comparison, broadband coaxial cable systems restrict the trans-

mission distance without repeaters to only a few kilometers at a few hundreds of MHz.

2. Small size and weight

   Common optical fibre cables have cladding diameters of 125 μm (fibre core diameter from 10 μm to 100 μm) enclosed in a sheath with outer diameter of 2.5 mm, and the weight is 6 kg/km. By comparison, the RG-19/U coaxial cables have outer diameter 28.4 mm, and the weight is 1110 kg/km. Furthermore, the transmission capacity of the fibre cables is at least 100 times that of the coaxial cables.

3. Immunity to interference and crosstalk

   Optical fibres are dielectric waveguides and are therefore free from electromagnetic interferences. Since they have extremely small optical leakages, crosstalk between fibres is negligible even when many fibres are cabled together. The immunity to interference and crosstalk represents a major design advantage for optical fibre communication systems.

Additional advantages are electrical isolation, signal security, ruggedness and flexibility, reliability, and potential low cost. Optical fibre systems have totally dominated long-haul telecommunications since the early 1980s. Shorter distance communication systems are being gradually replaced by optical fibres.

The major disadvantages of optical fibre communication should also be mentioned. Due to the difficulty and cost of splicing fibres, and the high cost of O/E and E/O conversions, it is presently not economically viable to build local area networks and short distance communication systems with optical fibres. Because of the higher photon quantum

noise and non-linearity of optical sources, the applications of optical fibres in analog systems are limited at present.

1.2 Optical receivers

1.2.1 Design considerations

The most important design considerations for a receiver in (electrical or optical) digital communications are sensitivity and bandwidth. The sensitivity is conventionally defined as the minimum average received power $\overline{P}_{rec}$ required by the receiver to operate at a BER of 10^{-9}, where BER (bit-error rate) is defined as the probability of incorrect identification of a bit.

1.2.2 Components

A digital optical receiver consists of three sections as shown in Figure 1.3. The front end section, which is the critical part of the three sections, includes a photodetector, followed by a preamplifier. The photodetector converts the optical bit stream into an electrical bit stream. A photodetector with internal gain is beneficial in increasing the overall sensitivity of the optical receiver. A transimpedance amplifier is the best choice for the preamplifier since the transimpedance amplifier can provide both high gain and high bandwidth, and in this case, the stability of feedback loop at higher gains is the major design challenge. In contrast, the design of preamplifier using a voltage amplifier forces a trade-off between bandwidth and gain, and is therefore less attractive.

The linear channel section consists of a high gain main amplifier and a low pass filter. The main amplifier includes automatic gain control (AGC), which limits its average output power to a fixed level regardless of the optical input power at the photodetector. The

low pass filter shapes the electrical pulses to reduce noise and intersymbol interference (ISI).

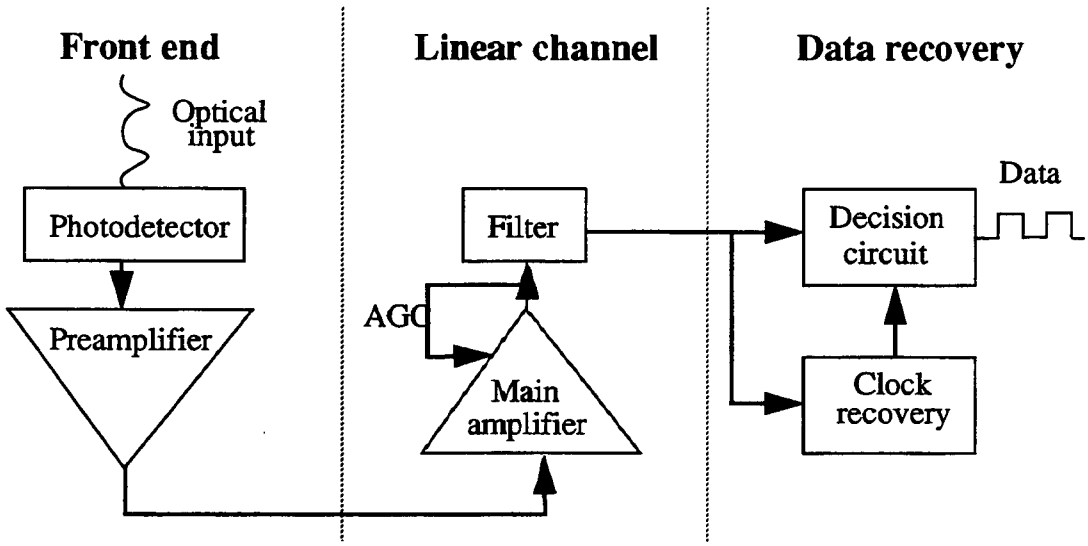

Figure 1.3 Diagram of a digital optical receiver.

The data recovery section is made up of a decision circuit and a clock recovery circuit. The decision circuit compares the output from the linear channel to a threshold level at sampling times determined by the extracted clock, and decides if the signal correspond to bit "1" or "0".

1.3 Motivation

Long-haul optical fibre communication systems necessitate high-performance optical receivers. One of the most critical components in the receiver is a high-performance photodetector. In this thesis, an extensive investigation is presented on such a state-of-the-art high performance photodetector, planar separate absorption, grading, charge, and multiplication (SAGCM) InP/InGaAs avalanche photodiode (APD), utilized in today and the near future commercial 1.3 or 1.55 μm optical fibre communication systems. In this thesis, comprehensive characterization and modelling, particularly DC and noise characteristics

and their temperature dependence, which have never been done before, are important parts of overall efforts to design, fabricate, characterize, model, and test the devices. The knowledge discovered here can also be used for other devices.

1.4 Thesis outline

In chapter 2, a review of the fundamentals of photodetectors is presented, including different types of photodetectors and the reasons why APD was selected. The fundamentals of APD are reviewed, followed by a brief account of its historical development. This leads to a discussion of the reasons why SAGCM InP/InGaAs APDs are the best choice as the photodetector in the intended optical fibre communication systems. In chapter 3, specific details of the devices are presented, including their structure, fabrication, and calibration.

In chapter 4, a simple, innovative, and non-destructive technique for extracting of two critical device parameters, multiplication layer thickness x_d and integrated areal charge density σ_{charge} in the charge layer, is described. The systematic uncertainties, arising from the neglect of ionizations in the absorption and charge layers, and from different ionization rates in InP reported in the literature, are considered in detail. The random errors caused by uncertainties from experiments and other device parameters are also investigated.

In chapter 5, the photogain (M) versus bias voltage (V) characteristic is studied both experimentally and theoretically. An empirical formula for Si and Ge is tested on the SAGCM InP/InGaAs APDs. A physics-based model is developed to theoretically calculate the M-V characteristics at room temperature for all the SAGCM InP/InGaAs APDs with different device parameters.

In chapter 6, a general theoretical model for the temperature dependence of breakdown voltage V_{br} in any type of InP-based APD (including the SAGCM InP/InGaAs APDs) is developed. The temperature dependence of breakdown voltage V_{br} from -40 °C to 110 °C in the SAGCM InP/InGaAs APDs with a range of device parameters is investigated. The temperature dependence of the M-V characteristics is also discussed.

In chapter 7, low frequency noise (LFN) in dark currents are also investigated experimentally. The dark current multiplication shot noise is determined experimentally as a function of dark current and multiplication gain M in a few SAGCM InP/InGaAs APDs. Flicker noise is also observed in some SAGCM InP/InGaAs APDs, and it can be related to surface/interface imperfections/defects.

A concise description of the specific achievements and accomplishments are summarized in chapter 8 of this thesis.

Chapter 2 Background

In this chapter, different types of photodetectors and their general operating principles are first briefly reviewed. This review highlights the reasons why APDs are a good choice for optical fibre communications. A detailed review of operating principles, structures, and calculations of major performance characteristics of general APDs follows. The chapter concludes with a brief description of the historical evolution of APDs, and the reasons why a specific structure APD, separate absorption, grading, charge, and multiplication (SAGCM) InP/InGaAs APD, is required for optical fibre communications.

2.1 Fundamentals of photodetectors

The most popular photodetectors, except avalanche photodiode (APD), are discussed in detail in the next three sections. Excellent general discussions of photodetectors can be found in many references, for examples, [1][7]. The comparisons of photodetectors for optical fibre communications are discussed in the references [8][9][10].

2.1.1 Photodetection

There are two distinct photodetection mechanisms. The first mechanism is external photoemission effect, typified by the photomultiplier tube (PMT). When the primary photocathode of a PMT is bombarded by photons, electrons are emitted if the energy of the incoming photons is larger than the work function of the photocathode. The emitted electrons are accelerated towards secondary electrodes (dynodes), where more electrons can be emitted by the impact from each incoming electron. This process is repeated for many stages, resulting in gains as high as 10^6. The PMT is not suitable for optical fibre communications because it is incompatible with microelectronic monolithic integration in these

systems, and there are no photocathode metals with a suitable work function for 1.3 - 1.6 μm wavelength light.

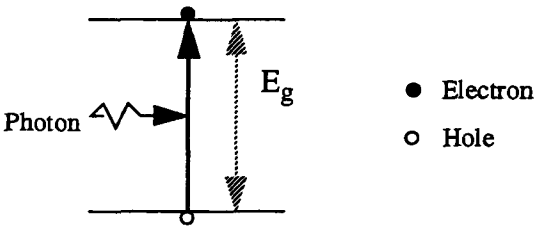

Figure 2.1 Internal photoemission - absorption.

The second mechanism is the internal photoemission effect (absorption) as shown in Figure 2.1. A photon with energy equal or larger than the bandgap energy of the semiconductor E_g can excite an electron and hole pair. Photodetectors based on internal photoemission effect are named solid state detectors since they are made of solid state materials, predominantly semiconductors. With good performance characteristics as well as simplicity, small size, ruggedness, compatibility to integration, semiconductor photodetectors are undoubtedly better choices than PMT or any other phototubes for visible and near infrared (IR) optical fibre communications. Semiconductor photodetectors can be classified further according to one of the following criteria: semiconductor material, device structure, and internal gain.

2.1.2 Performance characteristics

The major performance characteristics appropriate for all photodetectors are the following.

- Quantum efficiency and responsivity.

  The quantum efficiency η is defined as the ratio of the number of collected electron hole pairs (without gain) over the number of incident photons, and is

always less than 100%. η is determined by the absorption coefficient α, the surface reflection coefficient, and any other carrier recombination mechanisms occurring before collection. In common with α, η is a function of the photon wavelength.

A related but more often used figure of merit is responsivity $\mathcal{R}$. It is defined as the ratio of generated photocurrent, I_p, (without internal gain) over incident optical power, P_o, and it can be related to η using

$$\Re = \frac{I_p}{P_o} = \frac{\eta q \lambda}{hc}, \tag{2.1}$$

where q is the electron charge.

- Bandwidth.

  Electrical bandwidth is defined as the frequency of electrical signal at which the power of the electrical signal is 3 dB lower than its DC power.

- Gain.

  Gain is defined as the internal gain of the photodetector (i.e., the ratio of number of collected electron-hole pairs to the number of primary photogenerated pairs). Another popular name is multiplication gain (photogain), and they are used interchangeably in this thesis.

- Noise.

  Noise is defined as the fluctuation of the generated electrical signal and is described with corresponding rms values of current or voltage.

- Long cutoff wavelength.

  The photon energy with wavelength, λ, must be larger than the bandgap energy, E_g, (direct bandgap), that is, $hc/\lambda \geq E_g$. Thus the long cutoff wavelength, λ_c, is

$$\lambda_c = \frac{hc}{E_g}. \tag{2.2}$$

2.1.3 Device requirements

Being one of the crucial components which dictates the overall system performance in optical fibre communication systems, photodetectors must satisfy very stringent requirements for performance, compatibility, cost, and reliability.

- High sensitivity.

  The photodetectors are designed to detect weak optical signals of a specific wavelength. This demands high responsivity (quantum efficiency), low internal noise, and high multiplication gain (if applicable).

- Fast speed.

  The time delay in the conversion from electrical to optical forms should be minimum. In frequency domain, it means the electrical bandwidth should be adequate for the operating bit rate.

- High reliability and stability.

  The photodetector must maintain designed performance characteristics for many years in sometimes demanding environment. This requires better design and stringent fabrication quality for eliminating potential sources of degradation.

- Low cost.

  This normally means high yield in fabrication.

- High fidelity and dynamic range.

  For analog transmission, the photodetectors should be able to reproduce faithfully the received optical waveform over a wide range of optical power. This is not critical in digital applications.

A suitable photodetector must satisfy these requirements. Various type of photodetectors are examined in the following sections in order to select a suitable one.

2.2 Semiconductor photodetectors without internal gain

2.2.1 p-n photodiode

A p-n photodiode normally operates under reverse bias, and both the depletion and diffusion regions may absorb photons, which generate electron-hole pairs in proportion to the optical power, as shown in Figure 2.2. In the depletion region, the pairs are separated and drifted by the electric field. In the diffusion region, the pairs within a few diffusion lengths may slowly diffuse to the depletion region, and eventually generate some terminal current. The other pairs in the diffusion region recombine and generate no terminal current. Therefore, the depletion region should be wide enough to achieve high quantum efficiency. This also makes the p-n capacitance smaller to meet the high bandwidth requirement. However, the depletion region cannot be too wide since it would increase the drift time of the carriers through the depletion region, which results in reduced bandwidth. This exemplifies the compromise between quantum efficiency (gain) and speed (bandwidth) in all photodetectors.

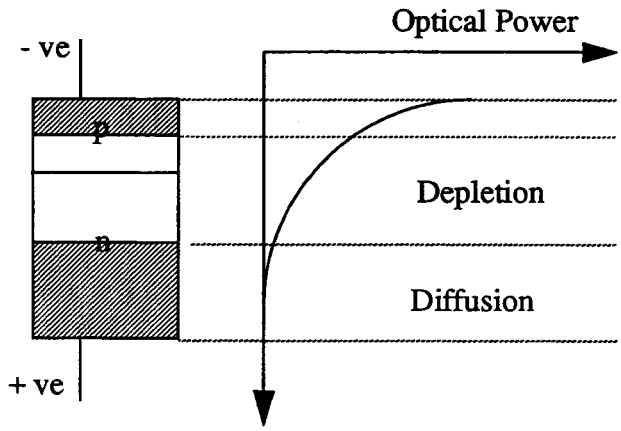

Figure 2.2 p-n photodiodes.

2.2.2 p-i-n photodiode

p-i-n photodiodes (PINs) as shown in Figure 2.3 have superseded p-n photodiodes, and are the most popular photodetectors without internal gain in optical fibre communications. p-i-n photodiodes are better than p-n photodiodes since they can be easily tailored for optimum quantum efficiency and bandwidth, and are relatively easy to fabricate, highly reliable, and of low noise. InGaAs/InP p-i-n photodiodes are most widely used, and have gained even more popularity after the breakthrough of the EDFAs.

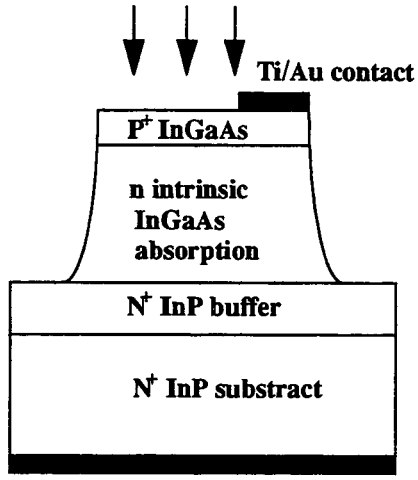

Figure 2.3 A front-illuminated InGaAs homojunction p-i-n photodiode.

Since all the generated carriers are in the depletion region (i region), the collection process is fast and efficient. Therefore, the intrinsic bandwidth is very high, and the overall bandwidth is usually limited by extrinsic effects up to a few tens of GHz. The p^+ InGaAs layer in homojunction p-i-n photodiodes, as shown in Figure 2.3, has to be thin to allow light to penetrate without severe loss. However, in this case, the strong surface recombinations impair the quantum efficiency. One solution is to open an optical window at the bottom of the substrate, and the p-i-n photodiode is back-illuminated rather than front-illuminated in this case (heterojunction), since InP is transparent to light with its

wavelength longer than 0.92 μm. Another solution is to replace the thin p^+ InGaAs layer with a thick p^+ InP layer (double heterojunction). Heterojunction p-i-n photodiodes with up to 30 GHz bandwidth and about 70% quantum efficiency are fabricated commercially.

2.2.3 Schottky-barrier photodiode

A Schottky-barrier photodiode as shown in Figure 2.4 is made of metal-semiconductor rectifying junction rather than the p-n junction in the case of p-n and p-i-n photodiodes. The Schottky-barrier photodiodes inherently have a very narrow active region, and are particularly useful in the visible and ultraviolet wavelengths due to their large absorption coefficients. Because of the short transit time, Schottky-barrier photodiodes can operate at frequencies as high as 100 GHz. One technical challenge is how to avoid surface traps and recombination centers, which cause substantial loss of generated carriers at the surface. In addition, the quantum efficiency is low, and there are no suitable metals for fabricating Schottky-barrier photodiodes operating in near infrared wavelengths. Therefore Schottky-barrier photodiodes are not suitable for optical fibre communications for wavelengths of current interest.

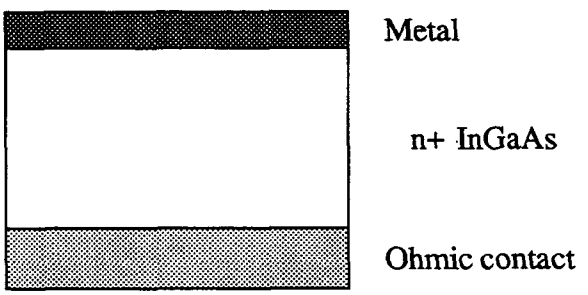

Figure 2.4 Schottky-barrier photodiode.

2.2.4 Metal-semiconductor-metal photodetector

A metal-semiconductor-metal (MSM) photodetector is a variation of Schottky-barrier photodiode (i.e., two Schottky contacts are made at the same side of the substrate). This results in easy fabrication and monolithic integration with other electronic devices, such as the metal semiconductor field effect transistor (MESFET), as demonstrated in Figure 2.5. The capacitance of an MSM photodetector is extremely small. However, it suffers similar limitations as a Schottky-barrier photodiode, and it is not widely used in optical fibre communications. As for optical receivers using optoelectronic integrated circuits (OEICs), it seems that the more popular choices are the combination of a p-i-n photodiode and a high electron mobility transistor (HEMT) or a heterojunction bipolar transistor (HBT) [11].

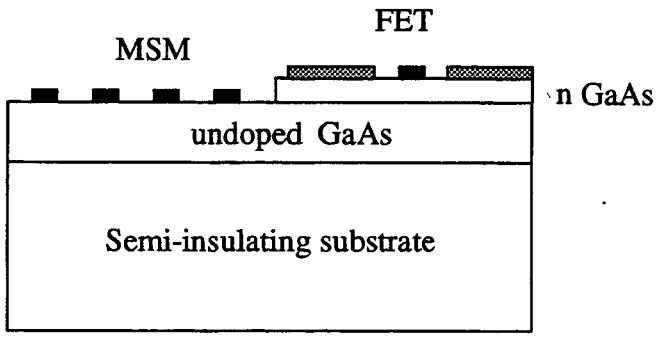

Figure 2.5 MSM photodetector integrated with MESFET.

2.3 Semiconductor photodetectors with internal gain

2.3.1 Photoconductive detector

A photoconductive detector is made of some absorptive semiconductor, such as InGaAs, with two electrical terminals. In the dark, the semiconductor behaves like a resistor with a finite dark current at a constant voltage bias. Electrical conductivity increases when it is illuminated because of photo-generated carriers and the current increases. The simplicity makes it attractive in OEICs.

The internal gain arises from the space charge neutrality requirement. The photo-generated electron-hole pairs move towards their respective collecting terminal with different velocities. The faster carriers are collected first, which results in excessive charge in the photoconductor. The excessive charge draws another faster carrier into the conducting layer until the slower one is recombined or collected. Therefore, the internal gain is equal to τ/t_r, where τ is the slower carrier lifetime (transit time), and t_r the fast carrier transit time. The bandwidth is inversely proportional to the relatively large τ; therefore, the bandwidth is normally limited to 100 MHz. Thus, an increase in gain can only be obtained at the expense of the speed of response. This is clearly another example of the trade-off between gain (or quantum efficiency) and bandwidth.

As for optical fibre communications, the relative large dark current (from lack of a p-n junction and required narrow bandgap energies) and its associated noise are the major problems. Quantum efficiency would be compromised significantly if the dark current is reduced to an acceptable level with current technology. Because of the limited bandwidth and large leakage current, photoconductors are rarely used in optical fibre communications.

2.3.2 Phototransistor

A phototransistor is similar to a bipolar transistor except normally there is no electrical contact to the base as shown in Figure 2.6. The base and the base-collector junction regions are used as the photosensitive region. The holes generated in these regions accumulate in the base. This excessive charge causes electrons to be injected from the emitter, and the current gain is achieved as in a normal bipolar transistor.

Phototransistors have yet to find use in major optical fibre communication systems although these devices have been investigated intensively in the late 1970s. The problems are quantum efficiency/gain and bandwidth, and maybe the more critical one is that a

steady-state illumination is required to bias the phototransistors to achieve linear amplification and fast response time.

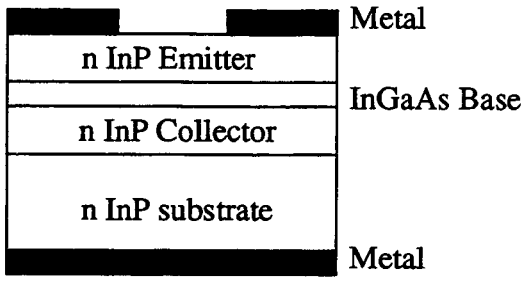

Figure 2.6 n-p-n InGaAs/InP phototransistor.

2.4 Fundamentals of APD

From the above discussions, it is clear that a p-i-n photodiode is by far the better choice among the photodetectors without internal gain. However, the photodetectors with internal gain are advantageous over the photodetectors without internal gain, especially when it comes to detecting weak signals. The counterpart of p-i-n photodiode, avalanche photodiode (APD), is a good choice, and is widely used.

The optical receivers with APDs are normally about 10 dB more sensitive than the optical receivers with p-i-n photodiodes, which may translate into an extra 40 km repeater spacing if 0.25 dB/km attenuation in optical fibres is assumed. The combination of p-i-n photodiode and EDFA is adequate in sensitivity. However, for sufficiently short distances or high launched powers, it may be advantageous to use a high-speed APD over an EDFA/ PIN configuration for significant cost reduction [10]. More importantly, no reliable optical amplifiers operating at 1.3 μm wavelength are available yet. For 1.3 μm optical fibre communication systems, APDs are far more sensitive than PINs without using optical amplifiers.

APDs suffer several drawbacks compared to PINs:

- more complex structure and complicated fabrication, therefore more expensive and less reliable;
- of inherently lower bandwidth at higher multiplication gains because the avalanche multiplication process takes extra time; and
- a higher bias voltage (30-70 V) is required, compared to 5 to 10 V required for PINs.

2.4.1 Avalanche multiplication

The APD's internal gain is realized by the avalanche multiplication process, which is achieved through impact ionization. The impact ionization phenomenon has been extensively investigated both theoretically and experimentally [55][56][57]. Electrons and holes are accelerated by a high electric field until they gain sufficient energy to excite an electron from the valence band into the conduction band, as shown in Figure 2.7. This process is a three-body collision process. The required minimum carrier energy for causing impact ionization is the ionization threshold energy E_i, which is obviously larger than the bandgap energy. Electrons and holes normally have different ionization energies.

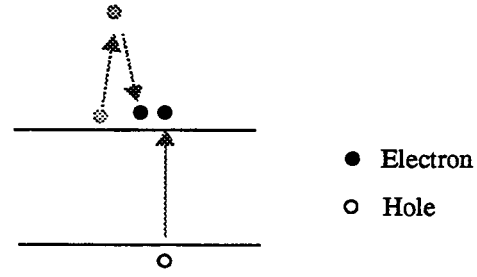

Figure 2.7 Impact ionization.

The impact ionization process is quantified by (impact) ionization rates α and β for electrons and holes, respectively. They are defined as the reciprocal of the average distance, measured along the direction of the electric field, traveled by an electron or a hole

to create an electron-hole pair. In the process of acceleration, the electrons and holes inevitably lose energy to non-ionization collision processes, such as phonon scattering.

One carrier undergoing the impact ionization creates a pair of free carriers. All three carriers get re-accelerated, and then continue to undergo impact ionization events and generate more free carriers. This process is only terminated if all the free carriers are swept out of the high electric field region. In the end, one initial electron (hole) generates M extra electron-hole pairs. M is therefore the APD multiplication gain (photogain).

2.4.2 Rate equations and photogain

The mathematical descriptions of avalanche multiplication are well documented [56][3]. Suppose that the avalanche multiplication occurs only within the multiplication region (the high electric field region) as shown in Figure 2.8(a) (x between 0 and w). The electron current, $J_n(x)$, increases and the hole current, $J_p(x)$, decreases along positive x direction. The rate equation for $J_n(x)$ can be written as

$$\frac{d}{dx}J_n(x) = \alpha(x)\cdot J_n(x) + \beta(x)\cdot J_p(x) + q\cdot G(x), \tag{2.3}$$

and for $J_p(x)$

$$-\frac{d}{dx}J_p(x) = \alpha(x)\cdot J_n(x) + \beta(x)\cdot J_p(x) + q\cdot G(x), \tag{2.4}$$

where G(x) is the space charge generation rate (optically or thermally). The total current $J = J_n(x) + J_p(x)$ is a constant throughout the structure (current continuity). Substituting this condition into each of the above expressions, and integrating both sides from 0 to w by using integrating factor $\exp\left(-\int_0^x (\alpha-\beta)\,dx'\right) \equiv \exp(-\varphi(x))$, the total current can be obtained in two equivalent forms

$$J = \frac{J_p(w) + J_n(0)\exp[\varphi(w)] + q\exp[\varphi(w)]\int_0^w G(x)\exp[-\varphi(x)]\,dx}{1-\int_0^w \beta\exp[\varphi(w)-\varphi(x)]\,dx}, \tag{2.5}$$

$$J = \frac{J_p(w)\exp[-\varphi(w)] + J_n(0) + q\int_0^w G(x)\exp[-\varphi(x)]\,dx}{1 - \int_0^w \alpha\exp[-\varphi(x)]\,dx}. \tag{2.6}$$

Pure electron and hole injection conditions are represented by $J_p(w) = 0$ and $J_n(0) = 0$, respectively. Therefore, the gains with pure electron injection, M_n, and with pure hole injection, M_p, can be respectively derived as

$$M_n = \frac{J}{J_n(0)} = \frac{\exp[\varphi(w)]}{1 - \int_0^w \beta\exp[\varphi(w) - \varphi(x)]\,dx} \equiv \frac{1}{1 - \int_0^w \alpha\exp[-\varphi(x)]\,dx}, \tag{2.7}$$

$$M_p = \frac{J}{J_p(w)} = \frac{1}{1 - \int_0^w \beta\exp[\varphi(w) - \varphi(x)]\,dx} \equiv \frac{\exp[-\varphi(w)]}{1 - \int_0^w \alpha\exp[-\varphi(x)]\,dx}. \tag{2.8}$$

The avalanche breakdown occurs when the multiplication gain is infinite, and it can be shown that for both pure electron and hole injections, the breakdown condition is the same, that is,

$$1 - \int_0^w \alpha\exp[-\varphi(x)]\,dx \equiv 1 - \int_0^w \beta\exp[\varphi(w) - \varphi(x)]\,dx = 0. \tag{2.9}$$

It can also be shown that if $\alpha > \beta$, then $M_n > M_p$, and vice versa. Thus a higher gain is obtained if the carriers with larger ionization rate are injected. It will be demonstrated later that this is also the condition for lower excess noise and higher bandwidth.

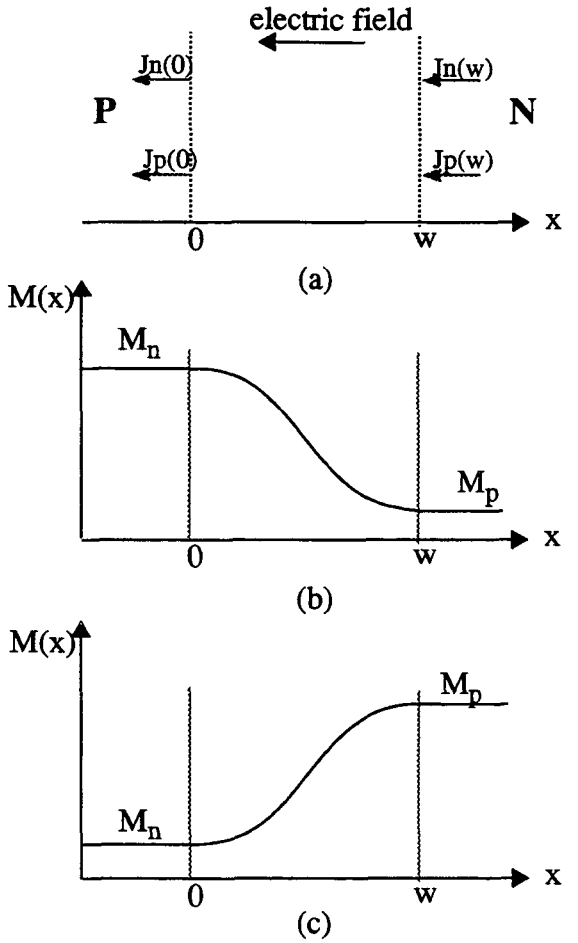

Figure 2.8 (a) Avalanche multiplication within a multiplication region, and gain along x direction for the case of (b) $\alpha > \beta$, or (c) $\alpha < \beta$.

In the case of no carrier injections, the carriers can still be photo-generated within the multiplication region. Suppose that the carriers are photo-generated at x_0 between 0 and W, and let $G(x) = G_o \delta(x - x_o)$, then the gain $M(x_0)$ is given by

$$M(x_o) = \frac{J}{qG_o} = \frac{\exp[\varphi(w) - \varphi(x_o)]}{1 - \int_0^w \beta \exp[\varphi(w) - \varphi(x)]\, dx} \equiv \frac{\exp[-\varphi(x_o)]}{1 - \int_0^w \alpha \exp[-\varphi(x)]\, dx}. \qquad \textbf{(2.10)}$$

It is obvious that $M_n = M(0)$ and $M_p = M(w)$. The variations of M(x) along x direction are displayed in Figure 2.8(b) and (c). The current can be written in a more physical expression

$$J = J_n(0)M_n + J_p(w)M_p + q\int_0^w G(x)M(x)\,dx. \tag{2.11}$$

2.4.3 Multiplication excess noise

The avalanche multiplication process is a random process, and the multiplication gain described in eqn. (2.10) represents only the average gain. The statistical variation of the multiplication gain is responsible for the multiplication excess noise, which is additional to the multiplication shot noise associated with the current. The total mean square noise spectral density [58][59] can be described by

$$\langle I_M \rangle^2 = 2q\left(2\left[I_n(0)M_n^2 + I_p(w)M_p^2 + \int_0^w G(x)M^2(x)\,dx\right] + I\left[2\int_0^w \alpha M^2(x)\,dx - M_p^2\right]\right), \tag{2.12}$$

where I is the total current. In the case of pure electron or hole injection,

$$\langle I_M \rangle^2 = 2qI_{po}M^2F, \tag{2.13}$$

where I_{po} is the primary photocurrent, M is either M_n or M_p, and F is the excess noise factor. F is always greater than or equal to 1, and $F = 1$ only if the multiplication process does not cause additional noise. It has been shown to a very good approximation [58][59] that

$$F = M\{1 - (1-k)\left(\frac{M-1}{M}\right)^2\}, \tag{2.14}$$

where k is either replaced by k_{eff} or k'_{eff} for the respective case of pure electron or hole injection, and

$$k_{eff} = \frac{k'_{eff}}{k_1^2}, \qquad k'_{eff} = \frac{k_2 - k_1^2}{1 - k_2}, \qquad k_1 = \frac{\int_0^w \beta M(x)\,dx}{\int_0^w \alpha M(x)\,dx}, \qquad k_2 = \frac{\int_0^w \beta M^2(x)\,dx}{\int_0^w \alpha M^2(x)\,dx}. \tag{2.15}$$

For the case of uniform electric field in the multiplication region, $k_{eff} = \beta/\alpha$ and $k'_{eff} = \alpha/\beta$. In Figure 2.9, F is plotted for different k_{eff} (or k'_{eff}) values. It can be seen that for lower excess noise, the carriers with higher ionization rate should be injected and the ionization rates for electrons and holes should be as much different as possible.

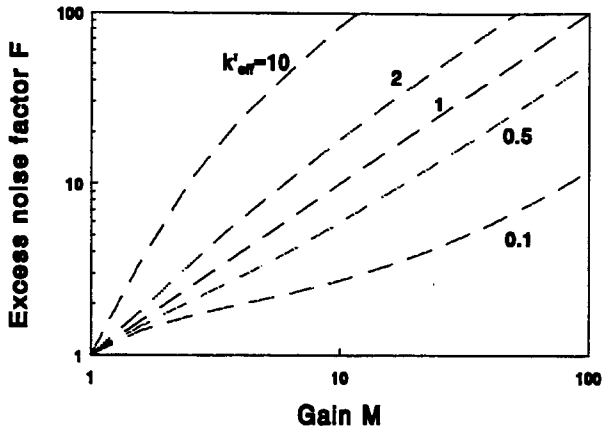

Figure 2.9 Excess noise factors for various values of k'_{eff} and M in the case of pure hole injection.

For the case of mixed carrier injections without charge space carrier generation [60], together with the average gain

$$\overline{M} = \frac{I}{I_n(0) + I_p(w)}, \tag{2.16}$$

the effective excess noise factor is given by

$$F_{eff} = \frac{fM_n^2 F_n + (1-f)M_p^2 F_p}{[fM_n + (1-f)M_p]^2}, \tag{2.17}$$

where f is the fraction of the total injection current due to electron injection ($= I_n(0)/(I_n(0) + I_p(w))$), and F_n and F_p are the corresponding excess noise factor for respective pure electron and hole injection. F_{eff} is always larger than F at the same average gain since in this case M_n or M_p is larger than $\overline{M}$.

2.4.4 Bandwidth

In addition to the limiting factors to the response speed in p-i-n photodiodes, such as the parasitic effect (RC) and the time required for the primary carriers to transit the depletion region, two additional limiting factors in the APDs are the avalanche buildup time and

the transit time of the secondary carriers. Practically, two more mechanisms are important: the hole trapping at the heterointerface and the diffusion tail [26][37][40][61]. In general, to analyze the time and frequency response of APDs, a pair of coupled time-dependent transport equations must be solved [62][63]. Those solutions are generally very complicated, and only recently have more rigorous analytical and numerical solutions been attempted [64][65][66].

Different limiting factors become dominant at different gains. At high enough gains, the bandwidth is inversely proportional to the avalanche buildup time. Since the gain is proportional to the buildup time, gain-bandwidth product GBW is independent of the gain. It can be proved that GBW (hole injection) is equal to $\frac{1}{2\pi N\tau\,(\alpha/\beta)}$ with N between 1/3 and 2, and τ is the transit time of the carriers in the multiplication region [62][63]. It is clear that GBW is higher if k'_{eff} is smaller.

In summary, to achieve lower excess noise and higher GBW product, the carriers with higher ionization rate should be injected and the difference between the ionization rates for electrons and holes should be as much different as possible.

2.4.5 Quantum efficiency

As shown in Figure 2.10, suppose that the width of absorption layer is x_{abs} with the absorption coefficient γ, and the reflection coefficient at the incident surface is R, then the optical power P(x) loss dP at x is given by

$$dP = -\Upsilon P dx, \tag{2.18}$$

with solution

$$P(x) = (1-R)P_i e^{-\Upsilon x}. \tag{2.19}$$

Therefore the quantum efficiency η without any carrier recombination is given by

$$\eta = \frac{\int_{x_{abs}}^{0} dP}{P_i} = (1-R)\,(1-e^{-\Upsilon x_{abs}}). \tag{2.20}$$

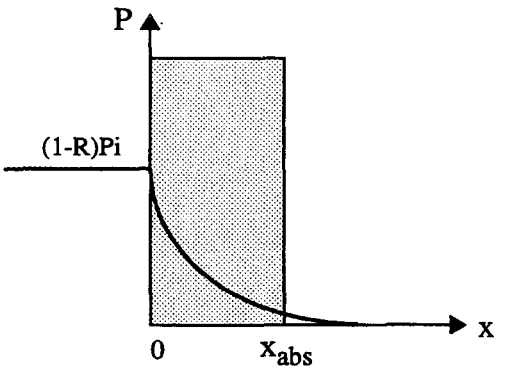

Figure 2.10 Optical power attenuation in an absorption layer.

2.4.6 Photocurrent

The photocurrent I_p is related to the photogain M by

$$I_p = I_{po}M, \tag{2.21}$$

where I_{po} is the primary photocurrent. Without any carrier recombinations,

$$I_{po} = \frac{q\eta P_i}{hc/\lambda} = \frac{q\lambda P_i}{hc}(1-R)\,(1-e^{-\Upsilon x_{abs}}). \tag{2.22}$$

Using eqn. (2.1), the responsivity is then given by

$$\Re = \frac{I_{po}}{P_i} = \frac{q\lambda}{hc}(1-R)\,(1-e^{-\Upsilon x_{abs}}). \tag{2.23}$$

2.4.7 Dark current and its noise

The dark current I_d of APDs consists of two components - multiplied and unmultiplied dark currents, that is,

$$I_d = I_{do}M + I_{du}, \tag{2.24}$$

where I_{do} is the primary dark current, and I_{du} is the unmultiplied leakage dark current via shunt paths. The important conduction mechanisms for the primary dark current are diffusion, generation-recombination (GR), and tunneling.

The diffusion current in p-n diodes at reverse bias voltages greater than a few kT/q is given by [67]

$$I_{diff} = qn_i^2\left(\sqrt{\frac{D_n}{\tau_n}}\frac{A_p}{N_A} + \sqrt{\frac{D_p}{\tau_p}}\frac{A_n}{N_D}\right), \tag{2.25}$$

where, $\tau_n(\tau_p)$, $D_n(D_p)$, $A_p(A_n)$, and $N_A(N_D)$ are the minority carrier diffusion lifetime, the minority carrier diffusion constant, the area of the depletion region boundary, and the doping concentration in the p (n) region, respectively. n_i is the intrinsic carrier concentration, and it is given by

$$n_i = 2(4\pi^2 m_e m_h k^2/h^4)^{3/4} T^{3/2} \exp(-E_g/2kT), \tag{2.26}$$

where $m_e(m_h)$ is the effective mass of electron (hole), h is Planck's constant, and T is the absolute temperature.

The GR current at reverse bias V is approximately given by

$$I_{gr} = \frac{qn_i AW}{\tau_{eff}}(e^{qV/2kT} - 1), \tag{2.27}$$

where A and W are the area and width of the depletion region, respectively, and τ_{eff} is the effective carrier lifetime [71]. GR is assumed to occur via traps near the middle of the bandgap [72]. Since $I_{diff} \propto n_i^2 \propto \exp(-E_g/kT)$ and $I_{gr} \propto n_i \propto \exp(-E_g/2kT)$, it is expected that the GR current would be dominant at lower temperatures, and the diffusion current dominant at higher temperatures.

For band-to-band tunneling in a direct bandgap semiconductor, the tunneling current is given by [67][72]

$$I_{tun} = \frac{(2m_e)^{1/2} q^3 F_m V A}{h^2 E_g^{1/2}} \exp\left(-\frac{2\pi\Theta m_e^{1/2} E_g^{3/2}}{qhF_m}\right), \quad (2.28)$$

where F_m is the maximum electric field, and the parameter Θ depends on the detailed shape of the tunneling barrier. Θ is 1.11 for a triangular barrier and 1.88 for a parabolic barrier. The only temperature dependence parameter is the bandgap energy E_g, and therefore, the tunneling current has a considerably weaker temperature dependence than either the diffusion or GR currents.

2.5 APD Evolution

2.5.1 Silicon APD

Because of the large ratio of electron to hole ionization rate and mature processing technology, silicon is the most suitable material for the 0.8 - 0.9 μm wavelength first generation optical fibre communication systems. The absorption coefficient dictates that absorption width is a few tens of μm. A simple Si p^+-n structure is not a satisfactory design for Si APDs, since it would require more than 500 V bias voltage to deplete such a long absorption layer. In addition, the high electric fields at operating bias voltages degrade the noise performance considerably.

The reach-through structure consisting of a p^+-π-p-n^+ structure is the standard design of Si APDs, and it is shown in Figure 2.11 [12]. Most of the photons are absorbed in the π region (~ 50 μm) since both p and n^+ regions are thin (a few μm). At operating bias voltages, the electric fields in the π region are low enough not to cause impact ionization, but high enough (20 V/μm) to ensure the generated carriers being swept at their scattering-limited velocity (10^2 μm/ns) to the p region, where the impact ionization occurs because of higher electric field. This type of Si APD can achieve breakdown voltage as low as 200

V, nearly 100% quantum efficiency, photogain as high as 10^4, excess noise with $k_{eff} \sim 0.04$ for photogains up to 500, and 500 MHz bandwidth for photogains up to 100.

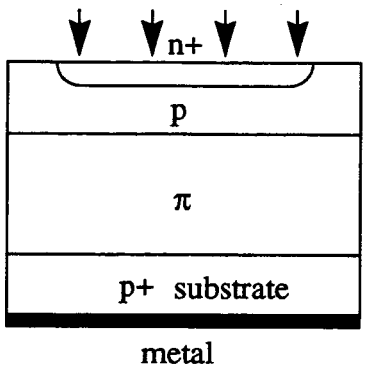

Figure 2.11 A silicon reach-through avalanche photodiode.

2.5.2 Germanium APD

Germanium is not the ideal material for APDs because it has almost equal electron and hole ionization rates. To achieve better noise performance, the n^+ - n - p structure shown in Figure 2.12 is the preferred one for the wavelength 1.3 μm [12]. Almost all incident light is absorbed in the thick n region (a few μm), and pure hole injection is achieved. It can achieve ~ 30 V breakdown voltage, ~ 200 nA leakage current, > 80% quantum efficiency, photogain 30 to 40, excess noise with k'_{eff} 0.6 - 0.7 for photogain up to 50, and larger than 1 GHz bandwidth. For 1.55 μm, the absorption in Ge is weak. A reach-through structure as in the case of Si APD is desired.

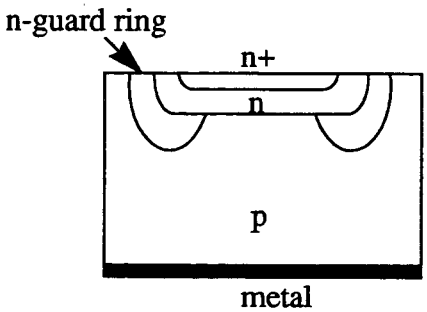

Figure 2.12 Germanium n^+ - n - p APD.

Therefore, germanium APDs may be used reasonably well used for the whole interested wavelength range 0.8 - 1.6 μm. However, ideally, the selected semiconductor should have only a marginally smaller bandgap energy than the energy of photons. This would ensure a compact structure with sufficient response, as well as a minimized tunnelling leakage currents. Large leakage current and its associated noise in germanium photodetectors are detrimental to their performance as sensitive photodetectors. In addition, germanium APDs suffer from some technical fabrication difficulties, and a large excess noise factor.

Direct bandgap III-V compound semiconductor alloys are superior to germanium because their bandgap energies can be tailored to suit a particular application by changing the relative concentrations of their constituents. In addition, a number of alloys with different bandgap energies can be utilized to fabricate a device because of their lattice match possibilities. This additional flexibility has been critical in designing photodetectors which must meet many conflicting design requirements. Therefore III-V compound APDs almost completely replace Ge APDs in optical fibre communications at 1.3 and 1.55 μm wavelengths.

Ternary alloys such as InGaAs and GaAlSb have been used to fabricate photodetectors for longer wavelengths. In particular, the alloy $In_{0.53}Ga_{0.47}As$ ($E_g = 0.75eV$), which is lattice matched to InP ($E_g = 1.35eV$), has been extensively employed to design and fabricate photodetectors for 1.3 and 1.55 μm wavelengths. InGaAs represents $In_{0.53}Ga_{0.47}As$ hereafter, unless stated.

2.5.3 SAM and SAGM InP/InGaAs APDs

There are some excellent reviews on evolution of InP/InGaAs heterojunction APDs up to late 1980s [13][14]. Because of the relatively narrow bandgap and light masses of

electrons and holes, carriers in InGaAs undergo band-to-band tunneling breakdown at an electric field of about 15-20 V/μm, which is below the threshold electric field for avalanche multiplication. Homojunction InGaAs APDs (with a structure like p-i-n) were reported with the problem of large leakage currents [15]. This problem was clearly understood at the beginning, and a separate absorption and multiplication (SAM) structure shown in Figure 2.13(a) was proposed [16] to circumvent this tunneling problem. The objectives are to make absorption occur in a narrower bandgap layer, such as InGaAs, while avalanche multiplication occurs in a wider bandgap layer, such as InP. For this structure to operate properly as an APD, the following conditions must be satisfied.

- The absorption layer width is ~ 2 μm. The goals are to obtain good quantum efficiency by ensuring adequate absorption, and to ensure adequate bandwidth by not unnecessarily increasing the carrier transit time.
- The electric field at the InGaAs/InP heterointerface is smaller than 15 V/μm at operating bias voltages to avoid significant tunneling currents there.
- The absorption layer is completely depleted with minimum electric field 10 V/μm to ensure the photogenerated carriers being swept with the saturated velocities to the InP multiplication layer at operating bias voltages.
- The conflicting requirements for the electric fields in the absorption layer implies that the background doping concentration in the InGaAs absorption layer must be smaller than 2×10^{15} cm^{-3} if it is uniformly doped.
- The maximum electric field in the InP multiplication layer is larger than 45 V/μm to achieve significant avalanche multiplication.
- The doping concentration in the InP multiplication layer is smaller than 2×10^{17} cm^{-3} to avoid the large tunneling current there [17].

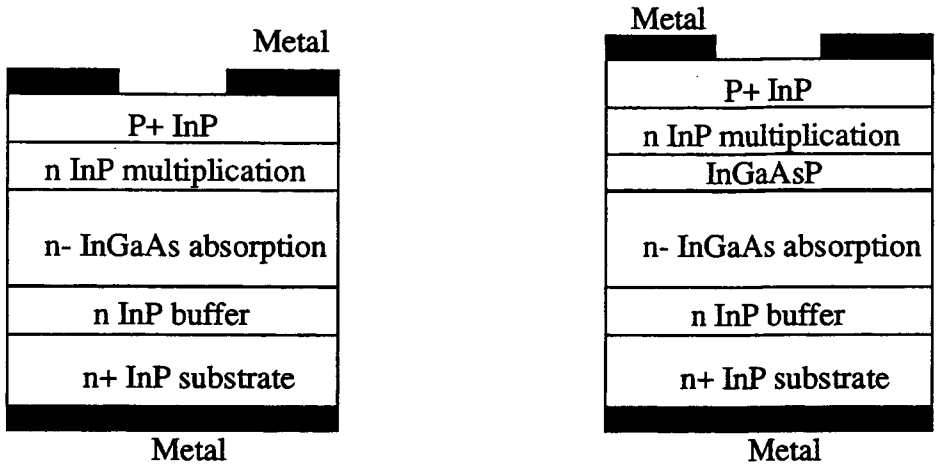

Figure 2.13 (a) SAM and (b) InGaAs/InP APDs.

SAM InP/InGaAs APDs were fabricated successfully [18][19][20] with useful gain ~ 10, leakage current ~ 25 nA before breakdown, and the primary multiplied dark current smaller than 1 nA. A severe limitation of SAM InP/InGaAs APDs is that the photo-generated holes are trapped at the InP/InGaAs heterointerface due to the valence band discontinuity (0.4 eV). The trapping results in a slow component of the photoresponse [21], which limits the bandwidth to a few hundred MHz [22].

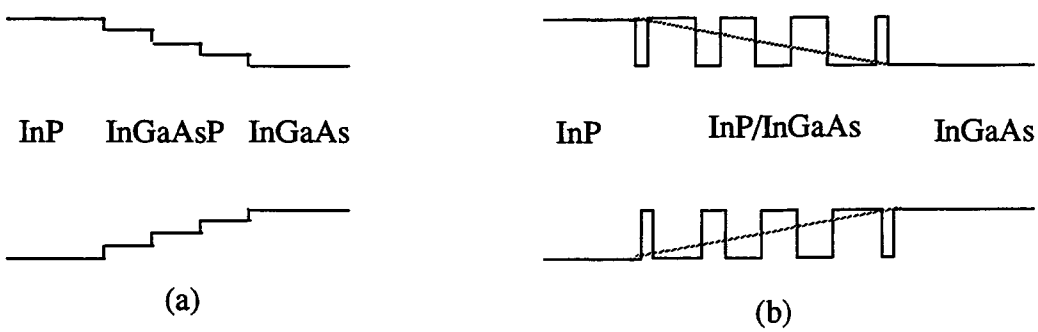

Figure 2.14 The band energy diagram of (a) compositional three-layer grading, and (b) variable-period superlattice.

As shown in Figure 2.13(b), this problem can be alleviated by incorporating a thin grading layer of InGaAsP between the InP multiplication and the InGaAs absorption layer [21][23][24][25][26]. The quaternary alloy InGaAsP can be tailored compositionally to have a bandgap energy anywhere between the bandgap energy of InGaAs (0.75 eV) and InP (1.35 eV), while simultaneously maintaining a fixed lattice parameter (5.869 Å). The gain-bandwidth products GBW for such devices are normally between 10 to 30 GHz [25][26]. An improved technique for increasing the bandwidth is to provide up to three InGaAsP transition layers as the grading layer, shown in Figure 2.14(a) [27][29]. Such devices have shown gain-bandwidth products up to 70 GHz, and are therefore adequate for 2.5 Gb/s optical fibre communications. This type of grading is the most common form in separate absorption, grading, and multiplication (SAGM) InP/InGaAs APDs. Alternatively, a sophisticated approach [28] is to grow a variable-period superlattice of InP and InGaAs, where the ratio of widths of thin layers of InP to InGaAs varies from very large at the InP side to very small at the InGaAs side, as demonstrated in Figure 2.14(b). In this way, a "pseudo-quaternary" compound is produced, and whose "effective bandgap" is determined by the local ratio and is shown as the dashed line in Figure 2.14(b).

2.5.4 SAGCM InP/InGaAs APD

The GBW of SAGM InP/InGaAs APDs can be increased by reducing the "effective multiplication" width [33][35]. The electric field profile in the multiplication layer is triangular, with the maximum electric field near the p^+-n junction. Most of the avalanche multiplication occurs around the location of maximum electric field. To reduce this width, the doping concentration in the InP multiplication layer should be increased. However, as discussed above, there is an upper limit of 2×10^{17} cm^{-3} to the doping concentration, which is almost impossible to fabricate. In addition, the theoretically possible achievement of GBW (about 90 GHz with a reasonable concentration of 5×10^{16} cm^{-3}) is at the price of

higher excess noise [32][35] because of the higher maximum electric field in the multiplication layer. This results in higher k_{eff} since it is well known that the ionization rates for electrons and holes in InP converge rapidly at electric fields higher than 60 V/μm [57]. In SAGM APDs, because of the strict requirements of electric field at the InP/InGaAs heterointerface and in the absorption InGaAs layer, it can be shown that the product of the doping concentration and the width of the InP multiplication layer (charge requirement) must be within a very small range. Thus, an increase in the doping concentration must be accompanied by a reduction in the multiplication width, and the accuracy of the multiplication layer width becomes critical to satisfy this charge requirement. Therefore, the increase in the doping concentration results in a narrow multiplication width with a small tolerance. For example [29], the control of a multiplication width of 0.5 μm must be within 0.02 μm for the doping concentration of 6×10^{16} cm^{-3}. The tolerance would be 0.01 μm if the doping concentration is 2×10^{17} cm^{-3}, an improbable task with today's fabrication technology for planar diffusion structure APDs.

To circumvent these problems, a high-low AlInGa/InGaAs was fabricated [30], and a δ-doped SAGM InGaAs/InP APD was proposed and analyzed [31][34][35] as shown in Figure 2.15. The primary advantages are that it decouples the doping concentration and width of the multiplication layer, and the flat electric field profile (because the multiplication layer is undoped) reduces the maximum electric field. It was predicted that GBW as high as 140 GHz could be achieved with a 0.2 μm thick multiplication layer, but with a concomitant increase in excess noise [35]. The high-low planar InP/InGaAs structure devices (which are named SAGCM) have been fabricated [36][37][38][39] with record-setting GBW of 122 GHz with a 0.1 μm wide multiplication layer [40], and without severe excess noise penalty [42]. The planar SAGCM InP/InGaAs APDs is discussed in detail in the next chapter.

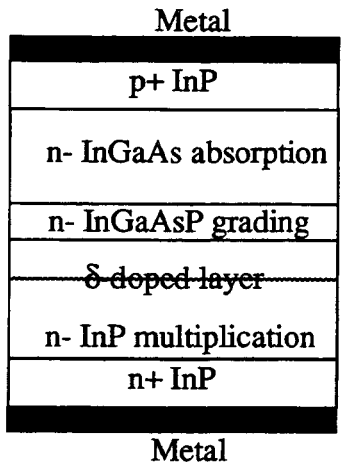

Figure 2.15 A δ-doped SAGM InGaAs/InP APD.

A properly designed SAG(C)M InGaAs/InP APD normally has bandwidth as a function of gain as shown in Figure 2.16 [40]. At low gains (2-4), the overall bandwidth is limited by hole trapping due to insufficient heterointerface electric field, and by the diffusion tail due to incomplete depletion of the absorption layer. At medium gains (5-20), the bandwidth is limited by the various transit times (particularly the transit of the secondary electrons) and the parasitic effects. At higher gains, the bandwidth is limited by the avalanche buildup time and GBW is a constant.

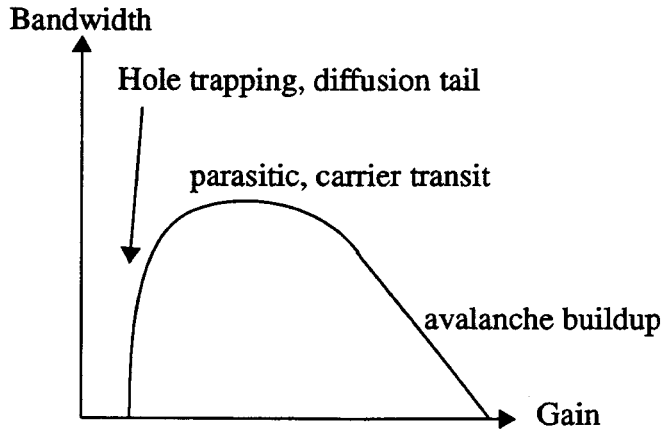

Figure 2.16 Various contributions to the overall bandwidth of SAGCM InP/InGaAs APDs. Both gain and bandwidth are in log scale.

2.5.5 Low noise and fast speed heterojunction APD

The excess noise and bandwidth of APDs depend strongly on the ratio of impact ionization rates for electrons and holes. Therefore, there is a great incentive to reduce this ratio since it can improve both noise and bandwidth performance characteristics simultaneously. The bulk III-V compounds are not very favorable in this regard. Popular schemes have been proposed in the early 1980s (i.e., multiquantum well (MQW) /superlattice (SL) [43], and staircase [44] APDs), and both of them use of a few tens of thin layers with the thickness of each layer a few hundred Å as the multiplication layer. The step-like MQW energy band diagram is shown in Figure 2.17(a). When an electron enters the well, it abruptly gains an energy equal to the conduction band discontinuity. This effectively reduces the electron ionization threshold energy, which greatly enhances the electron ionization rate. When the electron enters the next barrier, the opposite occurs. However, since the ionization rate in the well material is larger than the one in the barrier and the ionization rates depend on the threshold energy exponentially, the average ionization rate for electrons is largely enhanced. The holes undergo a similar process but with less enhancement due to the smaller valence band discontinuity. Such devices have been demonstrated successfully in the AlGaAs/GaAs material [45][46]. Unfortunately, the structure does not provide the same favorable enhancement when using InGaAs(P)/InP material systems [47], and any potential noise improvement is impaired by large tunneling leakage current in the InGaAs layers. For this reason, the more complex staircase scheme is devised as shown in Figure 2.17(b). The energy band structure is obtained by compositional grading. In this case, the impact ionization can occur at lower electric fields so that the tunneling current problem is eliminated. However, this structure presents substantial fabrication difficulty and has not been fabricated successfully.

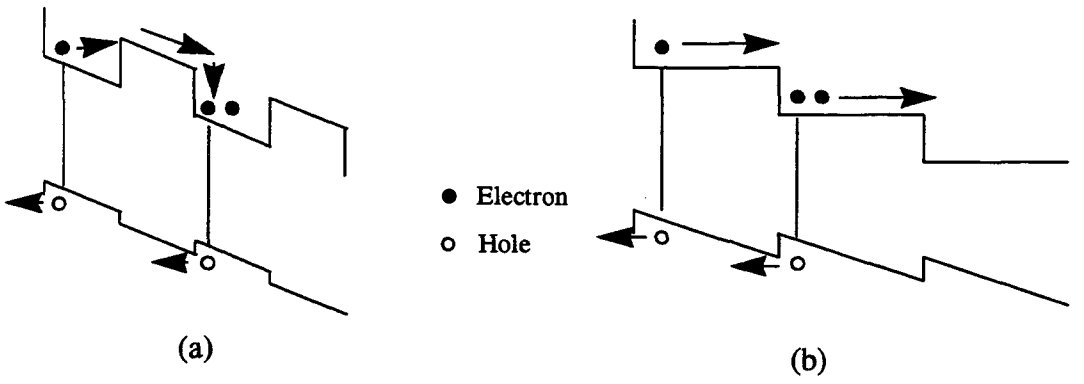

Figure 2.17 (a) MQW and (b) staircase APDs energy band diagrams under biasing.

The only commercially fabricated MQW/SL APDs for 1.3 and 1.55 μm wavelength optical fibre communications is the InGaAs(P)/InAlAs superlattice [48], in which the electron ionization rate is enhanced by a factor of 20 over the hole ionization rate [49]. Separate absorption, charge, and multiplication InGaAs/InAlAs superlattice multiplication APDs have been fabricated [50], and such devices have achieved gain-bandwidth product of 90 GHz and k_{eff} between 0.1 and 0.2 (about half of bulk InP) [51]. However, the improvement is impaired by large tunneling current in InGaAs. To eliminate this tunneling problem, a larger bandgap semiconductor is required. For example, InGaAsP/InAlAs superlattice APDs have been fabricated with GBW ~ 110 GHz and k_{eff} ~ 0.2. The superior advantage is best illustrated by a improved flip-chip structure with 17 GHz bandwidth [53], and by the successful 10 GB/s optical receiver with -27.4 dBm sensitivity (NRZ) [54], using this type of APDs.

Chapter 3 Planar SAGCM InP/InGaAs APD

In this chapter, the detailed structure, fabrication, and calibration of the planar SAGCM InP/InGaAs APDs are described.

3.1 Device structure

The APDs investigated in this research were designed to operate at 2.5 Gb/s, and possibly 10 Gb/s reliably with reasonable cost. As has been demonstrated in the last chapter, both the SAGM and SAGCM APDs can operate at data rates up to 10 Gb/s with a gain of 10. However, the yield of the SAGM APDs is low because of the tight tolerance in the thickness of the multiplication layer. Therefore, the SAGCM structure is selected.

Another consideration is that the devices should be mesa or planar. The mesa structure is simpler to design and fabricate, but its reliability is poor due to the requirement of passivation on crystal surfaces other than [100] surface. On the other hand, the planar structure is complicated to design and fabricate, but is of high reliability because the passivation is required on [100] surface only. Since reliability is crucial, planar structure is selected, similar to the structures of most commercial electronic devices.

One of the challenging problems in designing planar diodes is premature edge breakdown [71]. The electric field at the edge is always higher than the central region due to its small curvature. The standard solution is to use a guard ring shown in Figure 3.1 [25][29][73]. The guard ring modifies the doping profile at the edge region from abrupt into graded, which has a lower maximum electric field. An additional benefit is that the guard ring increases the curvature, which also results in a lower maximum electric field. However, the design and fabrication of a reliable (non-ion implanted) guard ring consti-

tutes a complex task. Because a technique for fabricating a linear graded impurity profile in n-type InP is not available yet, double guard rings must be used. Furthermore, the diffusion process used in fabricating the guard rings may limit the accurate control of the depth of the p^+ region.

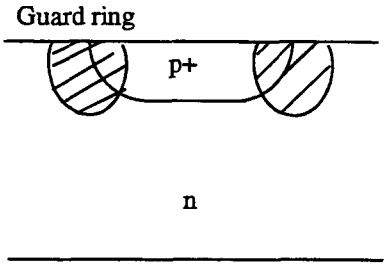

Figure 3.1 P^+-n diode with guard ring.

Another solution is to enhance the electric field in the central active region of the p-n junction by selectively increasing the charge density under that region [74]. This approach is extended further [36] as shown in Figure 3.2. Here, two lateral charge sheet, the full charge sheet σ_{active} in the central active region and the partial charge sheet $\sigma_{periphery}$ in the periphery region, are incorporated. This extra degree of freedom allows independent control of the electric fields in both the central active region and the periphery region. The full charge sheet σ_{active} is used to meet APD design requirements, and the partial charge sheet $\sigma_{periphery}$ is used to reach a balance between the electric field near the p^+ region edge and the electric field in the InGaAs absorption layer in the periphery region. Although the periphery charge sheet somewhat degrades the edge breakdown in the device, it is required to keep the electric field low in the InGaAs absorption layer, and hence to limit tunneling currents.

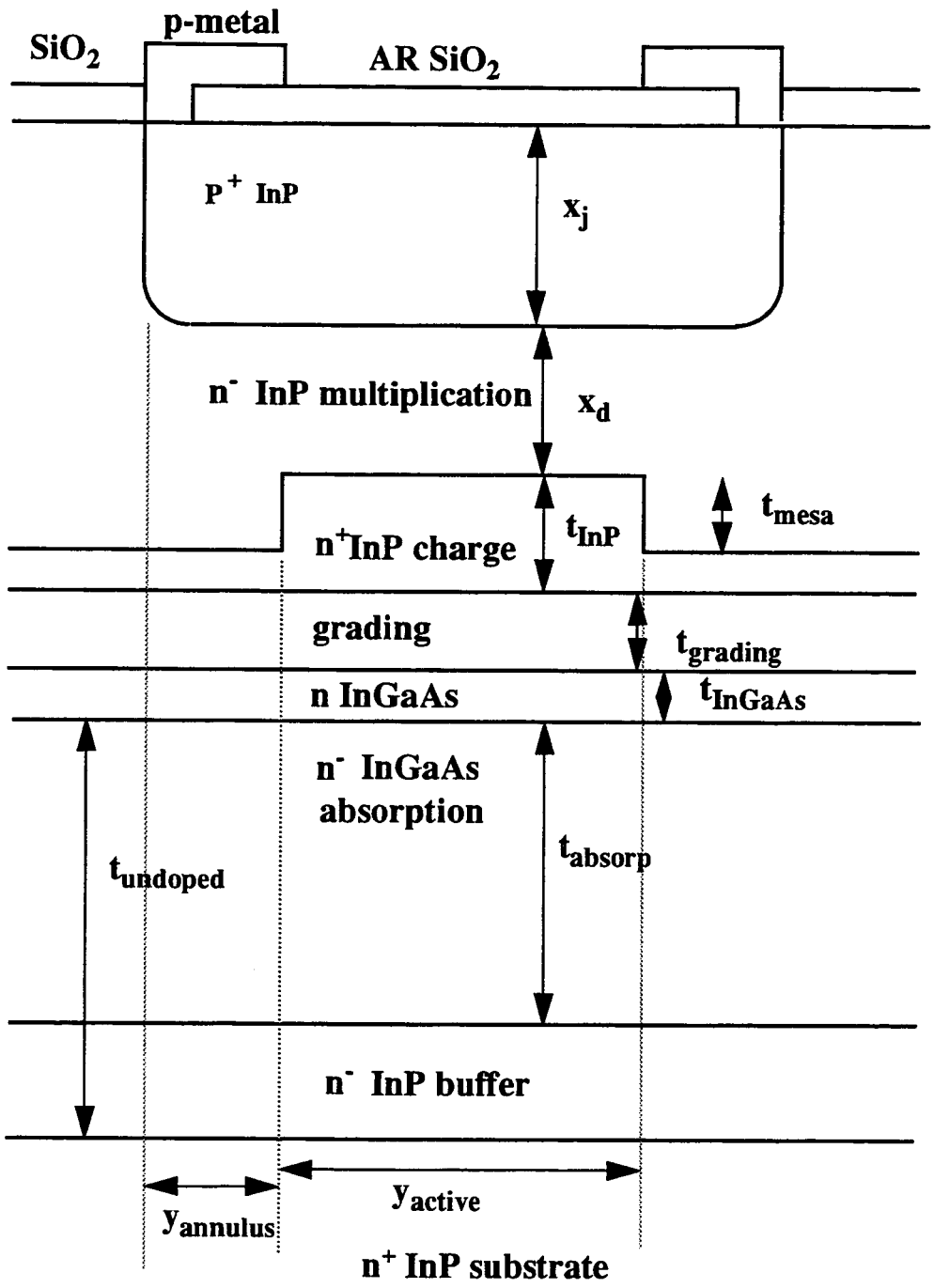

Figure 3.2 Planar SAGCM InP/InGaAs APD with a partial charge sheet in device periphery.

3.2 Fabrication

The fabrication and calibration of the planar SAGCM InP/InGaAs APDs with partial charge sheet in device periphery are described in detail in [75]. The metal-organic chemical vapor deposition (MOCVD) technique including an overgrowth is used to grow the wafers. The maximum lattice-mismatching among all the layers is about 0.07%. The upper limit of the unintentional background doping concentration is 1.0×10^{15} cm^{-3} in both InP and InGaAs.

An unintentionally doped InP buffer layer with a thickness of 0.5 ~ 1.0 μm is grown on a 2″ n^+-InP substrate. An unintentionally doped InGaAs absorption layer with thickness 2.5 ~ 3.3 μm follows. At the very end of it, a "boost" layer of thickness about 0.02 μm is formed by doping with Si (2.0×10^{17} cm^{-3}). The boost layer might increase the bandwidth since it helps to prevent hole trapping due to the higher heterointerface electric field. The grading layer consists of nine quaternary layers, compositionally graded from InGaAs to InP with the total thickness of ~ 0.09 μm. The dopant is Si and the doping concentration is ~ 1.0×10^{16} cm^{-3}. The InP charge layer is grown onto the wafer with thickness about 0.2 μm, and the integrated areal charge density σ_{active} (including the areal charge density in the boost and grading layers) is ~ 3.0×10^{12} cm^{-2} with Si as the dopant. The top 0.025 μm of the charge layer (sacrificial layer) as shown in Figure 3.3 is undoped, to avoid the following two problems. First, there is always a thin Si layer incorporated at the top of the charge layer before the overgrowth, and this causes substantial offset of the integrated areal charge density. Second, the cleaning procedure before the overgrowth removes a thin (less than 0.025 μm) uncontrollable thickness of the charge layer.

The mesas are patterned by standard photolithographic techniques with wavelengths of 4050 or 2900 Å and a dark field mask set (Z01). The etching is performed with either wet chemical etching (WCE) or reactive ion etching (RIE). To facilitate better control of

the etching, more complicated charge layer structures are fabricated in the first growth. For RIE, a low-high doping profile is adopted as shown in Figure 3.3(a). In this way, the uncertainty and non-uniformity of RIE have a minimum impact on σ_{active}. For WCE, an etch stop (InGaAs) within the charge layer is incorporated as shown in Figure 3.3(b). The thickness of the etch stop is chosen as 0.005 μm to balance the requirement of stopping etching and minimizing the tunneling current due to the narrower bandgap of the etch stop layer. Unless otherwise specified, WCE with an etch stop is selected.

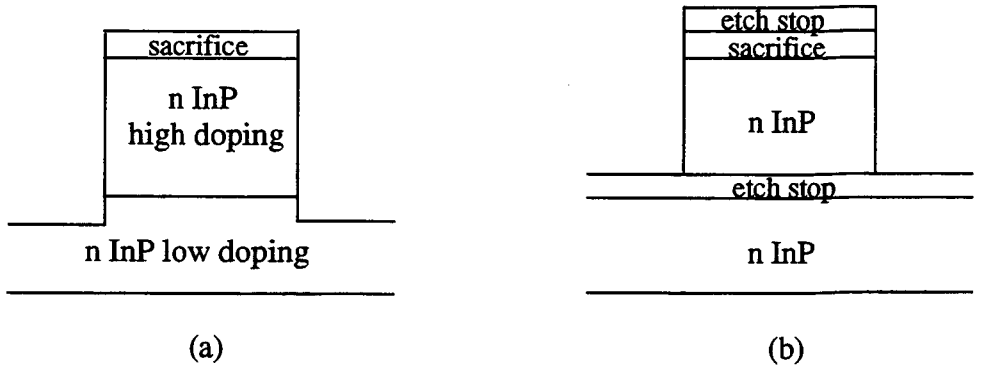

Figure 3.3 (a) Low-high doping mesa structure in RIE. (b) Mesa structure with etch stop in WCE.

The wafer is then put back into the MOCVD reactor and 2.5 μm of unintentionally doped InP cap layer is grown. A dielectric mask consisting of either of SiO_2 or SiN_x is then deposited. After the overgrowth, the mesa is still visible and the alignment for p^+ diffusion mask can be done without further complications. The Zn diffusion is monitored by a reference calibration sample and the depth x_j can be controlled within 0.1 μm. To precisely control the multiplication layer thickness x_d, the InP cap layer thickness is measured before the diffusion, and this is described in the next section. An anti-reflection (AR) coating of SiO_2 or SiN_x is applied to the wafer with a thickness about a quarter of the wavelength (~ quarter of 1.3 or 1.55 μm) in the material. The p-metal contact window is etched into the dielectric coating by RIE. The p-metal, which consists of 0.04 μm Cr

and 0.25 μm Au, is evaporated using an e-beam evaporator. A standard lift-off technique using a bilayer of polymethyl-methacrylate (PMMA) and photoresist is used to pattern the p-metal. The wafer is quartered and thinned down to a 150-200 μm thickness. Cr/Au n-metal is evaporated onto the polished substrate. The finished wafer is diced into 500×500 μm^2 dies and the dies are mounted onto 2×2×4 mm^3 ceramic carriers. The n-contact is formed by thermally compressing Au/Sn solder between the die and an Au pad on the ceramic carrier. p contact is formed with 1.0 or 1.4 mil diameter bonding wire of length ~ 2 mm.

3.3 Calibration

The Hall measurement technique is used to calibrate the doping concentrations. It uses a van der Pauw measurement sample, about 4×4 mm^2 in size that is cleaved from a calibration wafer. The Hall measurements determine that the upper limit of the unintentional background doping concentration is 1.0×10^{15} cm^{-3}. The intentional doping concentration is calibrated on the whole calibration wafers with layer thickness about 2 ~ 3 μm. It is found that the doping concentration is reduced by about 20% from the leading edge to the trailing edge (major flat) of the wafer, as shown in Figure 3.4. This is due to the gas flowing along that direction relative to the wafer in the MOCVD reactor. Along the direction perpendicular to the gas flow direction, the doping concentration variation is minimal.

Reflectance spectroscopy has been introduced for measuring the epitaxial layer thicknesses, such as the InP charge layer before the overgrowth and the InP cap layer after the overgrowth at both central and periphery regions. Reflectance is measured as a function of wavelength from 0.9 to 1.5 μm. Since in this spectral range, the InP layers are transparent while the InGaAs layers are opaque, then the measurement is similar to that of a single film thickness [76]. It is generally found that the variation of the InP cap layer thickness

after the overgrowth over a wafer is nearly radial, and it is thicker at the center and about 0.1 μm thinner at 8 mm from the edge along the direction of the gas flow. For measuring the InGaAs layer thicknesses, the technique of measuring the epitaxial layer thickness of A-B-A double heterostructure using reflectance spectroscopy is employed [77]. At present, the thickness measurement is only applied to wafers since the spot size of the spectrometer is 6 mm in diameter.

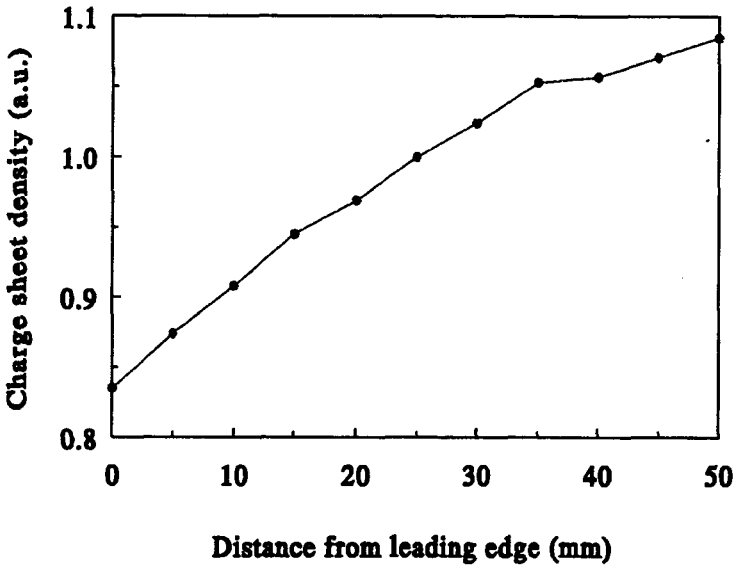

Figure 3.4 Measured (Hall measurement) doping profile for the charge sheet in the direction of MOCVD gas flow.

Secondary ion mass spectroscopy (SIMS) is used to determine the thickness of the multiplication layer and the doping profiles of the p^+, charge and grading layers, as shown in Figure 3.5. SIMS relies on removal of material from a solid by sputtering and on analysis of the sputtered ionized species. The depth axis of the SIMS profile is converted from the elapsed time by a subsequent stylus profilometry measurement. It is found that the doping profile of the p^+-n junction obeys a "modified erfc" function, which is quite close to an abrupt junction. The fall-off of the Zn concentration is a good indicator of the diffusion depth, which is found to be uniform across wafers within the SIMS uncertainty

(0.1μm). The abrupt increase of Si concentration provides an unambiguous location of the top of the charge layer. The separation between the Zn and Si profile edges is the thickness of the multiplication layer.

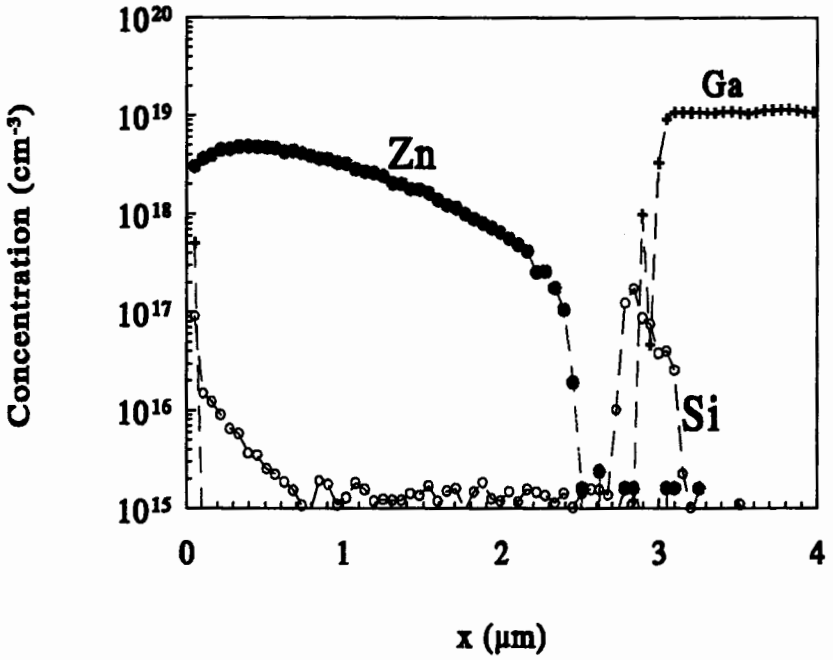

Figure 3.5 A typical SIMS profile.

3.4 Devices investigated

The planar SAGCM InP/InGaAs APDs with partial charge sheet in device periphery investigated in this thesis were designed and fabricated by Bell Northern Research, Ottawa, Canada. The devices investigated in the following chapters are from two wafers - P555 and P623. The nominal fabrication parameters are listed in the Table 3.1. The various thicknesses are already defined in Figure 3.2. σ_{charge}, $\sigma_{grading}$ and $\sigma_{periphery}$ are the integrated areal charge density in the charge, the grading, and the boost layers, respectively, and $\sigma_{active} = \sigma_{charge} + \sigma_{grading} + \sigma_{InGaAs}$ in the active central region. $\sigma_{periphery}$ is the corresponding value in the periphery region. Unless otherwise specified, all the devices

investigated here have GBW product in 50~100 GHz range. The highest is 122 GHz, a record-setting value [40].

Table 3.1 The nominal device fabrication parameters for wafer P555 and P623. The thickness is in μm and the integrated areal charge density is in 10^{12} cm^{-2}.

	y_{active}	$y_{annulus}$	x_j	x_d	t_{InP}	t_{mesa}	$t_{grading}$	t_{InGaAs}
P555	30	5	2.2	0.3-0.4	0.17	0.11	0.09	0.02
P623								
	t_{absorp}	$t_{undoped}$	σ_{charge}	$\sigma_{grading}$	σ_{InGaAs}	σ_{active}	$\sigma_{periphery}$	
P555	2.5-2.8	3.5-3.8	1.9-2.6	0.09	0.4	2.4-3.1	1.2-1.4	
P623	3.0-3.3		2.2-2.9			2.7-3.4	1.3-1.5	

Chapter 4 Critical device parameters extraction

The multiplication layer thickness x_d and the integrated areal charge density σ_{active} are crucial parameters for SAGCM APDs to meet design requirements. For our APDs, both device parameters vary significantly over a wafer when the devices are fabricated with current MOCVD technology. Even with the inherent advantages of SAGCM InP/ InGaAs APDs, it is still very important to control the variation of x_d when it is less than 0.5 μm (note that this is crucial for SAGM APDs). In our APDs, x_d is determined by two processes: growth of the epitaxial InP layer of thickness x_j+x_d, and subsequent p^+ diffusion of depth x_j. Because of the non-uniformity of the InP cap layer thickness and the uncertainty of the diffusion depth, it is difficult to control x_d to better than 0.1 μm across a wafer for devices intended for bandwidths greater than 5 GHz. Due to the gas flow direction in the MOCVD reactor and the uncertainty in mesa etching, σ_{active} can vary more than 20% across a wafer.

Typical direct measurements of x_d and σ_{active}, such as with secondary ion mass spectroscopy (SIMS) and Hall analysis, have limitations in that they are destructive and/or they must be performed on separate calibration wafers. Another common technique, capacitance-voltage (C-V) measurement, is not suitable for these devices because the capacitances are too small due to the small device size, resulting in a very noisy signal. In addition, the mesa structure makes the extraction of x_d and σ_{active} from C-V measurements a fairly complicated process, if not entirely impossible. Larger area devices were not readily available during the period of this investigation. Therefore, a new non-destructive technique to determine device parameters at device level is critical for on-going and further characterizing and modelling of our SAGCM InP/InGaAs APDs. In addition, determination of device parameters at the wafer level is very helpful to monitor wafer fab-

rication, and to reduce unnecessary fabrication and processing steps to reduce device cost.

In this chapter, a simple, innovative, and non-destructive method for determining both x_d and σ_{active} on a wafer and on individual APD is presented [78][81]. The method relies on punchthrough voltage V_{mesa} and breakdown voltage V_{br} easily obtained from photocurrent-voltage measurements. First, the experimental setup is briefly described, and then the detailed device parameters extraction technique is presented. Finally, this technique is applied to two wafers, and all possible errors, including both systematic and random ones, are discussed.

4.1 Experimental setup

The light is generated with a pigtail 1.3 μm LED, and is transmitted over a monomode optical fibre to the APD. The incident optical power is controlled by a HP optical attenuator. The end of the optical fibre is cleaved with core diameter about 10 μm, and it is pointed to the APD from a distance less than 50 μm away the surface. The incident light is directed at the central active region of the APD by maximizing the photocurrent at a bias voltage $0.9 \cdot V_{br}$ while moving the end of the optical fibre along the APD surface. The DC photocurrent is measured with a Keithley 617 Electrometer with the APD reverse-biased. The sensitivity is about 100 nA due to environmental noise. The normally employed phase-sensitive measurement of photocurrent is not necessary since both dark current and its associated noise are much smaller than the photocurrent. All instruments are controlled with a personal computer through an IEEE 488 bus.

4.2 Extraction technique

All properly designed APDs including SAGCM InP/InGaAs APDs show impact ionization breakdown at some reverse bias voltage V_{br}. However, as shown in Figure 4.2, an

additional characteristic voltage in our planar SAGCM InP/InGaAs APDs, which can be unambiguously determined from photocurrent-voltage characteristics, is the punchthrough voltage V_{mesa}. The punchthrough voltage is that at which the electric field starts to penetrate the InGaAs layers in the central active region [36]. The corresponding punchthrough voltage in the periphery region is V_{ann}. The detailed photo I-V characteristic in Figure 4.2 is now explained.

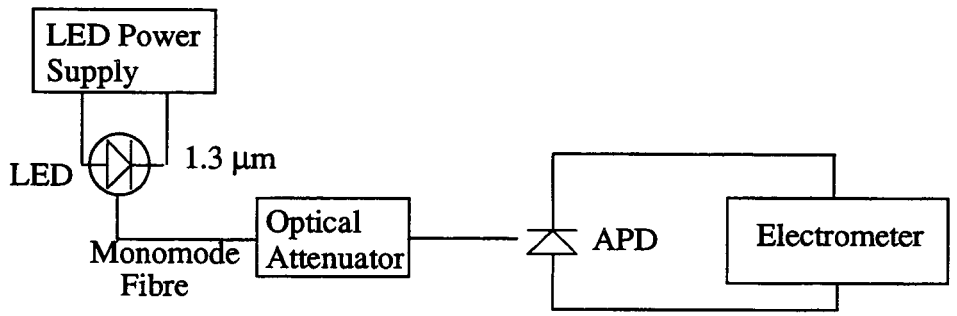

Figure 4.1 Photocurrent measurement setup.

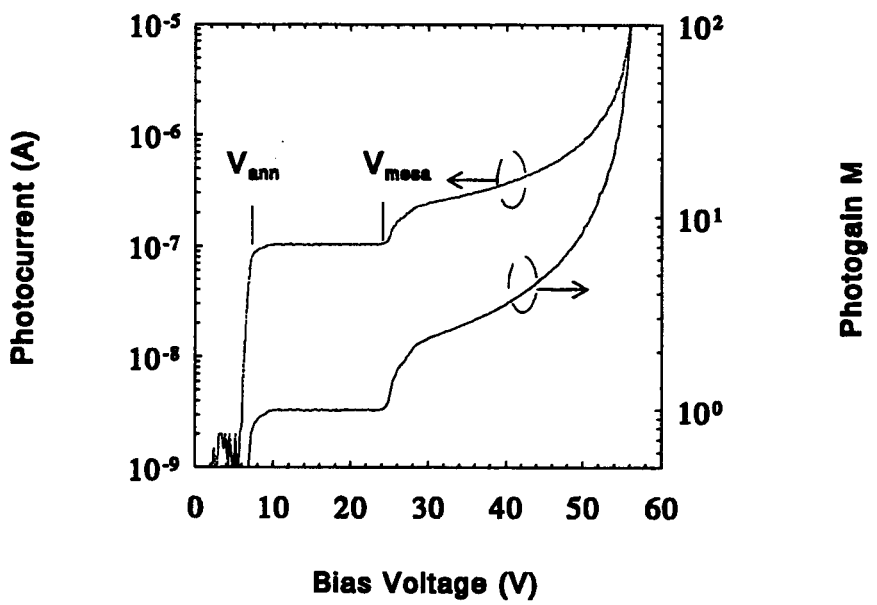

Figure 4.2 A typical (APD32, wafer P623) photocurrent versus bias voltage and its derived photogain.

When $V<V_{ann}$, the InGaAs absorption layer in both the active and the periphery regions are not depleted. The photocurrent is very small since the photogenerated holes in the absorption region are blocked by the energy barrier at the InP/InGaAs heterointerface, and eventually, the photogenerated electrons and holes recombine. When $V_{ann}<V<V_{mesa}$, the periphery region of the InGaAs absorption layer is depleted whereas the central active region is not. The energy barrier at the InP/InGaAs heterointerface in the central active region still blocks the photogenerated holes. However, the energy barrier in the periphery region is diminished. Because of the very high quality of the InGaAs semiconductor, the hole lifetime is about 18.5 μs and the diffusion length is about 140 μm [79]. Therefore, the long-lived photogenerated electron-hole pairs in the central active region can diffuse to the depleted periphery region, and are collected by the terminals. The photocurrent is constant over this range of voltage, and the gain is unity since the gain is due to impact ionization in the periphery region which is approximately unity at this range of low bias voltages. This is one of the unique features of planar SAGCM APDs with partial charge sheet in device periphery as the gain is calibrated automatically in this bias range. When $V>V_{mesa}$, the energy barrier in the active region is diminished, and the photogenerated holes are passing through the central active multiplication region. Therefore, the photocurrent and its derivative with respect to V starts to increase monotonically due to the increased impact ionization multiplication until the bias voltage reaches the avalanche breakdown voltage V_{br}. The existence of V_{mesa} is common in both planar and mesa SA(G)M InP/InGaAs APDs [18][24][25], but the existence of the unity gain bias voltage region is only observed in our high-quality planar SAGCM APDs with partial charge sheet in device periphery or in high-quality planar SAGM InP/InGaAs APDs with preferential lateral extended guard (PLEG) ring [25]. Also, the existence of the unity gain in our devices make it possible to derive directly the photogain, as shown in Figure 4.2.

With these two experimental characteristic voltages V_{mesa} and V_{br}, two device

parameters may be extracted if all other device parameters and the ionization rates are known. It is clear from the above discussions that it is most beneficial to extract x_d and σ_{active} – the two most critical and uncertain device parameters.

To relate the breakdown voltage V_{br}, the punchthrough voltage V_{mesa}, and the breakdown electric field F_{br} in the multiplication layer to the device parameters, the following assumptions and simplifications are made.

1. The p^+-n InP junction is abrupt.
2. The voltage drop at the InP/InGaAs heterointerface (0.1-0.4 V) is ignored.
3. The doping concentrations in the multiplication, charge and grading layers are uniform.
4. The thickness of the thin highly doped InGaAs layer is ignored,
5. The relative dielectric constant of the InGaAsP of the grading layer is assumed to be equal to the relative dielectric constant of InP.
6. The InP buffer layer is treated as part of the absorption layer.
7. The multiplication layer background doping concentration is assumed to be zero.
8. The doping concentration in the absorption layer is uniform,
9. The absorption layer is completely depleted at breakdown.

From Poisson's equation and appropriate boundary conditions as shown in Figure 4.3, from eqn. (A.11) and eqn. (A.3) it can be shown that

$$V_{mesa}+V_{bi} = \frac{q\sigma_{charge}}{\varepsilon_0\varepsilon_1}(x_d+t_{InP}/2) + \frac{qN_G t_{grading}}{\varepsilon_2\varepsilon_0}(x_d+t_{InP}+t_{grading}/2), \tag{4.1}$$

$$\begin{aligned} V_{br}+V_{bi} = {} & F_{br}(x_d+t_{InP}+t_{grading}+t_{undoped}) - \frac{q\sigma_{charge}}{\varepsilon_1\varepsilon_0}(t_{InP}/2+t_{grading}+t_{undoped}) \\ & - \frac{qN_G t_{grading}}{\varepsilon_2\varepsilon_0}(t_{grading}/2+t_{undoped}) - \frac{q\sigma_{InGaAs}}{\varepsilon_2\varepsilon_0}t_{undoped} - \frac{qN_D t_{undoped}^2/2}{\varepsilon_2\varepsilon_0}. \end{aligned} \tag{4.2}$$

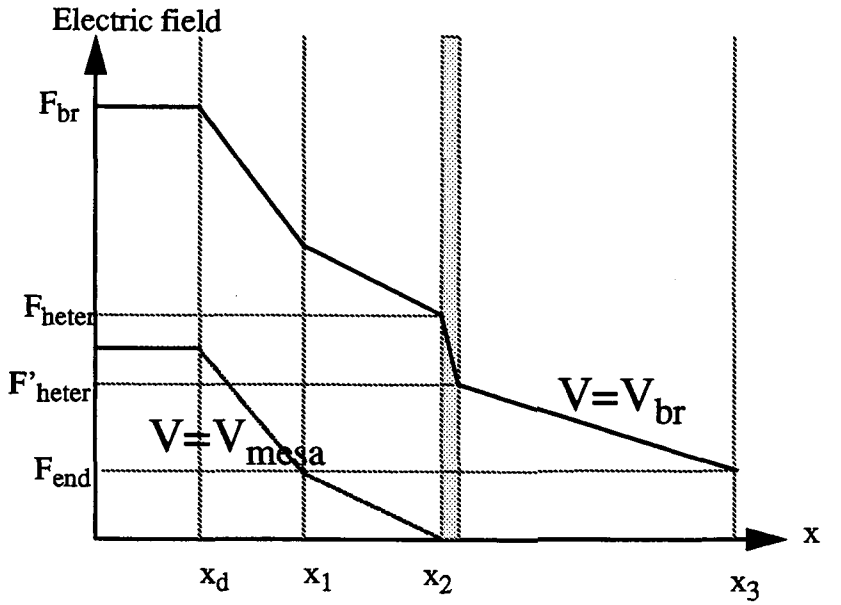

$$x_1 - x_d = t_{InP} \qquad x_2 - x_1 = t_{grading} \qquad x_3 - x_2 = t_{undoped}$$

Figure 4.3 The electric fields in SAGCM InP/InGaAs APD.

In the above equations, ε_1 and ε_2 are the relative dielectric constants for InP and InGaAs, and are 12.3 and 12.9, respectively. ε_0 is the dielectric constant of vacuum and q is the electron charge. N_G and N_{InGaAs} are the respective doping concentrations in the grading and highly doped thin InGaAs layers. N_D is the unintentional background doping concentration in the multiplication and absorption layers. σ_{InGaAs} ($= t_{InGaAs} N_{InGaAs} = 0.4\times10^{12} cm^{-2}$) is the integrated areal charge density of the thin highly doped InGaAs layer. σ_{charge} is the integrated areal charge density of the charge layer, and $\sigma_{active} = \sigma_{charge} + N_G t_{grading} + \sigma_{InGaAs}$. V_{bi} is the zero bias built-in voltage across the APD structure and it is approximately 1 V.

Two more simplifications are assumed for breakdown condition.

10. Impact ionization in the InGaAs absorption layer is ignored.
11. Impact ionizations in the charge and the grading layers are ignored.

The breakdown condition can be found from

$$\frac{\alpha_1(F_{br})}{\alpha_1(F_{br})-\beta_1(F_{br})}\exp\left[x_d\cdot\left(\beta_1(F_{br})-\alpha_1(F_{br})\right)\right]-\frac{\beta_1(F_{br})}{\alpha_1(F_{br})-\beta_1(F_{br})}=0, \tag{4.3}$$

which can be obtained from the more general breakdown condition in eqn. (2.9) when the electric field in the multiplication layer is constant. α_1 and β_1 are impact ionization rates for electrons and holes in InP, respectively. There are a few reported experimental values of α_1 and β_1 in the literature, and the particular set of values used results in differences in the extracted x_d and σ_{active}. This point is discussed in detail later. For now, the most commonly cited values [32] for α_1 and β_1 are used, which are

$$\alpha_1(F)=555\cdot\exp(-310/F),\ \beta_1(F)=198\cdot\exp(-229/F), \tag{4.4}$$

with the electric field F in V/μm, and the ionization rates in μm^{-1}. The three unknown variables F_{br}, σ_{charge} and x_d can be found by iteratively solving eqn. (4.1), eqn. (4.2), and eqn. (4.3), using values of α_1 and β_1 from eqn. (4.4), and with experimental V_{mesa} and V_{br} as sole input parameters.

Two more characteristic voltages are useful to calculate: the voltages V'_{mesa} and $V_{depleted}$ at which the electric field starts and finishes depleting the absorption layer (not including the thin highly doped InGaAs layer), respectively. From eqn. (A.12) and eqn. (A.7), it can be shown that

$$V'_{mesa}=V_{mesa}+\frac{q\sigma_{InGaAs}}{\varepsilon_2\varepsilon_0}\left(x_d+t_{InP}+t_{grading}\right), \tag{4.5}$$

$$V_{depleted}=V'_{mesa}+\frac{qN_Dt_{undoped}}{\varepsilon_2\varepsilon_0}\left(x_d+t_{InP}+t_{grading}+t_{undoped}/2\right). \tag{4.6}$$

Another two interesting values are the heterointerface electric field F_{heter} and F'_{heter} (Figure 4.3), the respective electric fields at the boundary of the thin highly doped InGaAs layer and the absorption layer, which are given by (eqn. (A.2))

$$F_{heter} = F_{br} - \frac{q\sigma_{charge}}{\varepsilon_0\varepsilon_1} - \frac{qN_G}{\varepsilon_0\varepsilon_1} t_{grading}, \tag{4.7}$$

$$F'_{heter} = F_{br} - \frac{q\sigma_{charge}}{\varepsilon_0\varepsilon_1} - \frac{qN_G t_{grading}}{\varepsilon_0\varepsilon_1} - \frac{q\sigma_{InGaAs}}{\varepsilon_0\varepsilon_2} \equiv F_{heter} - \frac{q\sigma_{InGaAs}}{\varepsilon_0\varepsilon_2}. \tag{4.8}$$

4.3 Results and Discussions

The device parameter extraction technique is tested on P555 and P623 wafers. The experimental values of V_{mesa} and V_{br} from the leading edge to the trailing edge of the wafers are displayed in Figure 4.4. The values of the device parameters used for modelling are listed in Table 4.1. The extracted values of x_d and σ_{active} are shown in Figure 4.5 (a) for wafer P555 and (b) for P623.

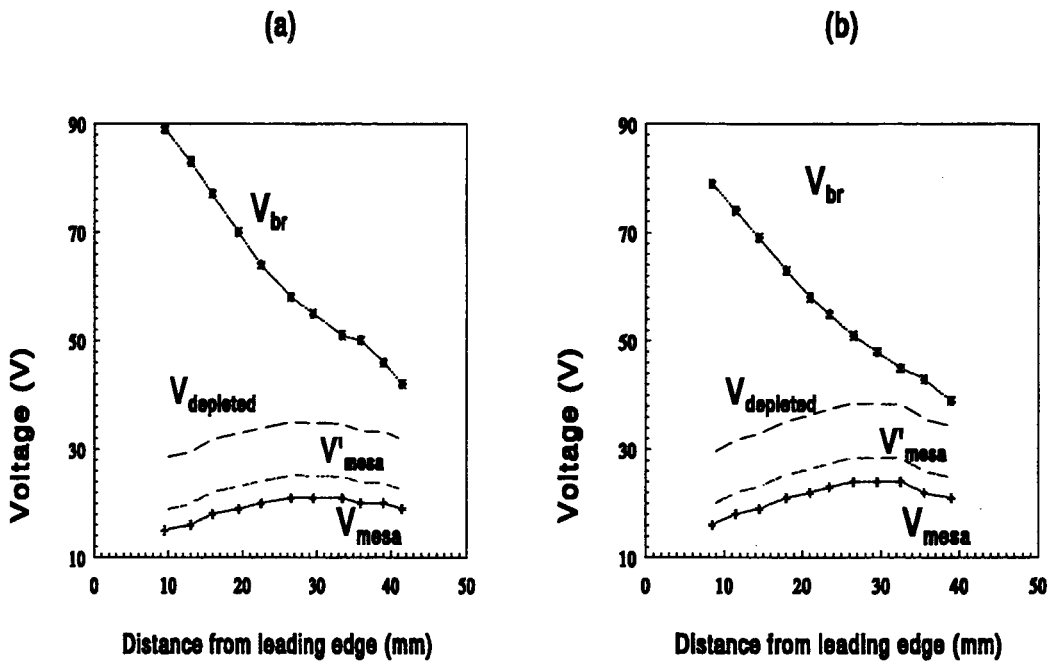

Figure 4.4 The experimental values of V_{mesa} and V_{br}, and the calculated V'_{mesa} and $V_{depleted}$ across (a) P555 and (b) P623 wafers.

Table 4.1 The values of the device parameters used for modelling. The thickness is in μm, the doping concentration is in 10^{15} cm^{-3}, and the integrated areal charge density is in 10^{12} cm^{-2}.

	t_{InP}	$t_{grading}$	N_G	σ_{InGaAs}	$t_{undoped}$	N_D
P555	0.17	0.09	10	0.4	3.8	0.7
P623						

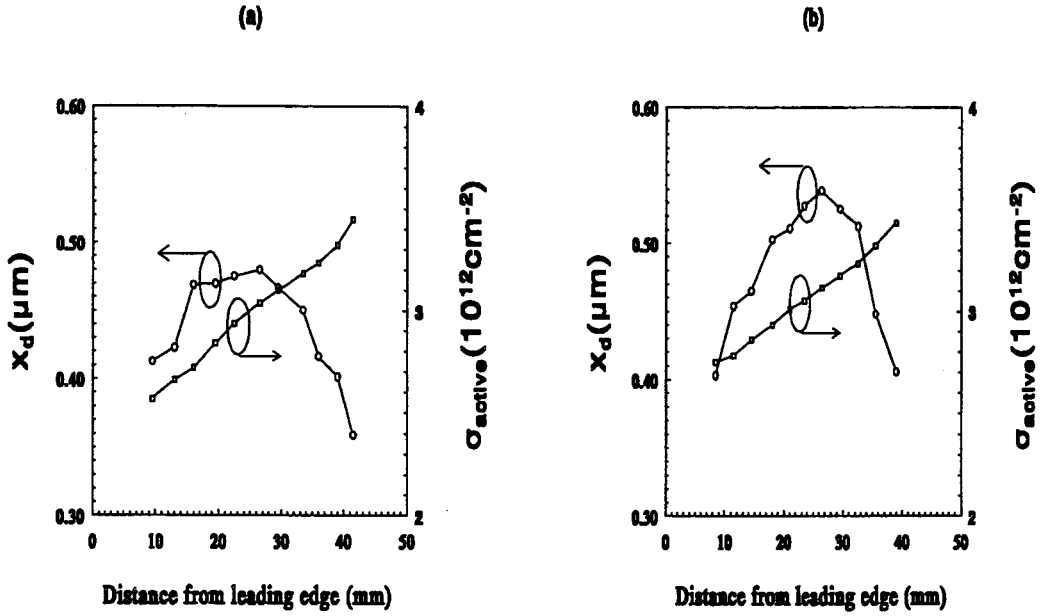

Figure 4.5 The extracted values of x_d and σ_{active} for wafer (a) P555 and (b) P623.

The extracted results agree quite well with the independent measurements (SIMS, reflectance spectroscopy, and Hall analysis), for which the results have been presented in [75][80] and in chapter 3. These independent measurements establish that for both wafers, x_d is greatest in the center of the wafer with a value about 0.4 μm, and falls off toward the edges to a value of ~ 0.3 μm. The trend is consistent with what has been calculated, but the calculated values are systematically 0.1-0.15 μm larger than the independently measured x_d values. However, the error of these independent measurements is about 0.1 μm and the error of this extraction technique is about 0.05 μm (shown later). Therefore, it can be concluded that the extracted and experimentally measured x_d values agree within the errors.

The small differences in x_d between wafer P555 and P623 reflects the fabrication uncertainty of ~ 0.1 μm. The small differences between wafer P555 and P623 reflect the fabrication uncertainty (0.1 μm) stemming from p^+ diffusion and the InP cap layer MOCVD growth.

σ_{active} for wafer P623 is designed to be (2.7-3.4)$\times 10^{12}$ cm^{-2} (Table 3.1), which is in good agreement with the extracted values. Wafer P555 is designed to have σ_{active} (0.2-0.3)$\times 10^{12}$ cm^{-2} smaller than the wafer P623, which agrees with the extracted values for the APDs near the leading edge. The variation of the extracted σ_{active} over wafer in Figure 4.5 is ~ 29% for wafer P555 and ~ 22% for wafer P623. The Hall measurements for calibrating this particular MOCVD reactor, which was used to grow the two wafers, established that σ_{active} increases by 15% to 20% from the location 8 mm from the leading edge to the location 8 mm from the trailing edge (Figure 3.4). This confirms that this extraction technique is successful in determining both absolute value of σ_{active} and its variation over wafer for wafer P623. However, the extracted variation of a 29% for wafer P555 is larger than the expected 20% variation. One possible reason for this discrepancy is that this fabricated wafer is slightly different from its design due to the very delicate fabrication processes.

The calculated V'_{mesa} and $V_{depleted}$ are shown in Figure 4.4, and the calculated F_{br}, F'_{heter}, and F_{heter} in Figure 4.6. The calculated $V_{depleted}$ is always lower than V_{br}, therefore the assumption that the absorption layer at breakdown is completely depleted is satisfied. The calculated V'_{mesa} is about 4 V systematically higher than V_{mesa}, which is not surprising since σ_{InGaAs} is assumed unchanged, and x_d changes very little. The calculated F_{br} is between 52 to 57 V/μm. This small variation of F_{br} is consistent with the small variation of the extracted x_d, since F_{br} depends only on x_d. Also F'_{heter} is about 5.6 V/μm lower than F_{heter}.

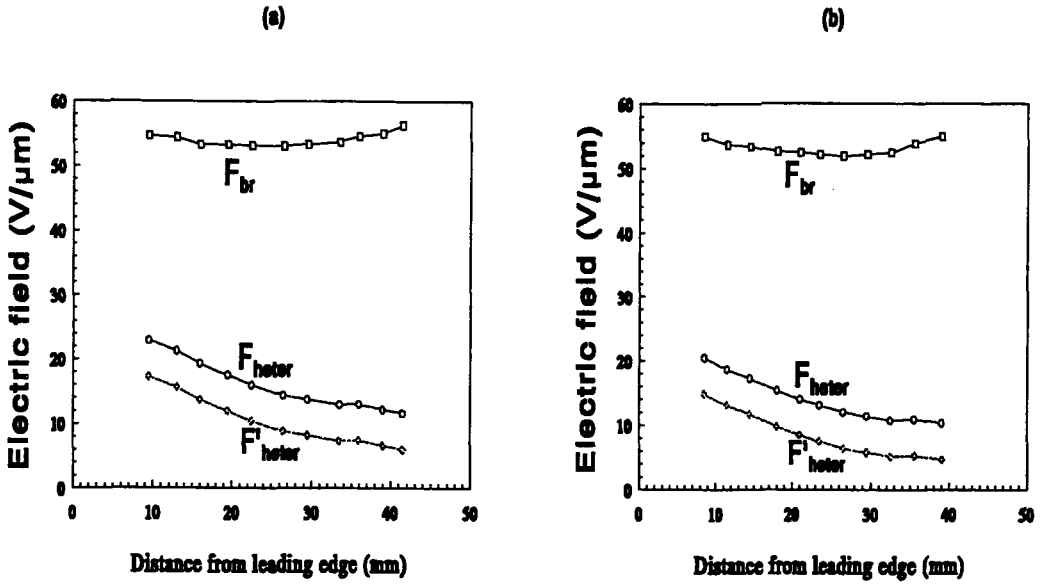

Figure 4.6 The calculated F_{br} and F_{heter} for wafer (a) P555 and (b) P623.

The extraction for individual APDs cannot be independently examined since the uncertainty of the independent measurements for individual APDs using SIMS are too large to reach meaningful conclusion. The validity of this new extraction technique is ultimately decided by future modelling of other characteristics.

The extraction technique described above (which will be called "standard technique") relies on some assumptions and simplifications. Some of them are fairly obvious (items 1-6) and no further discussions are warranted. Some of the assumptions represent the reality of the devices (items 8, 9). The rest of the assumptions and simplifications (items 7, 10, 11) are examined in the next section, and the resulting variations are treated as the errors of this extraction technique.

4.4 Error analysis

One aspect of error analysis is to determine the absolute uncertainty of the extracted values, which is very important for further investigations at the individual device level.

Another aspect is that the errors should be small so that the general trends across the wafer are preserved. The errors can be generally classified into two types: systematic and random. The systematic errors cause the extracted values to change systematically in a predicted direction whereas the random errors cause the extracted values to change in an unpredictable direction. The general trend across the wafer of the extracted values are generally not affected by the systematic errors whereas the absolute uncertainties of the extracted values depend on both the systematic and random errors.

The systematic errors are contributed by ignoring the ionizations in the absorption layer, and the ionization in the charge and grading layers, the assumed zero doping concentration in the multiplication layer, and the selection of InP ionization rates. The random errors are contributed by the experimental errors of V_{mesa} and V_{br}, and the fabrication and calibration errors of the device parameters listed in Table 4.1.

4.4.1 Ionization in the absorption layer

Ionization in the InGaAs absorption layer has long been suspected to be responsible for some unexplained experimental results, such as a lower than expected gain-bandwidth product (GBW) [29][40][80], and also a lower than expected excess noise [32][42]. Ionization in the InGaAs absorption layer will cause systematic errors to the extracted x_d and σ_{active}, and in principle this effect should be included. However, in many cases, it can be ignored when extracting x_d and σ_{active}. In this section, ionization in the InGaAs absorption layer is examined in detail so as to determine 1) the error due to the neglect of this effect; and 2) under what conditions this ionization can be ignored.

To include the ionization in the absorption layer, the right hand side of eqn. (4.3) should be modified to

$$\frac{\alpha_1(F_{br})}{\alpha_1(F_{br})-\beta_1(F_{br})}\exp\left[x_d(\beta_1(F_{br})-\alpha_1(F_{br}))\right]-\frac{\beta_1(F_{br})}{\alpha_1(F_{br})-\beta_1(F_{br})}=$$

$$\exp\left[x_d(\beta_1(F_{br})-\alpha_1(F_{br}))\right]\int_{F'_{heter}}^{F_{end}}\alpha_2(F)\exp\left[\int_{F'_{heter}}^{F}(\beta_2(F')-\alpha_2(F'))\frac{dF'}{dF/dx}\right]\frac{dF}{dF/dx}. \quad (4.9)$$

F_{end} is the electric field at the end of the absorption layer at breakdown, and

$$F_{end}=F'_{heter}-\frac{qN_Dt_{undoped}}{\varepsilon_2\varepsilon_0}. \quad (4.10)$$

dF/dx is the spatial gradient of the electric field in the absorption layer, and it is $(qN_D/\varepsilon_2\varepsilon_0)$ here. α_2 and β_2 in μm^{-1} are the ionization rates for electrons and holes in InGaAs with electric field F in V/μm, and their experimental values have been reported by Pearsall [82] as

$$\alpha_2(F)=5130\cdot\exp(-195/F),\beta_2(F)=7300\cdot\exp(-220/F), \quad (4.11)$$

and by Osaka [32] as

$$\alpha_2(F)=227\cdot\exp(-113/F),\beta_2(F)=395\cdot\exp(-145/F). \quad (4.12)$$

Their values are plotted with F between 15 and 25 V/μm in Figure 4.7. A cautionary note is that for both formulas the valid F range is between 20 to 25 V/μm. Also note that unlike InP, the ionization rate for electrons is larger than the ionization rate for holes in InGaAs.

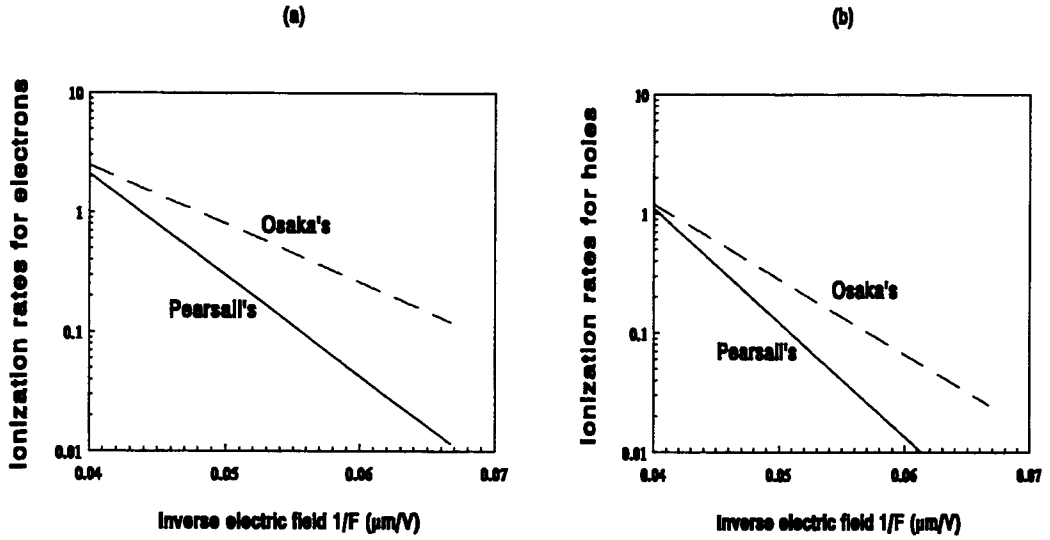

Figure 4.7 The experimental values for the ionization rates in InGaAs for (a) electrons, and (b) holes. The solid lines are from Pearsall, the dashed lines from Osaka.

The extracted x_d and σ_{active} for wafer P555 with both sets of the ionization rates are shown in Figure 4.8. The inclusion of the ionization in the absorption layer clearly makes some difference in the extracted values when the breakdown voltages are high, and makes no difference when the breakdown voltages are low. This is exactly as expected, since at lower breakdown voltages, σ_{active} are higher, which results in lower F'_{heter} (lower than 12 V/μm). Therefore the ionization in the absorption layer is too small, as seen from Figure 4.7. When breakdown voltages are high, σ_{active} are lower, which results in higher F'_{heter} (higher than 15 V/μm). Therefore the ionization in the absorption layer is significant. However, the extracted x_d and σ_{active} from the calculation with Osaka's InGaAs ionization rates, are contradicted by other independent measurements. The trend of x_d and the 52% variation of σ_{active} over the wafer cannot be explained. It seems that Osaka's α_2 and β_2 are not correct when F is below 20 V/μm. However, α_2 and β_2 are determined between 20 to 25 V/μm, and the only conclusion from this investigation is that extrapolation of Osaka's α_2 and β_2 to electric fields below 20 V/μm is not accurate. Therefore, only the results calculated with Pearsall's α_2 and β_2 will be discussed further.

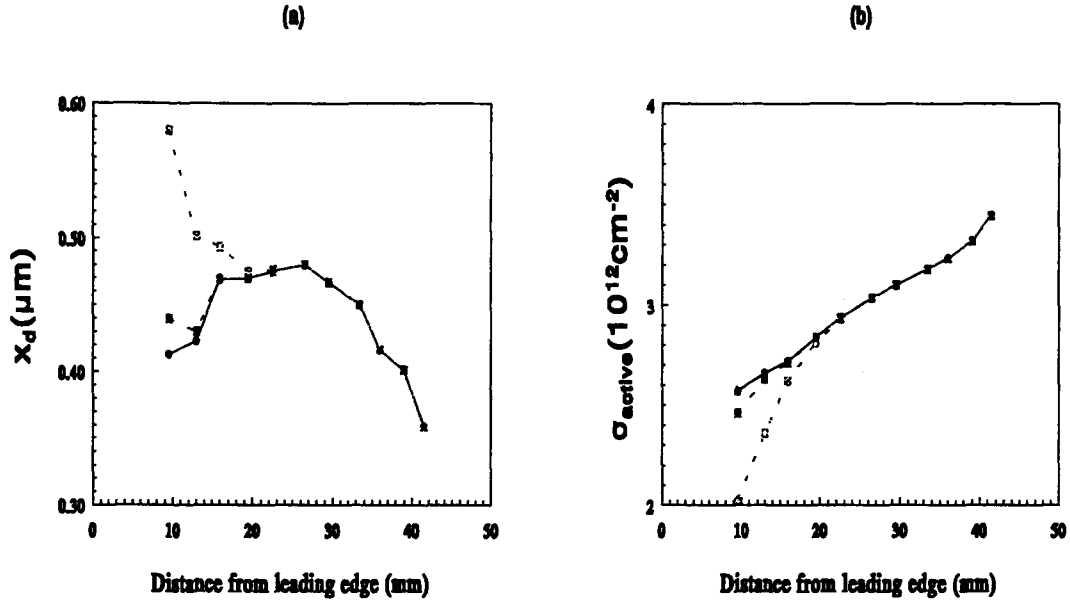

Figure 4.8 The extracted values of (a) x_d and (b) σ_{active} for wafer P555 with the ionization in the absorption layer. The solid lines are extracted with the standard technique. The dotted lines with solid squares are calculated with Pearsall's InGaAs ionization rates, and with open squares with Osaka's InGaAs ionization rates.

From the extraction for wafer P555, it seems that when F'_{heter} is higher than 17 V/μm, the ionization in the absorption layer is significant, and when F'_{heter} is lower than 15 V/μm, the ionization is negligible. For the purpose of a rule of thumb estimation, F'_{heter} of 17 and 15 V/μm correspond to experimental V_{br} of 90 and 80 V, if x_d is 0.4-0.5 μm. It also reveals that this inclusion causes an increase in x_d and a decrease in σ_{active}, when its contribution is important. The inclusion of the ionization in the absorption layer reduces the necessity of the ionization contribution from the multiplication layer, which causes a reduction of F_{br}. However, this reduction of F_{br} will reduce the electric fields in the absorption layer, which will result in a reduction of the ionization contribution from the absorption layer. To compensate for the reduction of the electric fields in the absorption layer, σ_{active} is reduced. The increase of x_d, which has a much smaller effect on the ionization contribution from the multiplication layer than from the reduction of F_{br}, is for maintaining V_{mesa}.

Wafer P623 is also extracted as shown in Figure 4.9(a). The results are almost identical to the values extracted with the standard technique, since σ_{active} is higher for this wafer than wafer P555. This higher σ_{active} results in the values of F'_{heter} lower than 15 V/ μm, as can be seen from Figure 4.9(b).

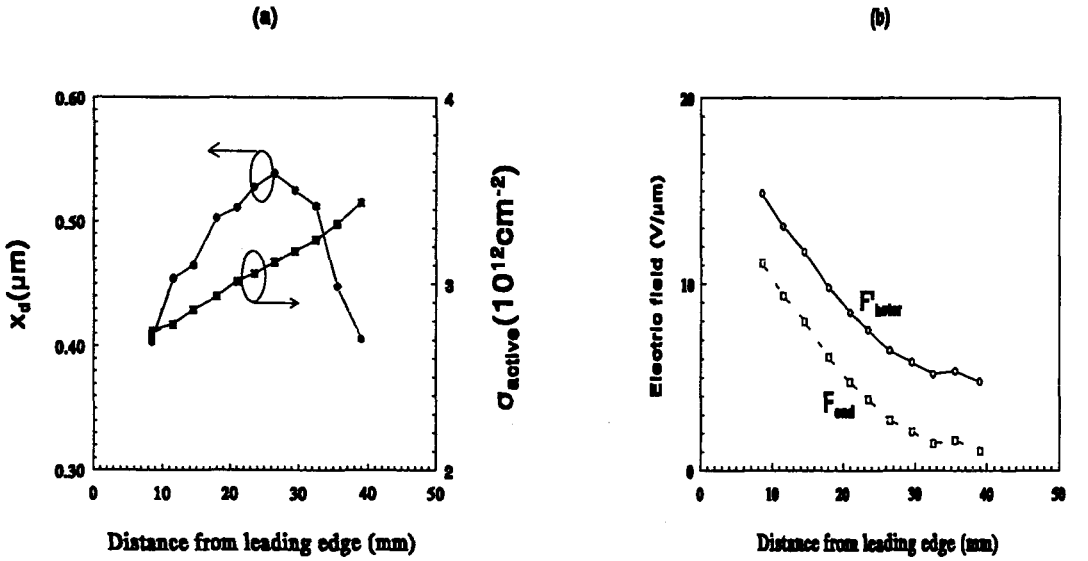

Figure 4.9 The extracted values of (a) x_d and σ_{active}, which are overlapping with the values extracted from the standard technique and, and (b) F'_{heter} and F_{end} for wafer P623, including the ionization in the absorption layer.

4.4.2 Ionizations in the charge and grading layers

In principle, the ionization in both the charge and grading layers ought to be considered together. In this section, it will be demonstrated that the inclusion of the ionization in the charge layer will cause acceptable systematic errors in the extracted x_d and σ_{active}. The systematic errors caused by the inclusion of the ionization in the grading layer is even smaller.

To include the ionization in the charge layer, the right hand side of eqn. (4.3) should be modified to

$$\frac{\alpha_1(F_{br})}{\alpha_1(F_{br})-\beta_1(F_{br})}\exp\left[x_d(\beta_1(F_{br})-\alpha_1(F_{br}))\right]-\frac{\beta_1(F_{br})}{\alpha_1(F_{br})-\beta_1(F_{br})}=$$

$$\exp\left[x_d(\beta_1(F_{br})-\alpha_1(F_{br}))\right]\int_{F_{br}}^{F_2}\alpha_1(F)\exp\left[\int_{F_{br}}^{F}(\beta_1(F')-\alpha_1(F'))\frac{dF'}{dF/dx}\right]\frac{dF}{dF/dx}. \quad (4.13)$$

F_2 is the electric field at the boundary between the charge and grading layers, and

$$F_2 = F_{br}-\frac{q\sigma_{charge}}{\varepsilon_2\varepsilon_0}. \quad (4.14)$$

dF/dx is the spatial gradient of the electric field in the charge layer, and is $(q\sigma_{charge}/\varepsilon_1\varepsilon_0 t_{InP})$ here.

The inclusion of the ionization in the charge layer causes a systematic increase of 0.011 - 0.024 μm in the extracted x_d, and a systematic decrease of (0.05-0.1)×10^{12} cm^{-2} in the extracted σ_{active}, as shown in Figure 4.10 for both wafers. This phenomenon is quite similar to the inclusion of the ionization in the absorption layer as discussed above, except that the effect of the ionization in the charge layer will be important for all the values of σ_{active}, since the electric field in the charge layer is not a strong function of σ_{active}. It should be noted that even if the ionization in the charge layer can be treated as a systematic error in the device parameters extraction, it does not necessarily mean that the effect can be treated as a second order effect in modelling other characteristics.

4.4.3 Non-zero doping concentration in the multiplication layer

Principally, the electric field in the multiplication layer is not constant due its non-zero background doping concentration. It will be demonstrated that this effect will cause negligible systematic errors in the extracted x_d and σ_{active}.

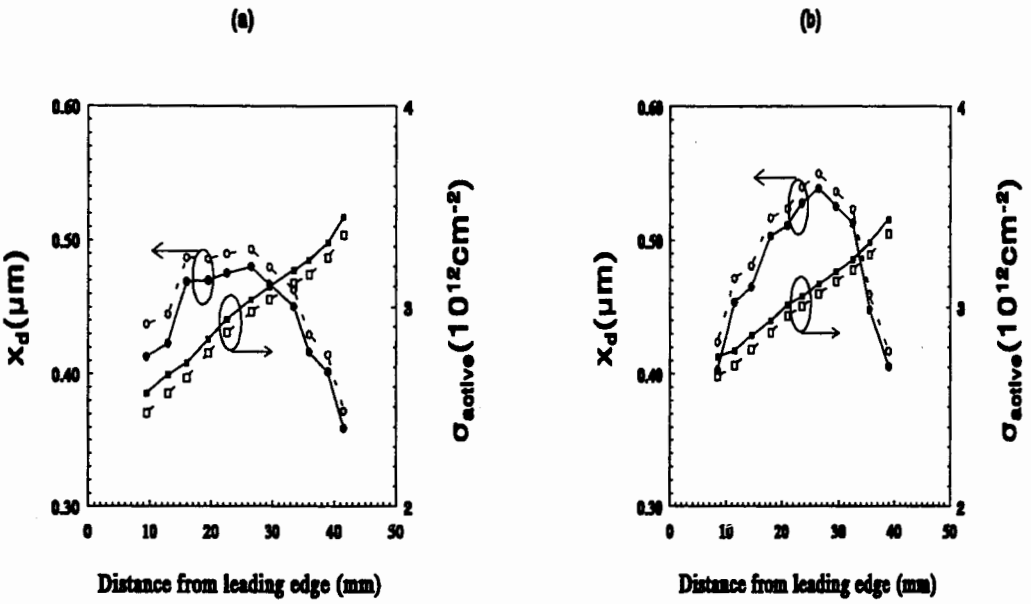

Figure 4.10 The extracted values of x_d and σ_{active} (the dotted lines with open symbols) with the ionization in the charge layer for wafer (a) P555 and (b) P623. The solid lines with closed symbols are extracted from the standard technique.

To include this effect, eqn. (4.1) and eqn. (4.2) should be modified to (Appendix A)

$$V_{mesa}+V_{bi}=\frac{qN_D(x_d^2/2)}{\varepsilon_0\varepsilon_1}+\frac{q\sigma_{charge}}{\varepsilon_0\varepsilon_1}(x_d+t_{InP}/2)+\frac{qN_G t_{grading}}{\varepsilon_2\varepsilon_0}(x_d+t_{InP}+t_{grading}/2), \tag{4.15}$$

$$\begin{aligned}V_{br}+V_{bi}=F_{br}(x_d+t_{InP}+t_{grading}+t_{undoped})-\frac{q\sigma_{charge}}{\varepsilon_1\varepsilon_0}(t_{InP}/2+t_{grading}+t_{undoped})\\ -\frac{qN_G t_{grading}}{\varepsilon_2\varepsilon_0}(t_{grading}/2+t_{undoped})-\frac{q\sigma_{InGaAs}}{\varepsilon_2\varepsilon_0}t_{undoped}-\frac{qN_D t_{undoped}^2/2}{\varepsilon_2\varepsilon_0}\\ -\frac{qN_D x_d}{\varepsilon_1\varepsilon_0}(x_d/2+t_{InP}+t_{grading}+t_{undoped}).\end{aligned} \tag{4.16}$$

The breakdown condition becomes

$$1-\int_{F_{br}}^{\left(F_{br}-\frac{qN_D}{\varepsilon_0\varepsilon_1}x_d\right)}\alpha_1(F)\exp\left[\int_{F_{br}}^{F}(\beta_1(F')-\alpha_1(F'))\frac{dF'}{dF/dx}\right]\frac{dF}{dF/dx}=0, \tag{4.17}$$

where dF/dx is the spatial gradient of the electric field in the multiplication layer, and it is $(qN_D/\varepsilon_2\varepsilon_0)$ here. The two eqn. (4.7) and eqn. (4.8) should be modified to

$$F_{heter} = F_{br} - \frac{q\sigma_{charge}}{\varepsilon_0\varepsilon_1} - \frac{qN_G}{\varepsilon_0\varepsilon_1}t_{grading} - \frac{qN_D}{\varepsilon_0\varepsilon_1}x_{d,} \tag{4.18}$$

$$F'_{heter} = F_{br} - \frac{q\sigma_{charge}}{\varepsilon_0\varepsilon_1} - \frac{qN_G t_{grading}}{\varepsilon_0\varepsilon_1} - \frac{q\sigma_{InGaAs}}{\varepsilon_0\varepsilon_2} - \frac{qN_D}{\varepsilon_0\varepsilon_1}x_d \equiv F_{heter} - \frac{q\sigma_{InGaAs}}{\varepsilon_0\varepsilon_2}. \tag{4.19}$$

The inclusion of the non-zero doping concentration in the multiplication layer causes a negligible systematic increase of less than 0.0006 μm in the extracted x_d, and a decrease of less than $0.018\times10^{12}cm^{-2}$ in the extracted σ_{active}, as shown in Figure 4.11 for both wafers.

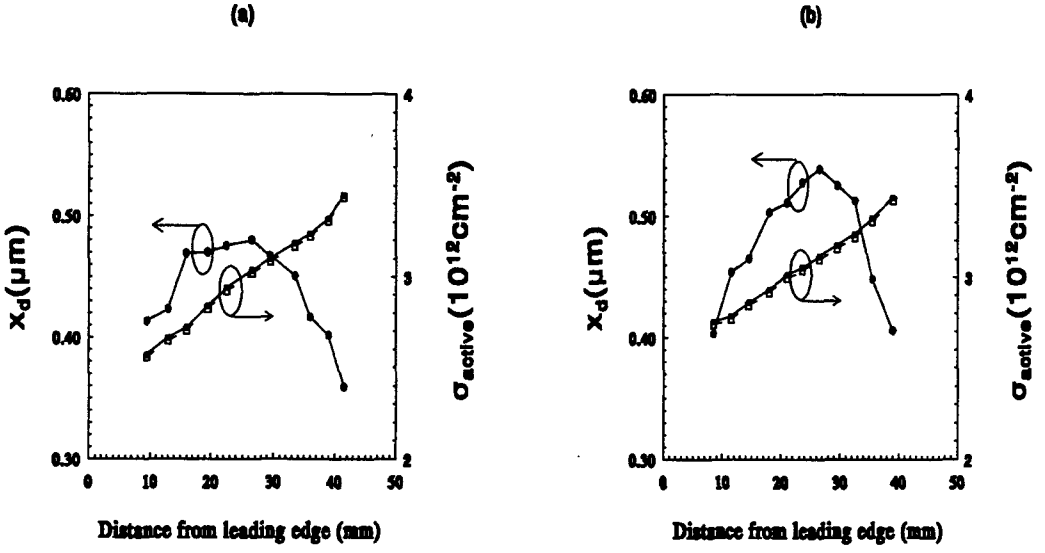

Figure 4.11 The extracted values of x_d and σ_{active} (dotted lines with open symbols) with the non-zero doping in the multiplication layer for wafer (a) P555 and (b) P623. The solid lines with closed symbols are extracted from the standard technique.

4.4.4 InP ionization rates

The selection of the InP ionization rates is of potential importance for the absolute accuracy of the extracted x_d and σ_{active}. There are substantial differences in reported experimental values α_1 and β_1 from Osaka's [32] used so far and others, such as from Umebu's [83],

$$\alpha_1(F) = 736 \cdot \exp(-345/F), \beta_1(F) = 204 \cdot \exp(-242/F), \quad (4.20)$$

from Cook's [84] for F between 36 and 56 V/μm,

$$\alpha_1(F) = 293 \cdot \exp(-264/F), \beta_1(F) = 162 \cdot \exp(-211/F), \quad (4.21)$$

and from Armiento's [85],

$$\alpha_1(F) = 555 \cdot \exp(-310/F), \beta_1(F) = 321 \cdot \exp(-256/F). \quad (4.22)$$

They are plotted with F between 50 and 60 V/μm in Figure 4.12 in order to both impress upon the reader the differences and to guide the reader through the discussion that follows. Note that Armiento's values, α_1, are identical to Osaka's and Armiento's values, β_1, are quite similar to Osaka's.

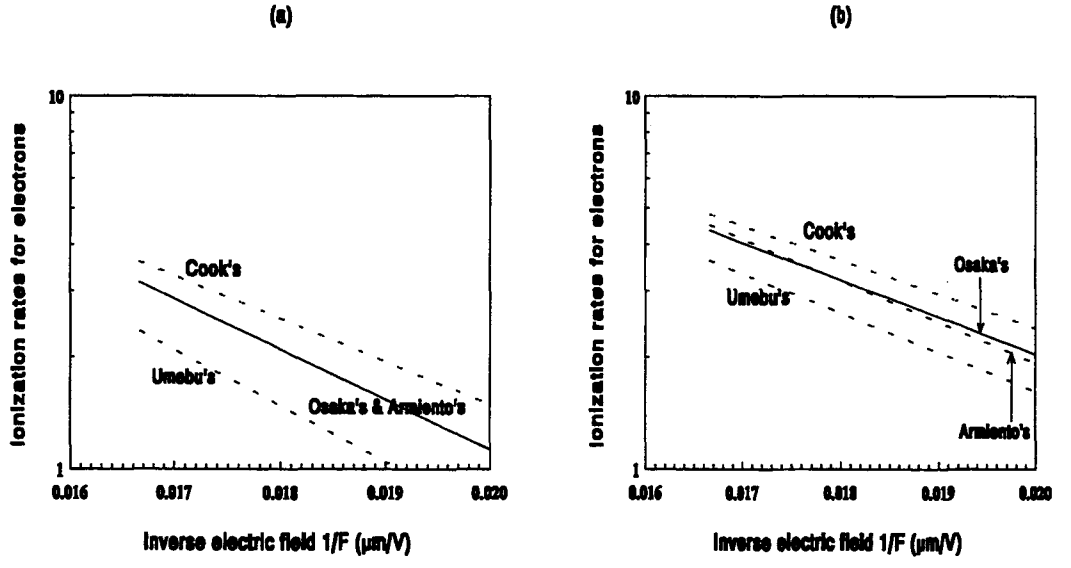

Figure 4.12 The experimental values for the ionization rates in InP for (a) electrons, and (b) holes from the literature.

The extracted x_d and σ_{active} for both wafers with Umebu's and Cook's InP ionization rates are plotted in Figure 4.13. Note that all the extracted F_{br} are within the valid F range of the corresponding set of the InP ionization rates. Since Armiento's values of α_1 and β_1 are quite similar to Osaka's, there is little difference if Armiento's values of α_1 and β_1 are used. Compared to the standard technique, using Umebu's values of α_1 and β_1 causes a

typical decrease of 0.06 μm of the extracted x_d and 0.3×10^{12} cm^{-2} increase of the extracted σ_{active}, while using Cook's values of α_1 and β_1 causes a typical increase of 0.05 μm and a decrease of 0.2×10^{12} cm^{-2}, respectively. There are a few reasons to discard both the extractions using Umebu's and Cook's values of α_1 and β_1. One of the reasons is that the two calculations result in exactly opposite extracted values of x_d and σ_{active}, and one of the two must be wrong. Osaka's values of α_1 and β_1 are more up-to-date and most frequently used in the recent literature. Finally, the extracted values are most important in the sense of self consistency, and the selection of different InP ionization rates may not be very critical in modelling other characteristics of the APDs. Therefore, Osaka's InP ionization rates are used for the calculations in this investigation.

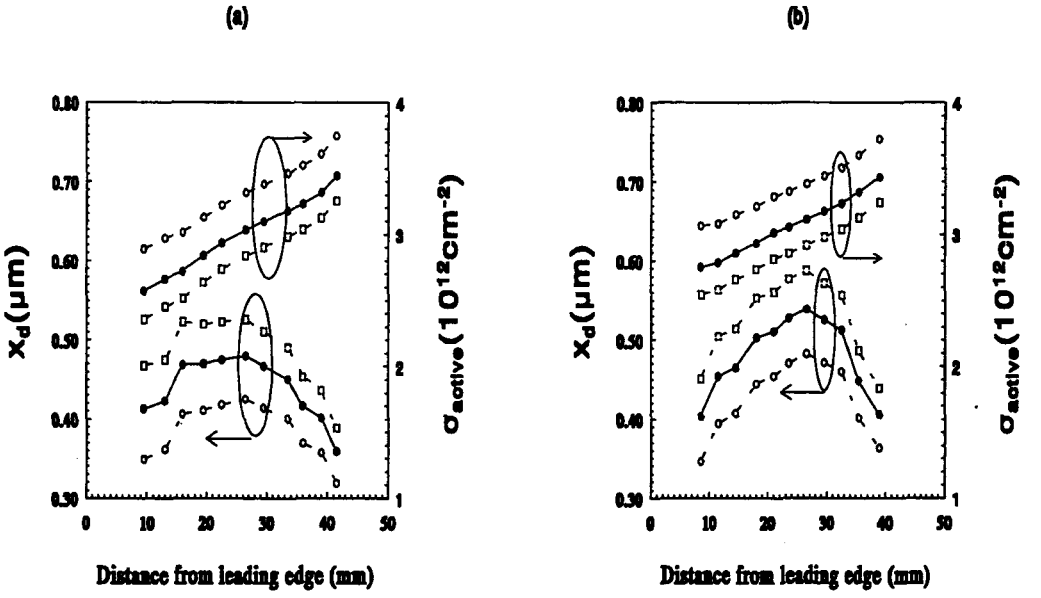

Figure 4.13 The extracted values of x_d and σ_{active} for wafer (a) P555 and (b) P623 with the InP ionization rates from Umebu's (the dotted lines with open circles) and Cook's (the dotted lines with open squares). The solid lines with closed symbols are extracted from the standard technique.

4.4.5 Random errors

The random errors are contributed by the experimental errors of V_{mesa} and V_{br}, and the fabrication and the calibration errors of the device parameters used in the extraction,

such as t_{InP}, $t_{grading}$, $t_{undoped}$, N_G, N_D and σ_{InGaAs}, that are listed in Table 4.1. The maximum errors corresponding to each contributing source are listed in Table 4.2. The uncertainties in V_{mesa} and $t_{undoped}$ are the dominant contributing sources to the total random errors, and the value for x_d is approximately ±0.05 μm, and for σ_{active} approximately $\pm 0.09 \times 10^{12}$ cm^{-2}. The total random error for σ_{active} is clearly small enough that the trend for both wafers is preserved. The total random error for x_d, which is calculated in the worst case, principally is large enough to smear out the trend of both wafers. However, the reflectance spectroscopy clearly established that the trend shown is correct, and thus the worse case is not likely occurring. In addition, the uncertainties of V_{mesa} and $t_{undoped}$ are most likely to be on one side rather than random, which will result in systematic rather than random uncertainties, thus preserving the trend over the wafer. However, it is not certain on which side these two errors are, and therefore they are still treated as random errors here.

Table 4.2 The random errors of the extracted x_d and σ_{active}. The thickness is in μm, the doping concentration is in 10^{15} cm^{-3}, and the integrated areal charge density is in 10^{12} cm^{-2}.

Contributor	V_{mesa}	V_{br}	t_{InP}	$t_{grading}$	N_G	σ_{InGaA}	$t_{undoped}$	N_D
Default	See Figure 4.4.		0.17	0.09	10	0.4	3.8	0.7
Uncertainty	±1	±1	±0.009	±0.005	±2.5[a]	±0.05	±0.2	±0.07
δx_d	±0.04	±0.005	∓0.008	∓0.001	∓0.002	±0.01	∓0.02	±0.004
$\delta\sigma_{active}$	∓0.05	∓0.005	±0.02	±0.004	±0.004	∓0.01	±0.07	∓0.02

a. The doping in the grading layer is not independently monitored.

4.4.6 δ-doped SA(G)CM APD

It would be rewarding to use an even simpler model to conduct the extraction, such as the simplified δ-doping structure model [75][80]. The formula is similar to the standard technique if it is assumed that $t_{InP} = t_{grading} = 0$ and $N_D = 0$. The extracted values with this simple model are surprisingly close to the extracted values with the standard

technique. x_d is increased by less than 0.04 μm and σ_{active} is decreased by less than 0.08×10^{12} cm^{-2}. However, this obvious success does not necessarily qualify this simple model as appropriate for more general cases. To examine its validity, a better model with $N_D \neq 0$ is used to do the extraction. Not surprisingly, this "better" model causes an unacceptable 0.06 μm increase of x_d and 0.23×10^{12} cm^{-2} decrease of σ_{active}. Obviously, the two simplifications in the simple model cause similar but opposite systematic errors to x_d and σ_{active}. Physically, the δ-doping simplification reduces the voltage drop in the charge and grading layers because of the zero thicknesses, and fortuitously, the $N_D = 0$ simplification increases the voltage drop in the absorption layer because the increased electric fields in the absorption layer. For quantitative modelling, caution should be exercised when the δ-doping structure model is used.

4.5 Summary

In this chapter, a novel, fast, accurate, and non-destructive technique has been invented to extract the two most critical device parameters in the SAGCM APDs - x_d and σ_{active}. To the author's best knowledge, the innovative use of V_{mesa} obtained from simple DC photocurrent measurements in this technique is novel. The technique is tested on two wafers, and the extracted values agree very well with the independent measurements within both the experimental and extraction errors.

The systematic errors have been considered in detail. The ionization in the absorption layer is found to cause significant errors only when F'_{heter} is higher than 17 V/μm; that is, x_d is increased by ~ 0.03 μm and σ_{active} is decreased by ~ 0.1×10^{12} cm^{-2}. The corresponding V_{br} is about 90 V if x_d is 0.4-0.5 μm. This effect is negligible for 90% of the APDs from a wafer. Also, it is found that for further modelling, Pearsall's rather than Osaka's InGaAs ionization rates are more consistent with this model and the experimental results.

The simplification of the zero doping concentration in the multiplication layer is found to cause very small systematic errors. The selection of either Umebu's or Cook's InP ionization rates is found to cause large systematic errors, but in opposite directions. It has been argued that the best choice for the extraction and further investigations are Osaka's values.

The largest systematic error is contributed by the simplification of no ionization in the charge layer. x_d is increased by less than 0.03 μm and σ_{active} is decreased by less than 0.1×10^{12} cm^{-2}. The combination of this simplification, and the simplification of no ionization in the absorption layer will cause an unacceptable error 0.2×10^{12} cm^{-2} in σ_{active} when V_{br} is larger than 90 V. However, for the overwhelming majority of the APDs, the systematic errors are acceptable, and are dominated by the simplification of no ionization in the charge layer.

The random errors are contributed by the experimental errors of V_{mesa} and V_{br}, and by the fabrication and calibration errors of the device parameters used in the extraction. The uncertainties in V_{mesa} and $t_{undoped}$ are the dominant contributing sources of the random errors, and the overall random error for x_d is about ±0.05 μm, and for σ_{active} about $\pm0.09\times10^{12}$ cm^{-2}.

This technique is applicable to SAM and SAGM APDs to some extent with the modification that the multiplication layer is heavily doped. The critical device parameters in those devices are the doping concentration and the thickness of the multiplication layer. However, it will be less accurate since the electric fields in the multiplication layer change significantly over the layer. The physical model established here is very useful for further investigations on the planar SAGCM InP/InGaAs APDs, and the extraction technique makes it possible to conduct detailed quantitative modelling.

Chapter 5 Photogain

In the previous chapter, a detailed description of a new technique to extract some critical device parameters was given. The next step in the process is to use the extracted and known device parameters of the APDs for prediction of important performance characteristics, such as DC multiplication gain (photogain), breakdown voltage, bandwidth, and noise. In this chapter, the photogain versus bias voltage (M-V) characteristics for a number of devices are investigated. The Miller empirical formula [89][90] invented for Si and Ge M-V characteristics is applied for the first time to the M-V characteristics of the SAGCM InP/InGaAs APDs. A physical model is developed to interpret the experimental M-V characteristics, and possible improvements/confirmations to the device parameter extraction technique are also discussed.

5.1 Introduction

Analytical expressions of the M-V characteristics are very useful when estimating the bias voltage required for a particular operating M. They also make possible the derivation of analytical expressions for the differentiation of M with respect to V required to extract the ionization rates, since numerical differentiation may introduce unwanted spikes and noise. With an analytical expression for the M-V characteristics, it is also possible to investigate gain saturation effects, such as those due to parasitic and load resistances, space charge, and heating. The well-known Miller empirical formula for the M-V characteristics in APDs has been used successfully in the cases of Si [90] and Ge [89] APDs. However, this formula has never been investigated systematically for InP-based APDs. In addition, the Miller formula makes it possible to extract the true experimental breakdown (at which the current through the device is infinite). In some cases, it is possible to deter-

mine if the breakdown is truly due to impact ionization or to some other mechanism such as tunneling, as shown soon.

It is relatively simple to physically model the M-V characteristics for an arbitrary electric field variation and distribution of injected carriers with eqn. (2.10) when the electron and hole ionization rates are known, as in the case of Si [87]. As a matter of fact, the electron and hole ionization rates are determined by the inverse of this procedure under the condition of pure electron and hole injections [56]. The determination of the electron and hole ionization rates in InP was performed from a differentiation of M-V curve [83][84][85][86]. Therefore, they cannot be translated directly into an M-V curve without some assumptions regarding quantum efficiency and unity gain [86].

Photogain versus bias voltage, along with breakdown voltage, bandwidth and noise, are the most critical performance characteristics of APDs. Thus, it is important to theoretically predict the M-V characteristics. However, physical modelling of the M-V characteristics in InP-based SA(GC)M APDs has never been done before, except that the M-V characteristics of SAGM InP/InGaAs APD have been calculated as a consistency check [26][27] with the doping concentration in the multiplication layer taken as an adjustable parameter to provide a better fit. Therefore, calculation of the M-V characteristics will be a good test of the device parameter extraction technique discussed above, and it may even offer some insights into possible improvements to the extraction technique.

Planar SAGCM InP/InGaAs APDs are almost ideal for studying the M-V characteristics as it is shown soon. However, two obstacles must be overcome when dealing with M-V characteristics in any type of APDs. One is how to define unity gain, and the other is how to maintain a constant primary photocurrent (quantum efficiency) throughout the bias voltages, or how to calculate it when it is voltage dependent. The photogain M in planar SAGCM InP/InGaAs APDs is conveniently self-calibrated and the quantum efficiency

does not change with bias voltage. The gain of other types of InP/InGaAs APDs must be calibrated with another photodiode or, unity gain is defined at an arbitrary low voltage, or at punchthrough voltage V_{mesa} in mesa SAM InP/InGaAs APDs [18][24], which is not necessarily correct [39]. For voltage dependent quantum efficiency in APDs, complicated baseline fitting must be employed to account for this effect [86]. The calibration of M and baseline fitting not only make the theoretical model more complicated, but more importantly, they introduce extra large uncertainties.

As discussed below, the primary photocurrent (quantum efficiency) for the planar SAGCM InP/InGaAs APDs is independent of the bias voltage for the voltage range $V > V_{ann}$, and M is indeed unity when $V_{ann} < V < V_{mesa}$, as shown in Figure 4.2.

When $V_{ann} < V < V_{mesa}$, the periphery region of the InGaAs absorption layer is depleted whereas the central active region is not. The energy barrier at the InP/InGaAs heterointerface in the central active region still blocks the holes photo-generated in the absorption layer from passing. Because of the very high quality of the InGaAs semiconductor, the hole lifetime is about 18.5 μs and the diffusion length is about 140 μm [79]. Therefore, the long-lived photo-generated electron-hole pairs in the central active region can diffuse laterally to the periphery region, and are collected by the terminals since the energy barrier in the periphery region is diminished. The photocurrent is constant over this range, and the gain is unity since at these low bias voltages the gain is due to impact ionization in the periphery region. This is strongly supported by the experimental photocurrent. Should the gain not be unity within this bias range, the photocurrents would not be constant. It should be noted that the multiplication gain due to the impact ionization in the central region is not necessarily unity. However, this multiplication gain is irrelevant to the photocurrent since the photocurrent does not flow through the central active region at all. This is one of the very unique features of planar SAGCM APDs with partial charge sheet in the periph-

ery as the photogain is calibrated automatically in this bias range. The existence of the unity gain bias voltage region is only observed in our high quality planar SAGCM APDs with partial charge sheet in device periphery, or high quality planar SAGM InP/InGaAs APDs with preferential lateral extended guard (PLEG) ring [25].

When $V > V_{mesa}$, the energy barrier in the active central region is diminished, and the photo-generated holes can pass through the central active multiplication region. In the case of a completely depleted absorption layer ($V > V_{depleted}$, $V_{depleted}$ is about 10-15 V higher than V_{mesa}), the holes photo-generated in the absorption layer drift through the central region. In the case of an incompletely depleted absorption layer, the holes photo-generated in the undepleted absorption region diffuse vertically along the central regions, since it is much shorter than to diffuse to the periphery region. Both the holes diffusing to the depleted absorption region, and the holes photo-generated in the depleted absorption region are collected through the central region. Therefore, when $V > V_{mesa}$, all the holes photo-generated in the absorption layer are collected through the central region, and the primary current is the same as when $V_{ann} < V < V_{mesa}$. However, the energy barrier at the InP/InGaAs interface in the central region does not disappear at $V = V_{mesa}$. The energy barrier at the heterointerface may prevent the hole current flow through the central region. In this case, the blocked holes will diffuse laterally to the periphery and are collected through the periphery region.

Let's estimate this extra voltage above V_{mesa} required to eliminate this hole blockage completely. The valence band discontinuity of InP/InGaAs junction is about 0.36 V, which spreads over the thickness of the grading layer. Therefore, the electric field at the hetero-interface F_{heter} of $0.36V/0.1\mu m = 3.6V/\mu m$ is approximately strong enough to eliminate this energy barrier. This means that an extra 3 V above V_{mesa} will eliminate this hole blockage caused by this energy barrier. It should be noted that this phenomenon is different from

hole trapping phenomena, which is an high frequency phenomenon. Therefore, when $V > (V_{mesa} + 3V)$, the primary current through the central active region does not change with bias voltage and is the same as the primary current (through the periphery region) when $V_{ann} < V < V_{mesa}$. It should be also noted that when $V > (V_{mesa} + 3V)$ the multiplication gain in the periphery region does not contribute to the photocurrent since the photocurrent does not flow through it and the gain may not be unity. The photocurrent and its differentiation with respect to V starts to increase monotonically due to the increased impact ionization multiplication until the bias voltage reaches the avalanche breakdown voltage V_{br}. The existence of the unity gain and the voltage independent quantum efficiency in our devices make it possible to calculated the photogain directly, as shown in Fig. 2, and more importantly, they make empirical and physical modelling more reliable.

Another important advantage of SAGCM APDs is that the electric field in the multiplication layer is uniform. This significantly simplifies the mathematics involved. More importantly, it eliminates the complicated dead space correction encountered in conventional APDs with a heavily doped multiplication layer [88]. All these advantages allow for a more accurate modelling of the M-V characteristics in planar SAGCM InP/InGaAs APDs.

5.2 Empirical formula

5.2.1 Theory

The Miller empirical formula is given by

$$M = \frac{1}{1 - (V/V_B)^r}, \tag{5.1}$$

where V_B is an adjustable breakdown voltage, and r is an adjustable positive power coefficient. The formula is numerically displayed in Figure 5.1 for different r values. V_B is dif-

ferent than the experimental V_{br} which is defined as the voltage at which the photocurrent is ~ 10 μA. Certainly, V_B is the most appropriate breakdown voltage from the physical point of view. However, V_{br} is usually only 0.5 V smaller than V_B, and both of them may be used interchangeably. To fit the experimental data, it is better to fit

$$\log(1 - 1/M) = r\log(V/V_B), \tag{5.2}$$

which can be performed conveniently as a linear regression.

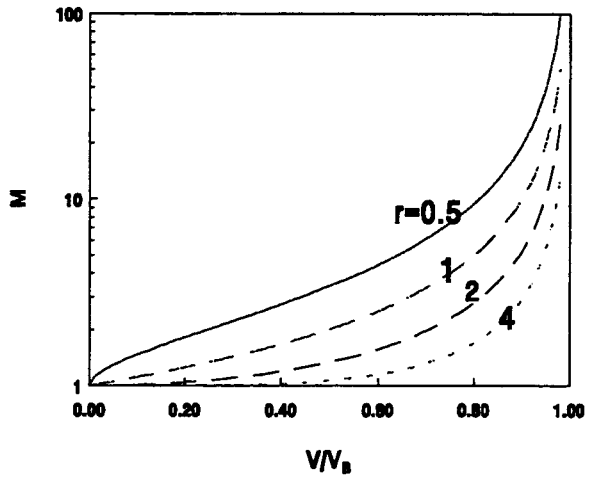

Figure 5.1 Empirical formula for M-V characteristics with different r.

5.2.2 Results and discussions

Photocurrents (photogains) versus bias voltage for 9 APDs from wafer P623 were measured. These 9 APDs showed different V_{br} and can be divided into four groups according their V_{br} and V_{mesa}, besides APD4. In fact, two APDs in each group are from the same area on the wafer. Each experimental M-V characteristics is fitted to the Miller empirical formula with 95% confidence, and the results are given in Table 5.1. The uncertainty for V_B is ~ 0.02 V, and for r, it is less than 0.006 for all the APDs.

Table 5.1 The fitted parameters for 8 APDs from wafer P623. All voltages are in volts.

APD#	4	14	37	32	31	13	36	34	35
V_{mesa}	21.2	25.8	25.4	24.8	25.0	14.6	15.0	20.6	20.2
V_B	37.41	46.50	45.84	56.62	55.50	70.00	68.45	70.44	71.22
r	0.640	0.880	0.732	0.993	1.020	1.343	1.372	1.443	1.403

One of the typical fits (APD32) is illustrated in Figure 5.2. The fit is very well from V_{mesa}+3V to $V_{br,}$ and V_B is only about 1 V higher than V_{br}. The extra 3 V is required to completely eliminate the hole blockage, and it confirms the estimate as given above. However, the estimation is done for the most optimized condition; that is, there are no other photocurrent shunt flow paths, and no other hole recombinations at the heterointerface (for example, due to interface defects). As a matter of fact, in some devices, up to 5 V extra bias voltage is required to eliminate the hole blockage. Therefore, to be consistent, all the fittings are done to data points for M>5. In addition, the higher photogain region is more relevant to the APD's design requirement. Even though the fit of log(1-1/M) does not agree to the experimental data at lower gains from the graph, it does not undermine the integrity of empirically fitting M-V characteristics, as can be seen from the M-V curves. This fitting is also performed on some APDs from wafer P624 (APD27, APD28, APD29, and APD30), and very satisfactory results are obtained.

One of the 10 APDs examined (APD 5, which is not listed in Table 5.1) has an abnormal value of extracted r (0.41) as shown in Figure 5.2, a value much smaller than the value of r for the other APDs (r ~ 1) with comparable breakdown voltage. In this case, a non-zero gain will be extrapolated at zero bias voltage for this experimental M-V characteristic. The reason remains elusive. This implies that fitting to the Miller empirical formula may even be useful for monitoring the measurements.

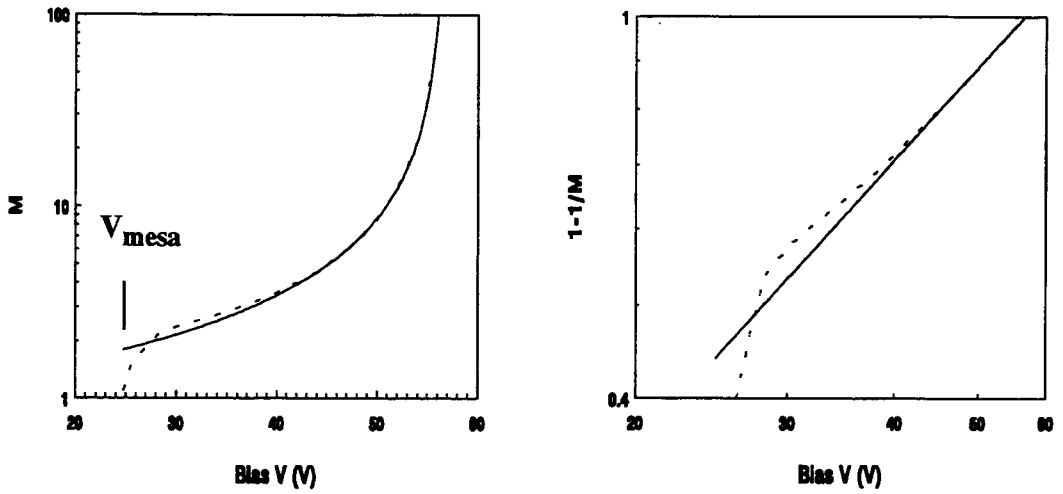

Figure 5.2 A typical fitted M-V characteristics (APD32) to the Miller empirical formula for M>5 data. The solid and dashed lines are the fitted and experimental characteristics, respectively. (a) M-V. (b) (1-1/M) - V.

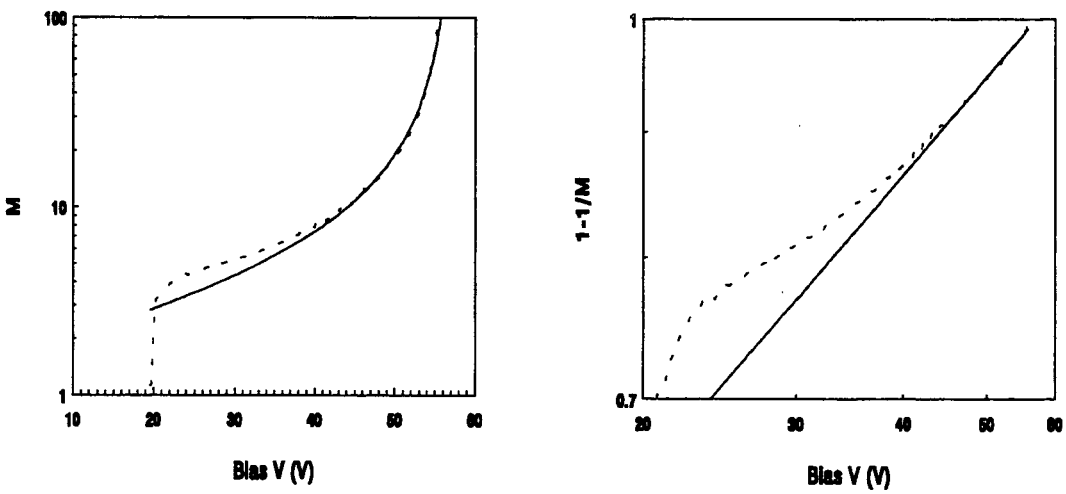

Figure 5.3 A fitted M-V characteristics (APD5) to the Miller empirical formula with unreasonable r (0.41). The solid and dashed lines are the fitted and experimental characteristics, respectively. (a) M-V. (b) (1-1/M) - V.

Because r does not have clear physical meaning, an empirical r-V_{br} relation between r and V_{br} is useful for device screening and modelling. V_{br} is chosen since it is probably the most easily and frequently measured quantity of APDs. Plotting r versus V_{br}, the APDs studied results in the graph shown in Figure 5.4, and this includes the APDs from both wafer P623 and P624. Form the plot, an empirical linear relation between r and V_{br} can be obtained as

$$r = (-0.06 \pm 0.13) + (0.020 \pm 0.002)\, V_{br} \,. \tag{5.3}$$

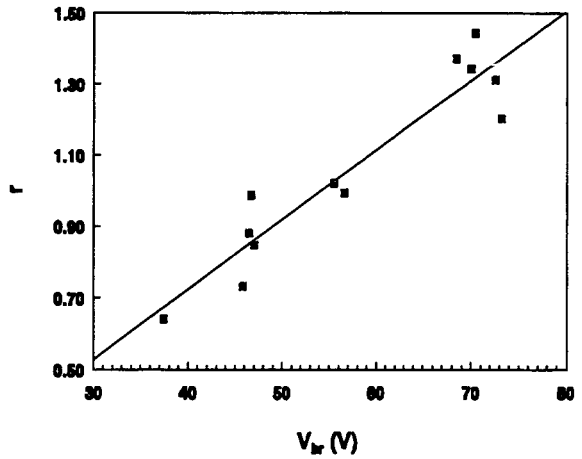

Figure 5.4 Empirical relation between r and V_{br}. The symbols are from the APDs, and the solid line is eqn. (5.3).

To examine the merit of this empirical r-V_{br} relation, two APDs with extracted r values that deviated most from the empirical relation r-V_{br} shown in Figure 5.4 were selected, and the new M-V characteristics were recalculated using r values obtained from the empirical r-V_{br} relation with V_{br} as input parameters, and the results are shown in Figure 5.5(a) and (b) respectively. The difference between r obtained from the empirical r-V_{br} relation and the experimentally extracted r is ~ 0.1. It causes little change for the APD (APD34) with higher V_{br} (70V), while it causes visible change for the APD (APD37) with lower V_{br} (46V). This occurs because the M-V characteristics for APDs with lower r values (lower V_{br}) are more sensitive to a variation of r than for APDs with higher r values

(higher V_{br}). Therefore, r obtained from the empirical r-V_{br} relation can reproduce well the experimental M-V characteristics for the APDs with V_{br} larger than 60 V. As for APD37, the discrepancy in bias voltage corresponding to M=5 and 10 is 0.8 and 0.6 V respectively, and the discrepancy in M for V=0.9V_{br} is 2 (M=13), which is caused by the steep slope there. Therefore, it is still reasonably accurate to estimate the bias voltage for M=10 even for APDs with V_{br} less than 60 V.

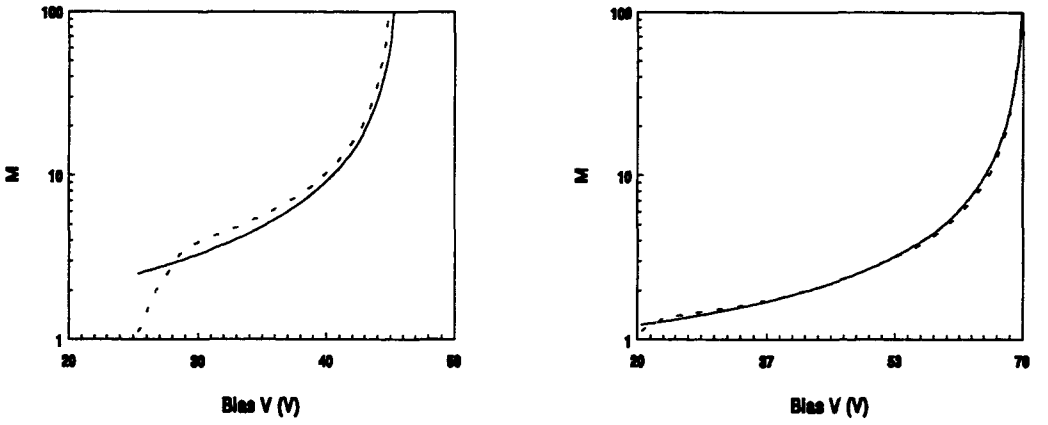

Figure 5.5 The re-calculated M-V characteristics with Miller empirical formula, using r obtained from r -V_{br} empirical relation (eqn. (5.3)). (a) APD37, r=0.857. (b) APD34, r=1.349.

One of the design objectives is to have lower operating voltages. Thus, it is important to design APDs with low breakdown voltages. Since r generally increases with V_{br}, the normalized voltage V/V_{br} is lower for the APDs with lower values of V_{br} than for the APDs with higher values of V_{br} for achieving the same photogain M, as can be seen from Figure 5.1. Therefore, it is more beneficial to design APDs with lower breakdown voltages since this translates to even lower operating voltages. For Si APDs, r has been found to range between 1.9 and 4.0 (with V_{br} between 34 and 48 V), which are significantly higher than the r values found here. This means that M is lower in Si APDs than in SAGCM InP/InGaAs APDs at a same normalized voltage, and this is mainly due to different ionization rates in Si and InP.

It appears that gain saturation effects [56] such as parasitic and load resistances, space charge effect, and heating are not important, at least to the maximum gain of 100 with light input power of approximately 0.1 μW. These gain saturation effects can be combined analytically as a series resistance, but the calculation discussed above does not need this series resistance to reproduce the experimental M-V characteristics. The reason for this is that the photocurrent is 10 μA at breakdown, and therefore, a 50 kΩ series resistance is needed to make some difference, but such a large resistance is highly unlikely.

Even though the Miller empirical formula can account for the general features of the M-V characteristics, deeper insight of the M-V characteristics requires a physical model. In addition, the empirical r-V_{br} relation has only been tested on APDs with a relatively smaller range of x_d (0.4-0.6 μm), and it may not be adequate to describe the M-V characteristics of APDs with significantly different values of x_d. A physical model will not suffer from such limitations.

5.3 Physical model

5.3.1 Theory

Physical modelling of M-V characteristics can be derived easily from the general formulas presented in chapter 2. With the identical assumptions and simplifications as in the standard technique for device parameter extraction, the electric field in the InP multiplication layer at bias V is given by

$$F_{InP}(V) = \begin{cases} \dfrac{V + V_{bi} + \dfrac{q\sigma_{charge}}{\varepsilon_1\varepsilon_0}(x_d + t_{InP}/2) + \dfrac{qN_G t_{grading}^2}{2\varepsilon_2\varepsilon_0}}{x_d + t_{InP} + t_{grading}} & V_{mesa} < V < V'_{mesa} \\ \dfrac{q\sigma_{charge}}{\varepsilon_1\varepsilon_0} + \dfrac{qN_G t_{grading}}{\varepsilon_2\varepsilon_0} + \dfrac{q\sigma_{InGaAs}}{\varepsilon_2\varepsilon_0} + \dfrac{qN_D t_{undoped}}{\varepsilon_2\varepsilon_0} \cdot \dfrac{t(V)}{t_{undoped}} & V'_{mesa} < V < V_{depleted} \\ \dfrac{V + V_{bi} + \dfrac{q\sigma_{charge}}{\varepsilon_1\varepsilon_0}(t_{InP}/2 + t_{grading} + t_{undoped}) + V_{extra}}{x_d + t_{InP} + t_{grading} + t_{undoped}} & V_{depleted} < V < V_{br} \end{cases} \tag{5.4}$$

with

$$V_{extra} = \frac{qN_G t_{grading}}{\varepsilon_2\varepsilon_0}(t_{grading}/2 + t_{undoped}) + \frac{q\sigma_{InGaAs}}{\varepsilon_2\varepsilon_0} t_{undoped} + \frac{qN_D}{2\varepsilon_2\varepsilon_0} t_{undoped}^2. \tag{5.5}$$

The depletion depth t(V) at bias V is given by

$$t(V) = \sqrt{(x_d + t_{InP} + t_{grading})^2 + \left(\frac{V - V'_{mesa}}{(qN_D)/(2\varepsilon_2\varepsilon_0)}\right)} - (x_d + t_{InP} + t_{grading}). \tag{5.6}$$

The photogain M(V) at bias V can be derived from the more general formula eqn. (2.8), when the electric field in the multiplication layer is constant, and it is given by

$$M(V) = \frac{1 - (\alpha_1(F_{InP})/\beta_1(F_{InP}))}{\exp[x_d \cdot (\alpha_1(F_{InP}) - \beta_1(F_{InP}))] - (\alpha_1(F_{InP})/\beta_1(F_{InP}))}, \tag{5.7}$$

where x_d and σ_{charge} are extracted with V_{mesa} and V_B, and V_B is extracted by fitting the experimental M-V characteristics to the Miller empirical formula as just discussed. V_B is better than V_{br} in reproducing the experimental M-V characteristics.

5.3.2 Results and discussions

To compare the physical model predictions to experiments, all 14 APDs discussed above are investigated again. A typical good and a typical fair match between the theoretical and experimental M-V characteristics are shown in Figure 5.6(a) and Figure 5.6(b), respectively, and even the agreement in the fair match is quite acceptable. There are about an equal number APDs with good and fair matches, as well as one APD which did not

give good agreement (APD5) as expected. It can be concluded that the physical model is successful, considering that many parameters are only estimated from the MOCVD growth conditions, rather than from direct measurements. The success indicates that both the physical model and the arguments in converting I_p-V into M-V are correct.

Similar to what has been found in the Miller empirical section, the physical model predicts that the normalized voltage V/V_{br} is lower for the APDs with lower values of V_{br} than for the APDs with higher values of V_{br} for achieving same photogain M. Recall that σ_{total} (which is proportional to the electric field discontinuity ΔF between the multiplication and absorption layers) is higher in the APDs with lower V_{br}, and the bias voltage is mainly dropped across the absorption layer. Then denoting the electric field in the multiplication layer F_M under the bias voltage V_M at photogain M, it can be shown that $V_M/V_{br} \approx (F_M - \Delta F)/(F_{br} - \Delta F) = 1 - (F_{br} - F_M)/(F_{br} - \Delta F)$. Therefore, V_M/V_{br} is smaller when ΔF is larger.

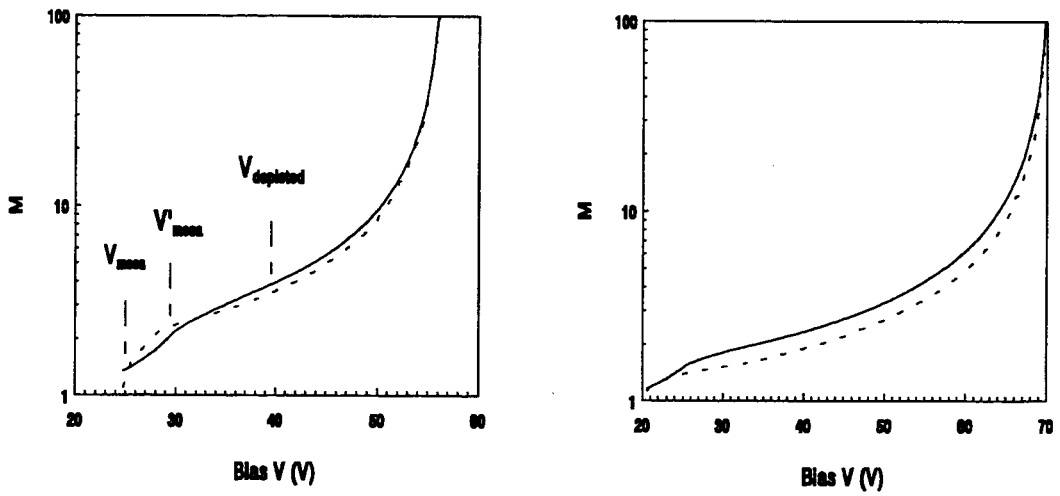

Figure 5.6 Physical modelling of M-V characteristics (solid lines). The dashed lines are experimental data. (a) Good match. (APD32) (b) Fair match. (APD34).

It is very interesting to note that the theoretical M is not unity at the bias voltage V_{mesa}, as has been discussed in the introduction. This non-unity phenomenon is more

severe for the APDs with lower V_{br}'s than for the APDs with higher V_{br}'s. For the examples in Figure 5.6, assuming unity gain at V_{mesa} would cause more than 50% error in M for the APD with lower V_{br}, and 10% for the APD with higher V_{br}. The electric field in the central multiplication layer has been built up before the bias voltage reaches V_{mesa}, and the multiplication gain is larger than unity, but it does not contribute to the photocurrent because there is not injection of carriers to the central active multiplication layer. This is why the Miller empirical formula is adequate to interpret p-n APDs as well as this type of complicated APDs, since it predicts non-zero multiplication gain as long as the bias voltage is non-zero.

The curvatures of the theoretical M-V characteristics when $V_{mesa} < V < V'_{mesa}$ is quite different than the curvatures when $V > V'_{mesa}$, and this is in general agreement to the experimental observations. This general agreement is due to the highly doped InGaAs layer, which modifies the slope of the electric field F_{InP} against the bias voltage as shown in Figure 5.7.

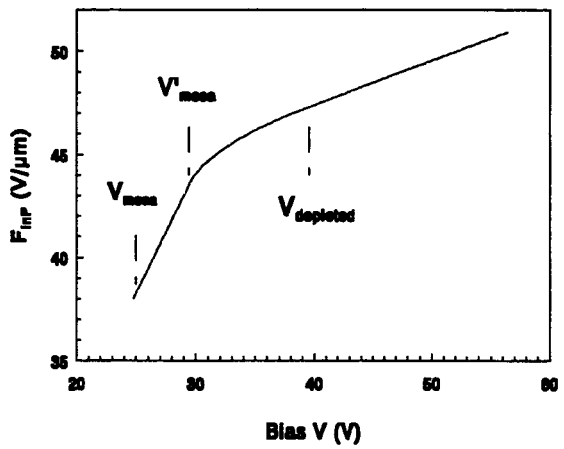

Figure 5.7 The electric field F_{InP} versus the bias voltage V for APD32.

Another interesting point confirmed is that the absorption layer is not completely depleted until at a bias voltage much higher than V_{mesa} is reached, as shown in Figure

5.6(a). This effect is particularly important for the APDs with lower V_{br}. It is obvious that a slow diffusion tail in the photoresponse will be observed at higher frequencies. However, this will not occur for the DC photogain described here. More importantly, this would not cause the normally observed variation of the quantum efficiency over a voltage bias range, as explained in the introduction. This phenomenon is confirmed by the good agreements between the theoretical and experimental M-V characteristics.

The agreements between the experimental data and the Miller empirical M-V characteristics are always good, while the agreements between the experimental data and the physical modelling are only good for half the APDs examined. This is not surprising since the empirical formula is also a good curve-fitting scheme. The discrepancy in bias voltage between the experiment and the physical model predictions for M=5 and 10 is 2.6 and 1.6 V respectively, and the discrepancy in M for $V=0.9V_{br}$ is 2 (M=7), which is caused by the steep slope there. Therefore, this physical model is adequate to physically model M-V characteristics except for the bias range close to breakdown, and totally adequate to model in logarithm scale as usually required.

5.3.3 Improved physical model

In the device parameter extraction discussed in last chapter, the device parameters, such as t_{InP}, $t_{grading}$, $t_{undoped}$, N_G, N_D and σ_{InGaAs}, can be adjusted within their respective experimental uncertainties. In addition, the physical model may be modified to include the effects of the ionizations in the charge and absorption layers. However, any modifications in the above device parameters, or any modification of the physical model, will cause corresponding changes in the extracted values of x_d and σ_{charge}.

If similar modifications are made in the physical modeling of M-V characteristics, then x_d and σ_{charge} will have to be re-extracted. As a matter of fact, the theoretical M-V

characteristics calculated using extracted x_d and σ_{charge} will ensure a perfect match of two unique points in M-V characteristics - V_{mesa} and V_{br}. It is clear that this physical model of M-V characteristics is not truly *ab initio* but is rather self-consistent.

The inclusion of the ionization in the absorption layer modifies M(V) of eqn. (5.7) into

$$M(V) = \frac{(1-\alpha_1/\beta_1)\left(\exp\left[\int_{F'_{heter}}^{F_{end}} (\beta_2(F') - \alpha_2(F'))\frac{dF'}{dF/dx}\right]\right)}{\exp[x_d(\alpha_1-\beta_1)] - \alpha_1/\beta_1 - (1-\alpha_1/\beta_1)\int_{F'_{heter}}^{F_{end}} \alpha_2(F)\exp\left(\int_{F'_{heter}}^{F} \beta_2(F') - \alpha_2(F')\frac{dF'}{dF/dx}\right)\frac{dF}{dF/dx}} \quad (5.8)$$

α_1 and β_1 are calculated with the electric field in the multiplication layer (eqn. (5.4)). It is easy to check that if the ionization in the absorption layer is ignored, the above equation becomes eqn. (5.7). The inclusion of this effect makes very little difference in the theoretical M-V characteristics. Since all the APDs examined have a V_{br} 70 V or lower, then as expected, ionization in the absorption layer contributes little to the photogain.

The inclusion of the ionization in the charge layer modifies M(V) of eqn. (5.7) into

$$M(V) = \frac{(1-\alpha_1/\beta_1)\left(\exp\left[\int_{F_{InP}}^{F_2} (\beta_1(F') - \alpha_1(F'))\frac{dF'}{dF/dx}\right]\right)}{\exp[x_d(\alpha_1-\beta_1)] - \alpha_1/\beta_1 - (1-\alpha_1/\beta_1)\int_{F_{InP}}^{F_2} \alpha_1(F)\exp\left[\int_{F_{InP}}^{F} (\beta_1(F') - \alpha_1(F'))\frac{dF'}{dF/dx}\right]\frac{dF}{dF/dx}} \quad (5.9)$$

Similarly, the inclusion of this effect makes very little difference in the theoretical M-V characteristics. The self-consistency is largely responsible for this negligible difference.

Perhaps a better example to demonstrate the self-consistency are the theoretical calculations with the other reported InP ionization rates, such as Umebu's [83] or Cook's [84].

This makes very little difference in the theoretical M-V characteristics as shown in Figure 5.8, even though it makes significant difference in the extracted device parameters. Independent and accurate measurements of x_d and σ_{charge} are the only way to decide which InP ionization rates are better.

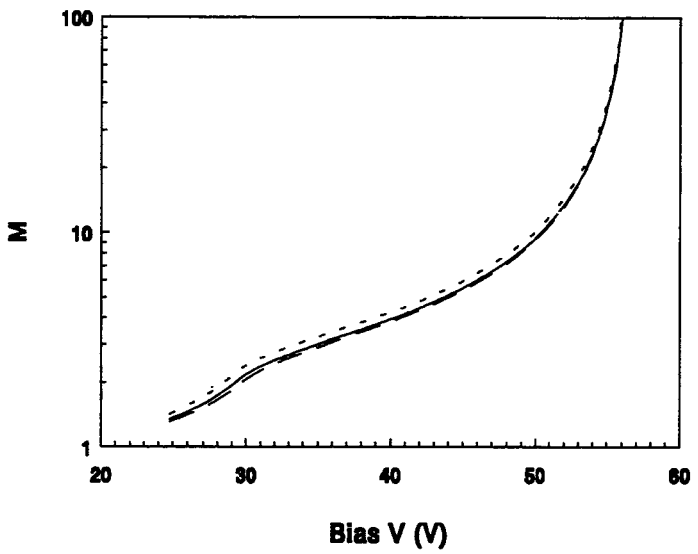

Figure 5.8 The theoretical M-V characteristics for APD32 calculated with Osaka's InP ionization rates (solid line), with Umebu's (dotted line), and with Cook's (dashed line).

Other device parameters used in calculating the theoretical M-V characteristics are also examined to seek any improvement within their respective uncertainties, and they are listed in Table 5.2. All the parameters make little difference to the theoretical M-V characteristics except the device parameter $t_{undoped}$. Clearly, $t_{undoped}$ is the only parameter which may improve the agreement between the theoretical and experimental M-V characteristics. For the particular wafers investigated here (wafer P623 and P624), $t_{undoped}$ is not directly measured. The default value of 3.8 μm is estimated from the argument that $t_{undoped}$ is equal to its value from calibration wafers with identical nominal MOCVD growth conditions. The uncertainty of $t_{undoped}$ (+/- 0.2 μm) refers to the variation among APDs

from the same wafer. It is found that it is always possible to find one particular value between 3.6 to 2.9 μm for each of the APDs with which the agreement the theoretical and experimental M-V characteristics is best, as shown in Figure 5.9. A best value of $t_{undoped}$ is determined by minimizing the sum of the square of the differences between the experimental and the theoretical M-V characteristics at all measured bias voltage points 5 V higher than V_{mesa} and 2 V lower than V_{br}. Certainly, for each individual APD, a range of values for $t_{undoped}$ can be found to obtain a reasonable agreement, which is much better than the typical good fit as shown in Figure 5.6(a). This range is typically ±0.3 μm.

Table 5.2 The effects to the theoretical M-V characteristics due to the uncertainties of some device parameters. The thickness is in μm, the doping concentration is in 10^{15} cm^{-3}, and the integrated areal charge density is in 10^{12} cm^{-2}.

Contributor	V_{mesa}	t_{InP}	$t_{grading}$	N_G	σ_{InGaA}	N_D	$t_{undoped}$	$t_{undoped}$
Default		0.17	0.09	10	0.4	0.7	3.8	3.8
Uncertainty	±1	±0.009	±0.005	±2.5	±0.05	±0.07	+0.2	-0.2
M-V	Little effect						Worse	Better

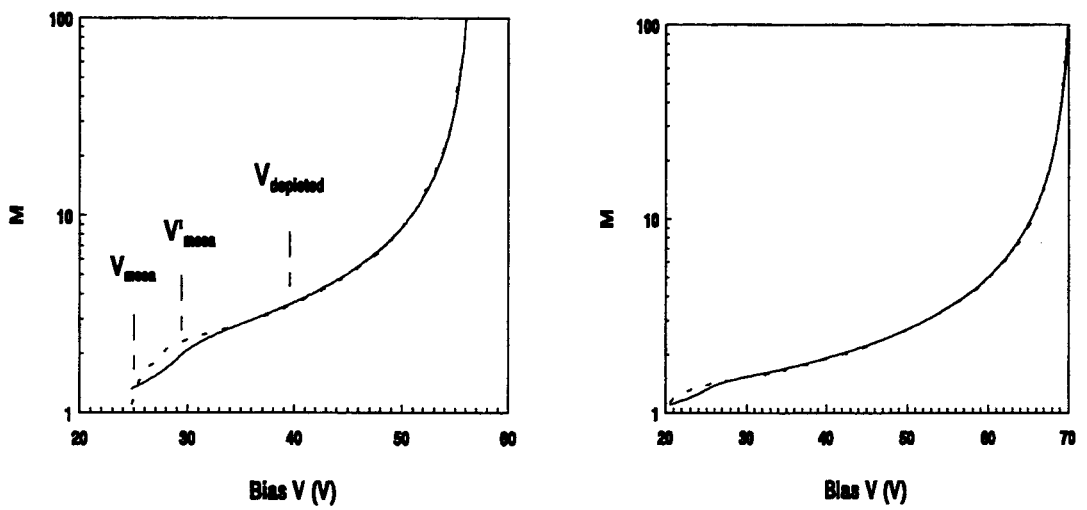

Figure 5.9 A typical almost perfect matched M-V characteristics. The solid and dashed lines are the theoretical and experimental M-V characteristics, respectively. (a) APD32 with $t_{undoped}$ = 3.4μm, and (b) APD34 with $t_{undoped}$ = 2.9μm.

This process offers an improvement over the previous described parameter extractions. Basically, by fitting the entire M-V characteristics (including V_{mesa} and V_{br}), three device parameters can be obtained simultaneously, i.e., x_d, σ_{charge}, and $t_{undoped}$. Measuring photocurrent I_p versus bias voltage V at room temperature should be mandatory for device characterization, modelling, and screening, since much information can be obtained from this simple measurement.

From a physical modelling point of view, the best compromised value of $t_{undoped}$ for all the APDs from wafer P623 is 3.2 μm. This new default value gives a better fit than the previous estimated value (3.8 μm). The new theoretical M-V characteristics are displayed in Figure 5.9. The shift in bias voltage (the worse case in the graph) for M=5 and 10 is 1.0 and 0.7 V, respectively, and the shift in M for $V=0.9V_{br}$ is 0.7 (M=7.1), which is caused by the steep slope there. Therefore, the physical model with this new default value is improved, and it is adequate to theoretically calculate the M-V characteristics in SAGCM InP/InGaAs APDs.

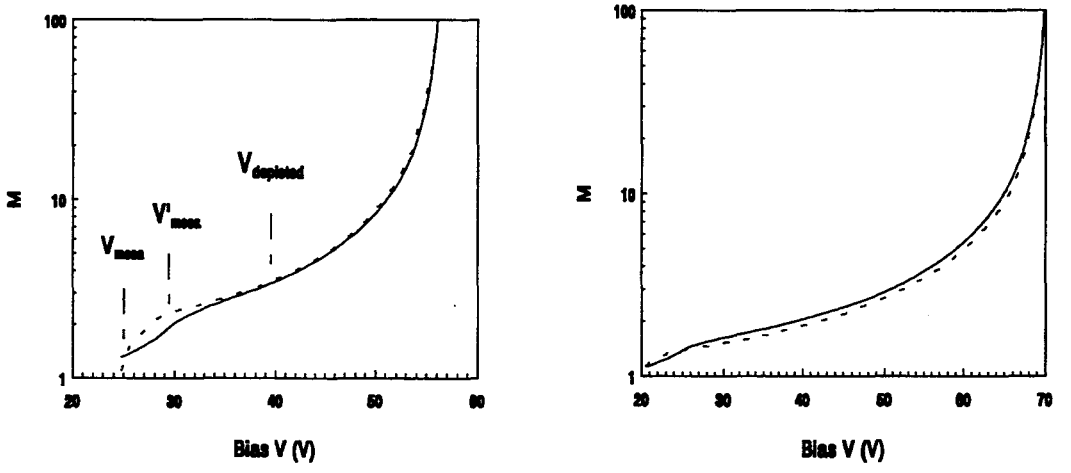

Figure 5.10 The theoretical M-V characteristics (solid lines) with new default value $t_{undoped} = 3.2\mu m$. The dashed lines are experimental data. (a) APD32. (b) APD34.

However, it should be cautioned that the curvatures of theoretical M-V characteristics also strongly depends on the slope of α_1 and β_1 with respect to 1/F in addition to the value of $t_{undoped}$. It will be demonstrated in the next chapter that the curvatures of the theoretical M-V characteristics are significantly different when it is calculated using α_1 and β_1 with different slopes. However, Osaka's ionization values are most trustworthy, and it is supported by four more experimental data (Umebu's [83], Cook's [84], Armiento's [85], and Taguchi [97][1]) as far as the slope is concerned. In other words, the selection of α_1 and β_1 is critical to both the absolute values of the extracted device parameters (x_d, σ_{charge}, and $t_{undoped}$) and the absolute correctness of the theoretical M-V characteristics. However, the consistency is much more important and this does not depend on the selection of α_1 and β_1.

5.4 Summary

In this chapter, I have demonstrated both experimentally and physically that for our planar SAGCM InP/InGaAs APDs that the photogain is unity when $V_{ann} < V < V_{mesa}$, and the quantum efficiency does not depend on the bias voltage. The Miller empirical formula for M-V characteristics is shown to be very appropriate to our APDs with r between 0.6 and 1.5, and an empirical relation between the power coefficient r in the Miller empirical formula and experimental V_{br} is derived. Finally, a physical model of the M-V characteristics is developed and proven to be successful in interpreting the experimental data from our APDs. It is also found that $t_{undoped}$ can be extracted from the experimental M-V characteristics – an improvement to the device parameter technique developed in the last chapter. The inclusion of the ionizations in the charge and absorption layers are not important in modelling the M-V characteristics.

---

1. At room temperature, $\alpha_1(F) = 920 \cdot \exp(-344/F)$, $\beta_1(F) = 430 \cdot \exp(-272/F)$.

Chapter 6 Temperature dependence of breakdown voltage and photogain

Temperature dependence of breakdown voltage is one of the critical performance parameters of APDs for coolerless applications. However, there has not been any theoretical modelling of temperature dependence of breakdown voltage in any types of InP-based APDs, even though a few early experimental works were published [96][18][70][101]. Maybe one of the reasons is that a large discrepancy can be found between the temperature dependence of α_1 and β_1 reported by different authors [95][96][97][98]. Therefore, it is important to examine this discrepancy for future modelling.

In this chapter, the temperature dependence of breakdown voltage V_{br} in SAGCM InP/InGaAs is investigated [101][101]. Detailed experimental results of the breakdown voltages for temperature from -40 °C to 110 °C of the SAGCM APDs having a range of device parameters, including a small sub-linearity at higher temperatures are reported. A physical model of temperature dependence of breakdown voltage, as well as numerical results are presented with a full account of all important device details. Then the model is tested on other types of InP-based APDs from the published literature. Finally, the temperature dependence of the M-V characteristics is discussed.

6.1 Theory

The device parameters extraction technique ensures a perfect match of V_{br} at room temperature since x_d and σ_{charge} are extracted using V_{br} at room temperature. V_{br} at any temperature can be calculated from eqn. (4.2) once σ_{charge} and x_d are determined, and F_{br}, calculated from eqn. (4.3), is the only variable which is a strong function of temperature for the temperature range investigated here. The temperature dependence of F_{br} is mainly due to the temperature dependence of α_1 and β_1, as can be seen from eqn. (4.3). The ion-

ization in the InGaAs absorption layer can be ignored for a first-order approximation, and this is discussed in detail later.

A generalized theory (Baraff theory) for the impact ionization process in semiconductor has been developed [91] in terms of the threshold energy E_i, the average energy loss per phonon scattered E_r, and the carrier mean free path λ from optical-phonon scattering. Unfortunately, this formula is not very convenient for modelling since it can only be numerically calculated. Later, an analytic expression (Okuto-Crowell theory) applicable for a wide range of electric fields was given in [92] and it is

$$\alpha, \beta = \frac{qF}{E_i} \exp\left\{ 0.217 \left(\frac{E_i}{E_r}\right)^{1.14} - \sqrt{\left[0.217\left(\frac{E_i}{E_r}\right)^{1.14}\right]^2 + \left[\frac{E_i}{qF\lambda}\right]^2} \right\}, \tag{6.1}$$

where F is the electric field. Assuming that the energy loss per unit path length is independent of temperature, then the temperature dependence of E_r and λ were obtained [93] as

$$E_r = E_{ro} \tanh\left(E_{ro}/2kT\right), \qquad \lambda = \lambda_o \tanh\left(E_{ro}/2kT\right), \tag{6.2}$$

and E_{ro} and λ_o are the values of E_r and λ at 0 K. Furthermore, the temperature dependence of E_i can be assumed to be the same as the temperature dependence of the bandgap energy $E_g(T)$ (eV), and for InP [94] it is given by

$$E_g(T) = 1.421 - \frac{3.63 \cdot 10^{-4} T^2}{(T + 162)}, \tag{6.3}$$

where T is in degrees Kelvin (K).

In principle, α_1 and β_1 can be completely determined once E_i, E_r, and λ at one particular temperature (room temperature) are known. In general, some or all of the parameters in the Okuto-Crowell theory are adjusted to fit experimentally measured α_1 and β_1 at room temperature. However, a large discrepancy can be found between E_i, E_r, and λ reported by different authors [95][96][97][98] (Table 6.1). Different parameters used for

fitting and the discrepancy between experimentally determined α_1 and β_1 are the main reasons for this large discrepancy. Note that, to the author's best knowledge, Ref. [97] is the only work where the temperature dependence of α_1 and β_1 is experimentally determined, and its α_1 and β_1 at room temperature are close to Osaka's values [32] for electric fields from 50 to 60 V/μm.

Table 6.1 E_i, E_r and λ at 300K for InP from references. E_{ro} and λ_o are calculated from eqn. (6.2) except in Ref. [97], where they were determined by fitting experimental α_1 and β_1 at a few temperatures.

	E_i(eV)	E_r(meV)	λ(Å)	E_{ro}(meV)	λ_o(Å)	Fitted parameter	Ref.	Source of measured data
α_1	1.99	13	18.0	27	37.6	λ	[95]	[95]
β_1	1.65	26	30.1	40	46.4			
α_1	1.57	33.7	27.0	46.9	37.5	λ	[96]	Umebu's[83]
β_1	1.61	42.9	33.1	54.7	42.2			
α_1	1.84	32.7	29.6	46	41.7	E_{ro}, λ_o	[97]	[97]
β_1	1.65	21.6	24.8	36	41.3			
α_1	2.37	39.9	45.2	52.2	59.1	E_i, E_r, λ	[98]	Cook's[84]
β_1	2.00	39.9	45.2	52.2	59.1			

6.2 Experimental results

The temperature dependence of our APDs was measured by placing devices in a variable temperature oven (-80 to 200 °C). The temperature uncertainty of the devices is ~ 1 °C. The dark current versus (reverse) bias voltage was measured with an HP 4145B Semiconductor Parameter Analyzer (SPA), and the accuracy of measuring DC currents is ~ 1 pA.

Typical (APD32) dark currents versus bias voltages at different temperatures are shown in Figure 6.1. The breakdown is impact ionization breakdown since it shows a hard

breakdown rather than a soft breakdown, as in the case of Zener tunneling breakdown [70]. The experimental V_{br} is defined as the voltage corresponding to 10 μA through the APD. Experimental V_{br} as a function of temperature from -40 °C to 110 °C are shown as symbols in Figure 6.2 for three APDs (APD14, APD32 and APD34) with different room temperature V_{br} from the same wafer (P623).

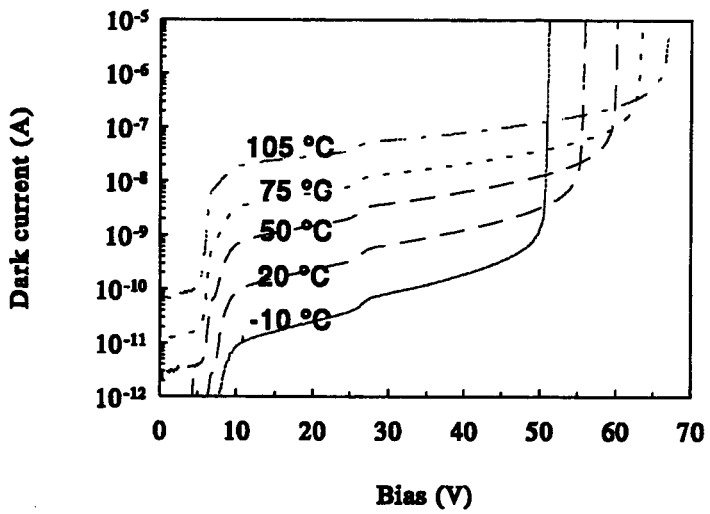

Figure 6.1 Typical (APD32) dark currents versus bias voltages for different temperatures. The breakdown voltage is defined as the voltage at which the dark current is 10 μA.

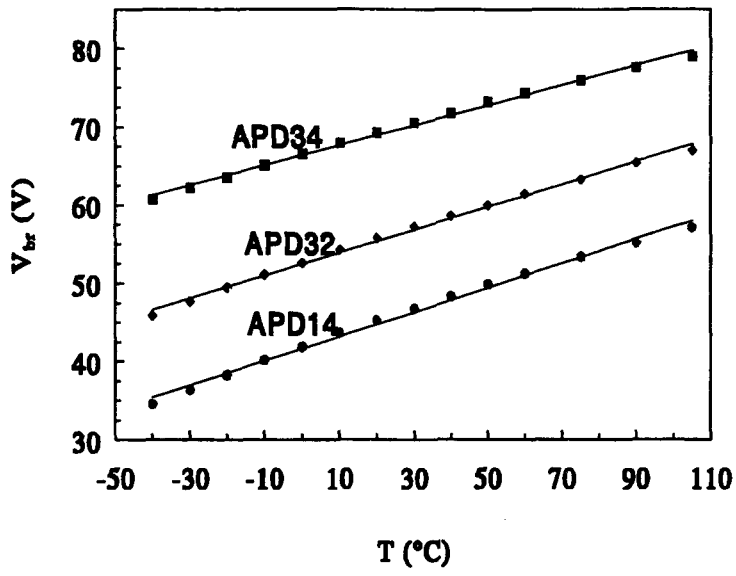

Figure 6.2 The V_{br} as function of temperature from -40 °C to 110 °C for three APDs. The symbols are experimental data, and the solid lines are linear fits.

Experimental V_{br} at temperature T can be approximated as a linear function of T

$$V_{br}(T) = V_{br}(0) + \eta_{exp} \cdot T, \tag{6.4}$$

where $V_{br}(0)$ is V_{br} at 0 °C, T is in °C, and η_{exp} is the experimental temperature coefficient of $V_{br}(T)$. For a first order approximation, the experimental $V_{br}(T)$ is well represented by eqn. (6.4). However, a close examination reveals that η_{exp} is different at lower and higher temperatures for each APD. By linearly fitting the experimental data for all temperatures (-40 to 105 °C, AVE), for lower temperatures (-40 to 0 °C, LT), and for higher temperatures (50 to 105 °C, HT), respectively, different η_{exp} have been found and they are listed in Table 6.2. In addition, there is a small variation of η_{exp}(AVE) among the APDs ranged from 0.16 to 0.13 V/°C. To confirm the existence of these second order variations, photocurrents versus bias voltages were also measured for different temperatures for each APD, and the experimental $V_{br}(T)$ is extracted from this measurement. A similar trend can be confirmed from these experimental $V_{br}(T)$. A very generous estimation of

measurement error in η_{exp} is ±0.05 V/°C.

Table 6.2 The linearly fitted η_{exp} and $V_{br}(0)$ for the APDs, for all the temperatures (AVE), for between -40 to 0 °C (LT), and for between 50 to 105 °C (HT). η_{exp} is in the unit of V/°C and $V_{br}(0)$ in V.

	η_{exp}(AVE)	η_{exp}(LT)	η_{exp}(HT)	$V_{br}(0)$(AVE)	$V_{br}(0)$(LT)	$V_{br}(0)$(HT)
APD14	0.156	0.184	0.131	41.7	42.0	43.5
APD32	0.146	0.170	0.128	52.5	52.8	53.7
APD34	0.128	0.146	0.105	66.4	66.6	68.0

6.3 Discussion

The extracted x_d and σ_{charge} for the three APDs (with Taguchi's [97] α_1 and β_1 at 20 °C) are listed in Table 6.3. The extractions are performed with the parameter extraction standard technique, using V_{mesa}, which hardly change with temperature, and V_{br} at 20 °C. The extracted x_d does not change significantly among the APDs with different V_{br}, whereas the extracted σ_{charge} for the APDs with large V_{br} is noticeably smaller than for the APDs with smaller V_{br}. This extraction procedure is repeated whenever a different set of α_1 and β_1 is used for calculating $V_{br}(T)$. Note that 3.2 μm rather than 3.8 μm is used as the value of $t_{undoped}$ to be consistent with the results presented in chapter 5.

Table 6.3 The input parameters and the extracted device parameters for the SAGCM APDs.

	V_{mesa}(V)	V_{br}(20°C) (V)	x_d(μm)	σ_{charge}(cm^{-2})	F_{br}(V/μm)	F'_{heter}(V/μm)
APD14	25.8	44.8	0.562	2.72×10^{12}	51.6	4.8
APD32	24.8	55.4	0.590	2.50×10^{12}	51.2	7.6
APD34	20.6	69.0	0.544	2.23×10^{12}	51.9	12.2

The theoretical $V_{br}(T)$ for the three APDs calculated with each set of α_1 and β_1 in Table 6.1 are displayed in Figure 6.3(a-d), respectively. These figures show that it does not

matter which α_1 and β_1 is used; that is, despite which set of parameters is used in the Okuto-Crowell theory, the theoretical $V_{br}(T)$ is very close to a linear function of T,

$$V_{br}(T) = V_{br}(0) + \eta_{the} \cdot T, \tag{6.5}$$

and the theoretical temperature coefficient η_{the}, calculated with a particular set of α_1 and β_1, does not change from one APD to another. For example, the linearly fitted η_{the} is $0.154 \pm 0.001 V/°C$, calculated with α_1 and β_1 from [97] and $0.105 \pm 0.001 V/°C$ from [98].

The theoretical $V_{br}(T)$, which agree best with the experimental data for all the APDs, are the ones calculated with α_1 and β_1 from Taguchi's [97], as shown in Figure 6.3(c). Because of this good agreement, and the fact that they are the only experimentally determined α_1 and β_1 at a few different temperatures, this set of α_1 and β_1 (or this set of parameters in the Okuto-Crowell theory) is considered most reliable, at least as far as the temperature dependence is concerned, and this set will be used in the rest of this thesis.

A typical (APD32) calculated $F_{br}(T)$ from eqn. (4.3), eqn. (6.1) and eqn. (6.2) is shown in Figure 6.4. It can be proved generally that $F_{br}(T)$ is a linear function of temperature T, which is not easy to see from the equations. Since F_{br} depends only weakly on x_d, its temperature coefficient $\partial F_{br}/\partial T$ does not vary much among the APDs investigated here, and it is approximately $3.84 \cdot 10^{-2} (V/(\mu m \cdot °C))$. Therefore, η_{the} can be related to the temperature coefficient of F_{br} from eqn. (4.2) analytically, and it is given by

$$\eta_{the} = \frac{\partial V_{br}}{\partial T} = \frac{\partial F_{br}}{\partial T}(x_d + t_{InP} + t_{grading} + t_{undoped}) = \frac{\partial F_{br}}{\partial T} \cdot 4.0\mu m. \tag{6.6}$$

The numerical value is obtained if it is assumed that $x_d \approx 0.54\mu m$. The variation of x_d among the APDs is too small to significantly change this numerical value. Thus, it can be analytically calculated that $\eta_{the} = 0.154 V/°C$, which is identical to what has been numerically calculated.

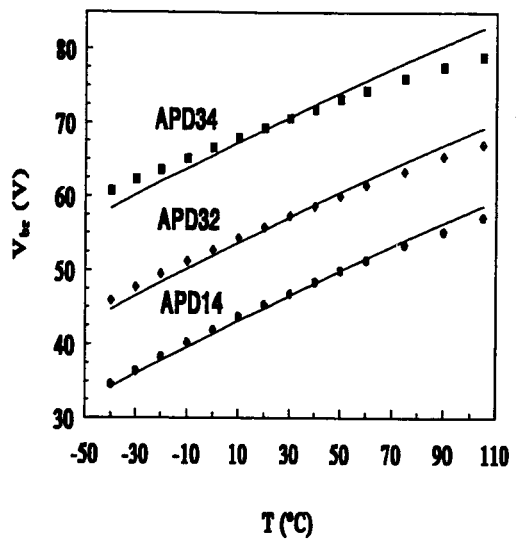

(a)

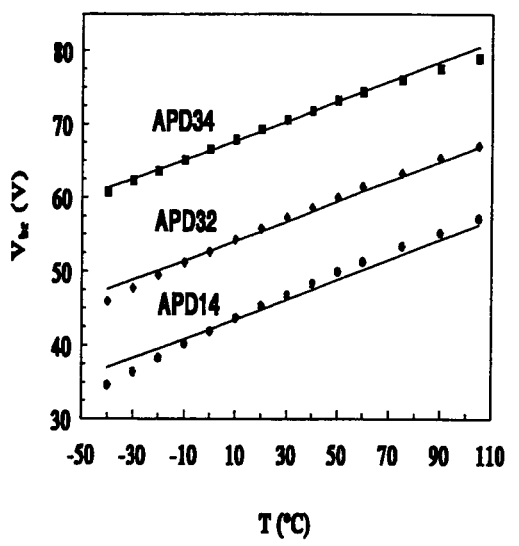

(b)

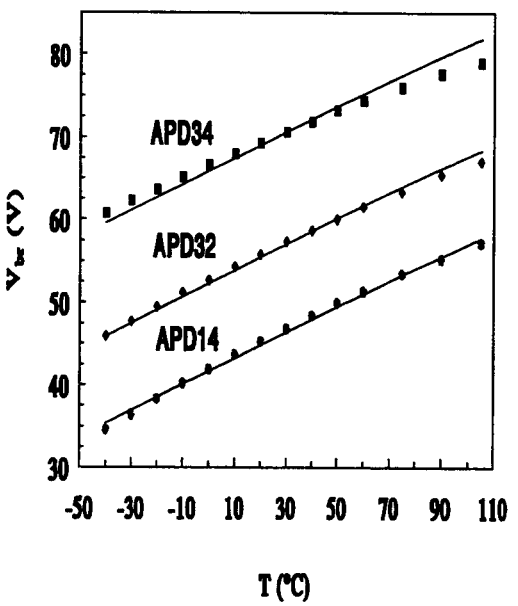

(c)

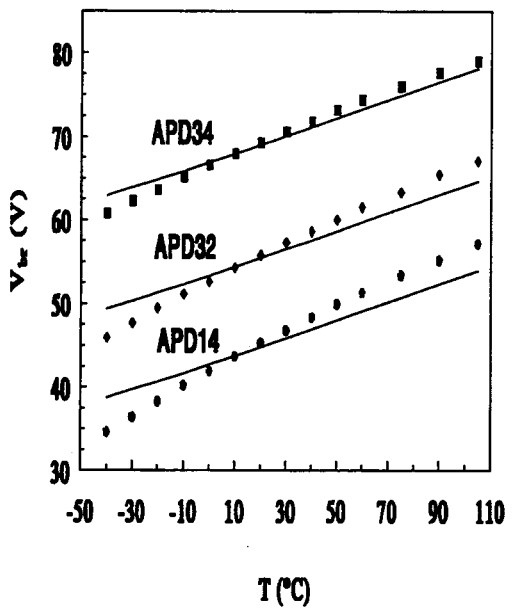

(d)

Figure 6.3 The theoretical $V_{br}(T)$ (solid lines) calculated with α_1 and β_1 from Refs. (a) [95], (b) [96], (c) [97], and (d) [98]. The symbols are experimental data.

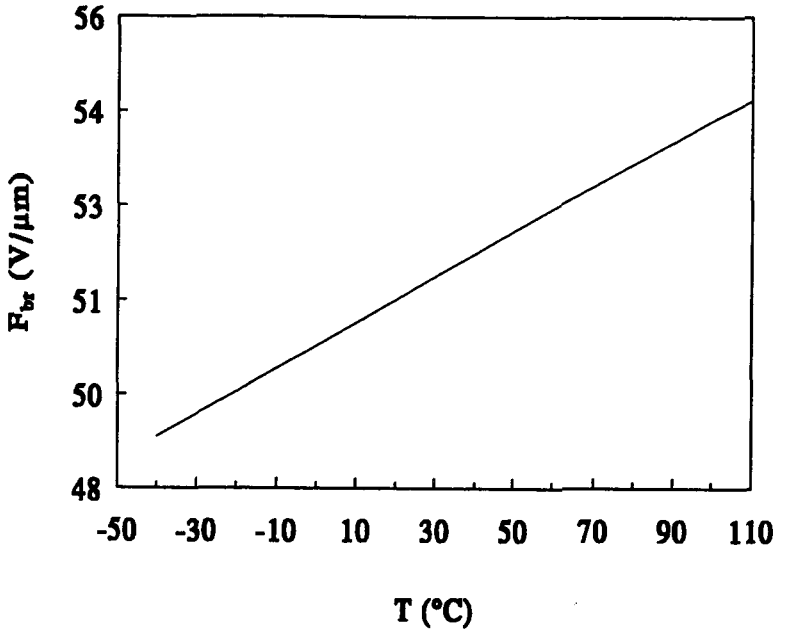

Figure 6.4 The theoretical $F_{br}(T)$ for APD32 calculated with α_1 and β_1 from Taguchi's.

This analytical expression offers some physical insights which are not obvious from the numerical calculations. For example, it is now easy to explain the small but discernible variation of η_{exp} among the APDs (Table 6.2) which cannot be accounted for, regardless of the choice for the parameters in Okuto-Crowell theory. From eqn. (6.6), it is clear that only a variation of $t_{undoped}$ is possible to cause this small variation of η_{exp} since the variations of the other thicknesses there are too small. For example, if $t_{undoped} = 3.8\mu m$, then the theoretical value of $\partial V_{br}/\partial T$ becomes approximately $0.177V/°C$.

At higher temperatures, the theoretical and experimental $V_{br}(T)$ has a visible discrepancy for all the APDs, but particularly for APD34 (Figure 6.3(c)). The neglect of ionization in the InGaAs absorption layer may be the possible reason. F'_{heter} at room temperature for APD34 is much larger than for other APDs (Table 6.3), and it is expected that the contribution from the ionization in the InGaAs absorption layer is largest for APD34.

The only reported parameters for the Okuto-Crowell theory for ionization in InGaAs from the literature [98] is listed in Table 6.4, and this was fitted to Pearsall's experimental data at room temperature [82]. The bandgap energy (E_g) for InGaAs is given by [94]

$$E_g(T) = 0.822 - \frac{4.5 \cdot 10^{-4} T^2}{T + 327}, \tag{6.7}$$

where T is in degrees Kelvin. It must be emphasized that there are no reports about the temperature dependence of α_2 and β_2, and the parameters for Okuto-Crowell theory from Ref. [98] were obtained by fitting at room temperature only.

Table 6.4 E_i, E_r and λ at 300K for InGaAs. E_{ro} and λ_o are calculated from eqn. (6.2).

	E_i(eV)	E_r(meV)	λ(Å)	E_{ro}(eV)	λ_o(Å)	Fitted parameter	Ref.	Source of measured data
α_2	1.05	25.1	44.7	39.24	69.9	E_i, E_r, λ	[98]	[82]
β_2	1.26	25.1	44.7	39.24	69.9			

The re-calculated $V_{br}(T)$ is shown in Figure 6.5 for APD34. The theoretical $V_{br}(T)$ including InGaAs ionization makes a small but not sufficient improvement with respect to the theoretical $V_{br}(T)$ without including InGaAs ionization. This failure is due to the fact that α_2 and β_2 decreases comparatively as fast as α_1 and β_1 do with increasing temperature, and the ratio between the contribution to ionization from the InGaAs absorption layer and the InP multiplication layer remains comparable at all temperatures. Should the ionization in the InGaAs layer be responsible for the discrepancy at higher temperatures, then α_2 and β_2 would not decrease as much as α_1 and β_1 do when the temperature increases. There are no independent measurements to support this claim at present time.

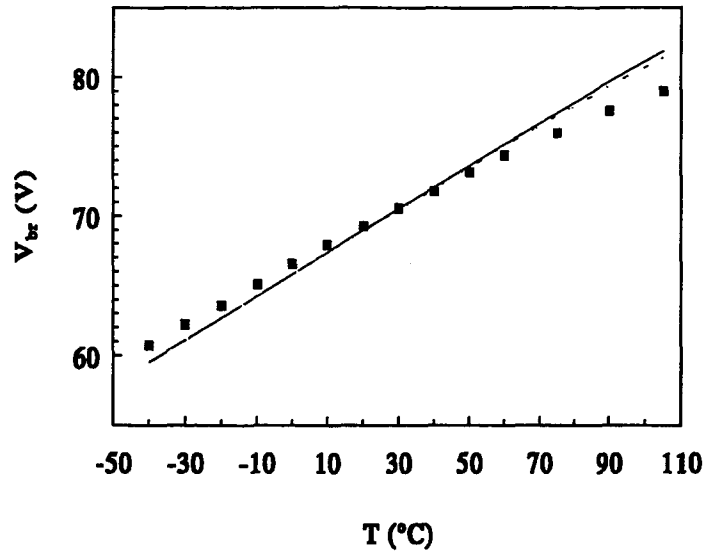

Figure 6.5 The theoretical V_{br} (T) with (solid line) or without (dashed line) the ionization in the InGaAs absorption layer for APD34.

6.4 InP-based APDs

It is important that the theoretical modelling of $V_{br}(T)$ developed here be applicable to other InP-based APDs. Two p^+-n InP APDs listed in Table 6.5 (Samples A and B) in the literature are discussed, and their experimental values are taken from the graphs/values in [18][96].

Table 6.5 The experimental and theoretical parameters related to $V_{br}(T)$ for two p^+-n InP diodes in the literature. The unit for N_{InP} is $10^{16}cm^{-3}$, t_{InP} is μm, V_{br} is V, η is V/°C, F_{br} is V/μm, and $\partial F_{br}/\partial T$ is V/μm°C.

	Experimental				Theoretical				
Sample	N_{InP}	t_{InP}	$V_{br}(0°C)$	η_{exp}	$V_{br}(0°C)$	η_{the}	$F_{br}(0°C)$	$\partial F_{br}/\partial T$	Ref.
A	0.9	3	80	0.15	102.2	0.146	52.25	0.0361	[18]
B	4	3	36	0.05	33.9	0.043	64.09	0.0390	[96]

The experimental $V_{br}(T)$ indicates that V_{br} is a linear function of T, and η_{exp} can be significantly different from one APD to another. N_{InP} and t_{InP} are the respective doping

concentration and thickness of the n-region in a p^+-n InP diode. For a reach-through structure like Sample A (n-region is completely depleted at breakdown), the relevant formulas are given by

$$\begin{aligned} V_{br}(T) &= t_{InP}\left(F_{br}(T) - \frac{qN_{InP}}{\varepsilon_0\varepsilon_1}t_{InP}\right) - V_{bi}, \\ \eta_{the} &= t_{InP}\frac{\partial F_{br}}{\partial T}, \\ \zeta = \eta_{the}/(V_{br}(0°C)) &= \frac{\partial F_{br}/\partial T}{F_{br} - \frac{qN_{InP}}{2\varepsilon_0\varepsilon_1}t_{InP}}. \end{aligned} \tag{6.8}$$

ζ is the relative temperature coefficient of $V_{br}(T)$. For a long p^+-n diode like Sample B (n-region is not completely depleted at breakdown), the relevant formulas are given by

$$\begin{aligned} V_{br}(T) &= \frac{qN_{InP}}{2\varepsilon_0\varepsilon_1}F_{br}^2(T) - V_{bi}, \\ \eta_{the} &= F_{br}\frac{qN_{InP}}{\varepsilon_0\varepsilon_1}\frac{\partial F_{br}}{\partial T}, \\ \zeta = \eta_{the}/(V_{br}(0°C)) &= 2\frac{\partial F_{br}/\partial T}{F_{br}}. \end{aligned} \tag{6.9}$$

V_{bi} has been ignored for the last expression (ζ) in each of the last two equations. The breakdown condition is very similar to eqn. (4.17), and it is given by,

$$1 - \int_{F_{br}}^{F_{end}} \alpha_1(F,T)\exp\left[\int_{F_{br}}^{F}(\beta_1(F',T) - \alpha_1(F',T))\frac{dF'}{dF/dx}\right]\frac{dF}{dF/dx} = 0. \tag{6.10}$$

F_{end} is the electric field at $x=t_{InP}$, and it is zero in the case of a long p^+-n diode.

$F_{br}(T)$ is found numerically to be a linear function of temperature (Figure 6.6), and its value depends on N_{InP} only. This can be readily understood from eqn. (6.10) that the most important contribution to ionization is from the narrow region with highest electric field. Therefore, it is clear from the analytical expressions in eqn. (6.8) or eqn. (6.9) that for a first order approximation, η_{the} is indeed independent of temperature. From Figure 6.6 and

Table 6.5, it is clear that the theoretical modelling is very satisfactory, even without considering the fact that the input parameters (N_{InP} and t_{InP}) are subject to some uncertainties. It also indicates that the valid range of electric field for the temperature dependence of α_1 and β_1 is from 50 to 65 V/μm at room temperature, and there are no reasons why the valid range of electric field cannot be extended even further.

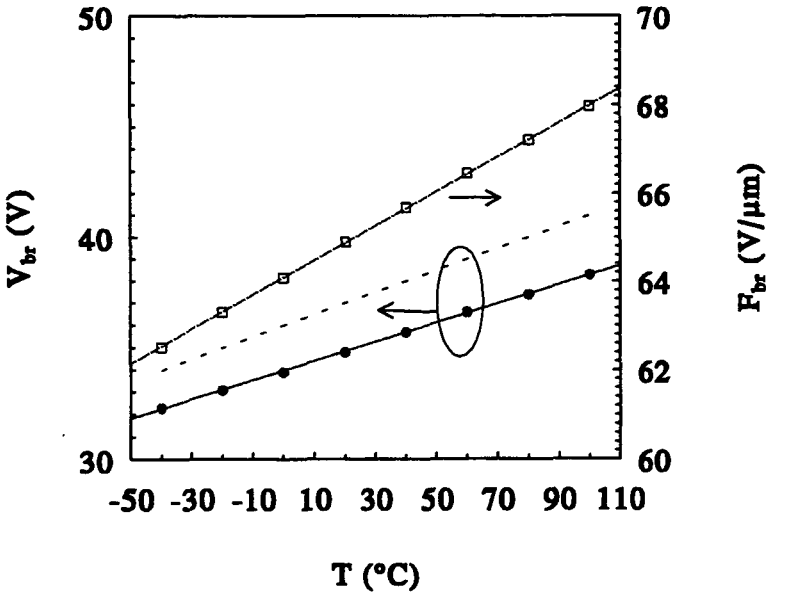

Figure 6.6 The theoretical $V_{br}(T)$ and $F_{br}(T)$ (solid lines) for p^+-n InP diode sample B. The dotted line is the experimental data.

The model is also applied to three SAM InP/InGaAs APDs in the literature [18][70] listed in Table 6.6, where N_{InP} and t_{InP} are the respective doping concentration and the thickness of the multiplication layer, and N_{InGaAs} and t_{InGaAs} are the respective doping concentration and the thickness of the absorption layer. Since the InGaAs layer is not completely depleted at breakdown, then the relevant formulas can be given by

$$V_{br}(T) = t_{InP}\left(F_{br}(T) - \frac{qN_{InP}t_{InP}}{2\varepsilon_0\varepsilon_1}\right) + \frac{\left(F_{br}(T) - \frac{qN_{InP}t_{InP}}{\varepsilon_0\varepsilon_1}\right)^2}{2qN_{InGaAs}/(\varepsilon_0\varepsilon_2)} - V_{bi}, \tag{6.11}$$

$$\eta_{the} = \frac{\partial F_{br}}{\partial T}\left[t_{InP}\left(1 - \frac{\varepsilon_2 N_{InP}}{\varepsilon_1 N_{InGaAs}}\right) + \frac{F_{br}}{qN_{InGaAs}/(\varepsilon_0\varepsilon_2)}\right].$$

The breakdown condition is unchanged from the case of a p^+-n diode as discussed above. Not surprisingly, the theoretical calculations agree well with the experimental data as listed in Table 6.6.

Table 6.6 The experimental and theoretical parameters related to $V_{br}(T)$ for the three SAM InP/InGaAs diodes in the literature. The unit for N_{InP} and N_{InGaAs} is $10^{16}cm^{-3}$, t_{InP} is μm, V_{br} is V, η is V/°C, F_{br} is V/μm, and $\partial F_{br}/\partial T$ is V/μm°C. t_{InGaAs} is not listed since it is irrelevant.

Sam-ple	Experimental					Theoretical				Ref.
	N_{InP}	t_{InP}	N_{InGaAs}	$V_{br}(0°C)$	η_{exp}	$V_{br}(0°C)$	η_{the}	$F_{br}(0°C)$	$\partial F_{br}/\partial T$	
A	1	3	0.67	77	0.15	95.9	0.147	52.93	0.0366	[70]
B	0.8	3.2	1	100	0.18	110.6	0.153	51.51	0.0359	[18]
C	0.9	2	1	80	0.15	102.2	0.146	52.25	0.0361	[18]

Another widely used expression to describe the experimental $V_{br}(T)$ in InP-based APDs [96][18][70] is given by

$$V_{br}(T) = V_{br}(0°C)\,[1+\zeta T], \tag{6.12}$$

where T is in °C, and ζ is the relative temperature coefficient of V_{br}. This expression is mathematically equivalent to the expression of $V_{br}(T)$ with temperature coefficient η used so far. However, physically the expression of eqn. (6.12) implicitly states that ζ depends strongly on the properties of semiconductor, but weakly on the specific details of devices, which has been proven to be correct both experimentally and theoretically for Si p^+-n APDs [101]. However, this cannot be generalized to other structures. For example, the experimental values of ζ as listed in Figure 6.7 are very close among the SAM APDs, but change by more than 100% among the SAGCM APDs.

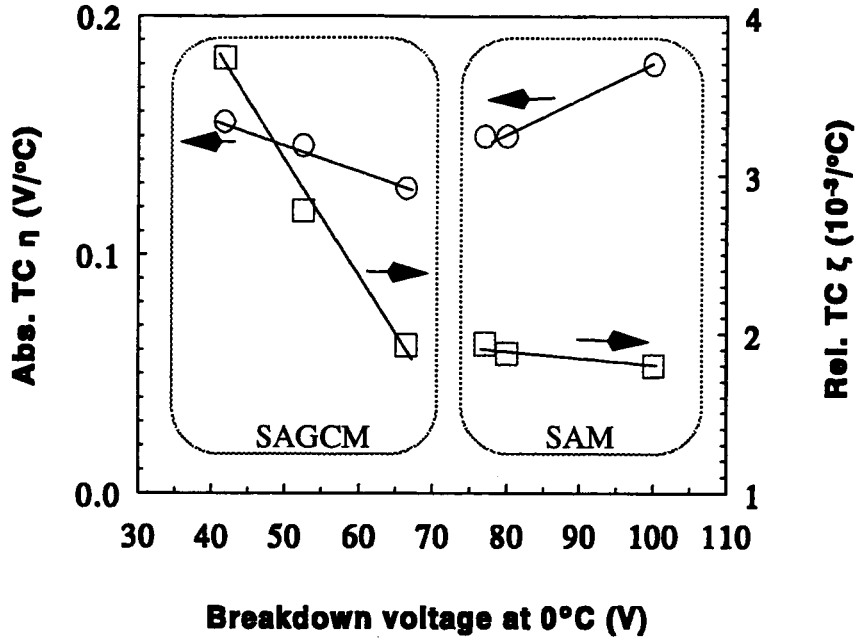

	p⁺-n		SAM			SAGCM		
	A	B	A	B	C	APD14	APD32	APD34
V_{br}(0°C) (V)	80	36	77	100	80	41.7	52.5	66.4
η (V/°C)	0.15	0.05	0.15	0.18	0.15	0.156	0.146	0.128
ζ(10^{-3} °C^{-1})	1.9	1.4	1.94	1.8	1.88	3.74	2.78	1.93

Figure 6.7 Summarized experimental results for all the InP- based APDs. They are also tabulated.

It can be demonstrated that the insensitivity of ζ to device details for Si p⁺-n APDs is also true for long InP p⁺-n APDs. The numerical results for different N_{InP} calculated from eqn. (6.9) and eqn. (6.10) are displayed in Figure 6.8. These results show that $\partial F_{br}/\partial T$ is not a strong function of N_{InP}; therefore, neither is ζ. However, since V_{br} at 0°C is a strong function of N_{InP}, then η will also be a strong function of N_{InP}. Note that the p⁺-n sample A

is a reach-through diode rather than a long diode; thus, it does not agree with the values calculated for long InP p^+-n APDs.

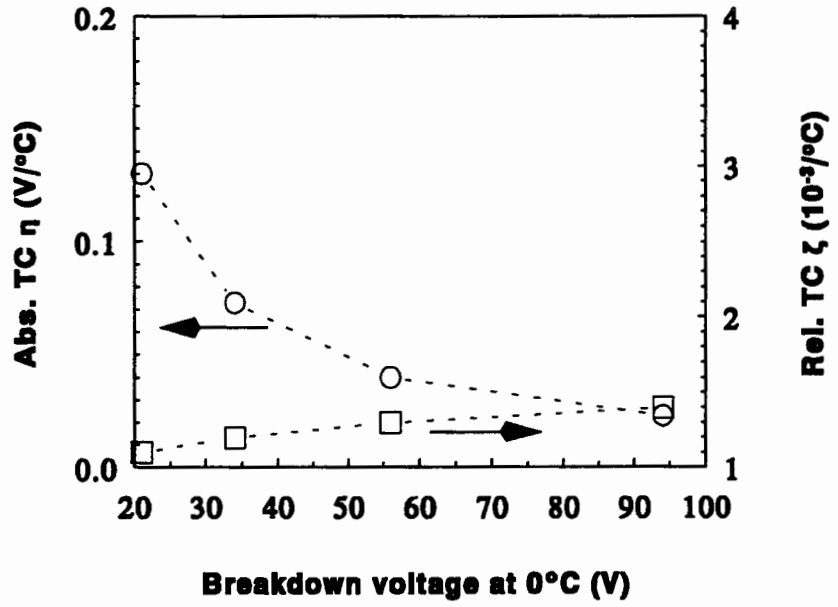

$N_{InP}(10^{16}\ cm^{-3})$	$V_{br}(0°C)(V)$	$F_{br}(0°C)(V/\mu m)$	$\partial F_{br}/\partial T$ (V/μm°C)	η(V/°C)	$\zeta(10^{-3}\ °C^{-1})$
1	94	52.93	0.037	0.13	1.4
2	56	57.95	0.0385	0.073	1.3
4	34	64.09	0.040	0.040	1.2
8	21	71.74	0.041	0.023	1.1

Figure 6.8 Theoretical results for long InP p^+-n APDs with different N_{InP}. They are also tabulated.

As stated above, this phenomenon that ζ is insensitive to device details of long InP p^+-n APDs cannot be generalized, and the agreement of the values of ζ between the SAM APDs in Figure 6.7 is coincidental rather than generally correct, since their structures and doping concentrations are similar. For example, if N_{InP} keeps increasing, then SAM APDs become p^+-n APDs; therefore, the value of ζ will become 1.1 rather than 1.8. The

SAGCM InP/InGaAs APDs are the better examples to demonstrate this point. As can be seen from eqn. (6.6), η is independent from σ_{charge}, whereas V_{br} strongly depends on σ_{charge}. Therefore, this strong dependence causes the large variation of ζ among the SAGCM InP/InGaAs APDs, as has been experimentally observed.

6.5 Temperature dependence of photogain

It is relatively straightforward to extend the theoretical model of the M-V characteristics at room temperature to any temperatures, combining the model of photogain at room temperature and the model of temperature dependence of breakdown voltage.

Typical (APD32) experimental M-V characteristics for different temperatures are shown in Figure 6.9. Theoretical M-V characteristics for different temperatures can be calculated using eqn. (5.7) and eqn. (5.4) with Taguchi's α_1 and β_1, and the results are displayed in Figure 6.10(a). The unsatisfactory agreement between the theoretical and experimental M-V characteristics can be improved dramatically if $t_{undoped} = 3.8\mu m$ is used, as shown in Figure 6.10(b). It should be noted that in principle, the values of x_d and σ_{charge} used in the calculations of M-V characteristics should be extracted each time a different value of $t_{undoped}$ is used. However, it is found that this is not necessary as long as M versus V/V_{br} is calculated. In other words, the shape of the M-V characteristics is not sensitive to the values of x_d and σ_{charge}, whereas the values of V_{br} are.

It has been found that $t_{undoped} = 3.2\mu m$ is the better choice for modelling the M-V characteristics at room temperature as long as it is calculated with one of the InP ionization rates reported by Osaka's, Umebu's, Cook's, or Armiento's. Note that the slopes of the ionization rates with respect to 1/F are very similar among these reported InP ionization rates.

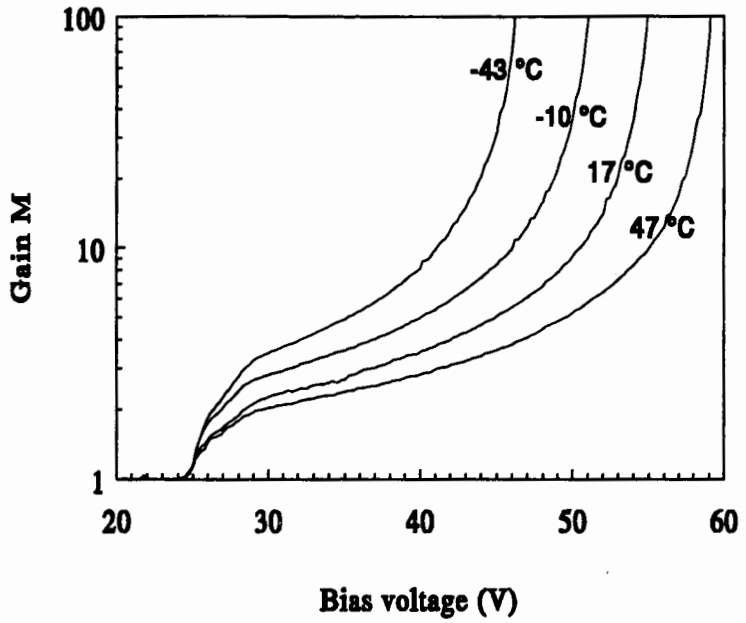

Figure 6.9 Typical (APD32) experimental photogains versus bias voltages for different temperatures.

For modelling the temperature dependence of the M-V characteristics, $t_{undoped} = 3.8\mu m$ is the better choice. The obvious contradiction is due to the significant difference in the slopes between Osaka's and Taguchi's InP ionization rates shown in Figure 6.11, and that are used in the calculations. The absolute values of the ionization rates are certainly very important for calculating V_{br}, but only the slope of the ionization rates with respect to 1/F is important for calculating the M-V characteristics, as already demonstrated in chapter 5.

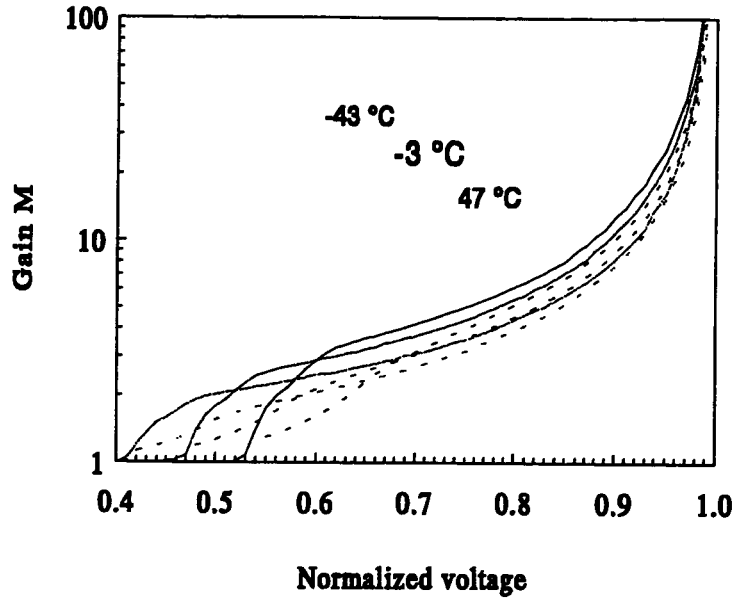

(a)

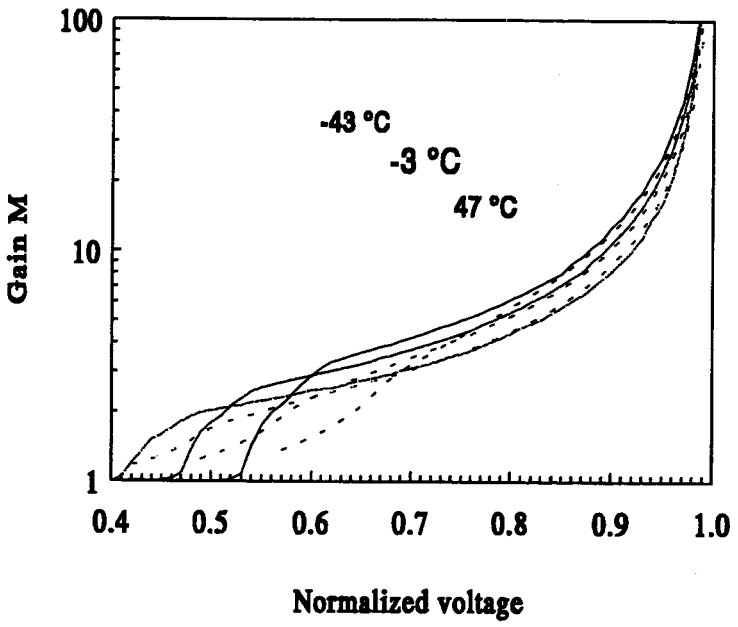

(b)

Figure 6.10 Normalized experimental (solid lines) and theoretical (dashed lines) M-V characteristics for different temperatures (APD32). (a) $t_{undoped} = 3.2\mu m$. (b) $t_{undoped} = 3.8\mu m$.

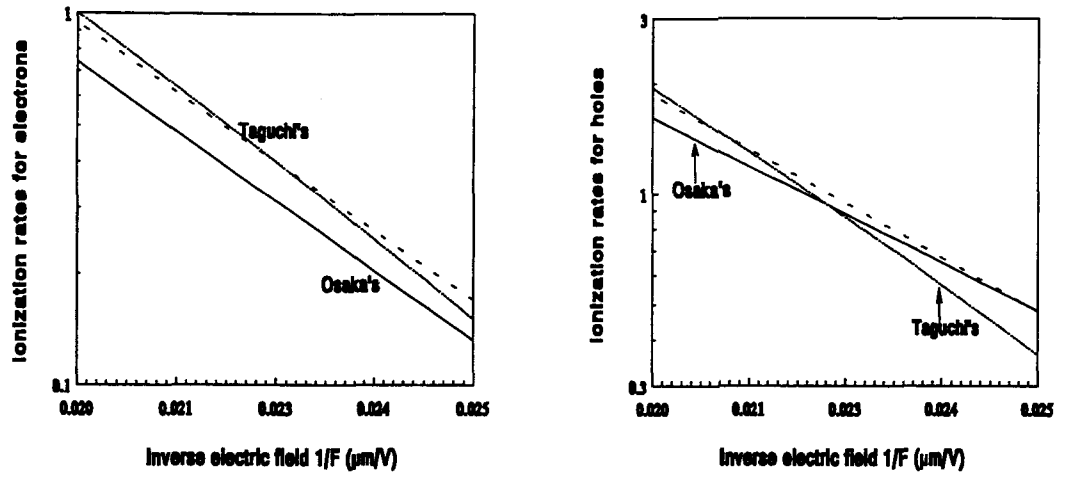

Figure 6.11 Comparison of InP ionizations rates (solid lines). Taguchi's ionization rates are calculated at 20 °C, and the dashed lines are the experimental room temperature InP ionization rates reported in the same publication.

3.2 μm rather than 3.8 μm is most likely the true value of $t_{undoped}$, since the modelling the M-V characteristics at room temperatures is very reliable, and supported by four independently reported InP ionization rates. It is even supported by the experimental room temperature InP ionization rates reported by Taguchi's in the same publication, which are different from the calculated ones at 20 °C. This discrepancy can be due to a few reasons. The values of the parameters used in the Okuto-Crowell theory for the temperature dependence of InP ionization rates are obtained by fitting to the experimental data for a number of temperatures. In addition, the range of the electric field in Figure 6.11 is much smaller than the range fitted. More importantly, all the experimental errors of the InP ionization rates are fairly large. Therefore, the temperature dependence of Taguchi's InP ionization rates are much more reliable than their absolute values at a particular temperature.

In conclusion, $t_{undoped} = 3.2\mu m$ with Osaka's InP ionization rates are the better combination for modelling the characteristics at room temperature, whereas $t_{undoped} = 3.8\mu m$ with Taguchi's InP ionization rates are the better combination for modelling the temperature

dependence of the characteristics. This is the best compromise unless a better expression for the temperature dependence of the InP ionization rates can be found.

6.6 Summary

In summary, the temperature dependence of breakdown voltage V_{br} in the SAGCM InP/InGaAs APDs with a range of device parameters from -40 °C to 110 °C is investigated. The experimental data shows that V_{br} is approximately a linear function of temperature, with a temperature coefficient η_{exp} between 0.13 and 0.16 V/°C. A physical model is developed, and it demonstrates that V_{br} indeed varies linearly with temperature with a temperature coefficient η_{the} approximately 0.155 V/°C. It is also shown that the electric field in the multiplication layer at breakdown is a linear function of temperature. It can explain successfully the small variation of η_{exp} among the APDs.

This physical model is also successfully applied to p^+-n and SAM InP-based APDs. Good agreement between the physical model predictions and experimental data of published InP-based APDs is obtained. This good agreement demonstrates that the proposed physical model is appropriate to model the temperature dependence of characteristics in any InP-based APDs. It is also demonstrated that the widely used expression for $V_{br}(T)$ with a relative temperature coefficient is only correct for long p^+-n InP-based diodes. The good agreement between the experimental and calculated $V_{br}(T)$ for the InP-based APDs implies that the temperature dependence of the impact ionization coefficients in InP is verified independently for the first time, and Taguchi's InP ionization rates is the best.

The temperature dependence of the M-V characteristics also is examined, and the results are satisfied within the uncertainties. This work is also very useful for further modelling the temperature dependence of the characteristics of InP-based APDs. It demonstrates that $t_{undoped} = 3.2\mu m$ with Osaka's InP ionization rates are better for modelling the

characteristics at room temperature, whereas $t_{undoped} = 3.8\mu m$ with Taguchi's InP ionization rates are better for modelling the temperature dependence of the characteristics.

Chapter 7 Dark current noise

Dark currents and their associated multiplication shot noises are potential sources of degradation to the sensitivity of the APDs [101]. In addition, flicker noises may be a powerful tool for finding sources of degradation in many electronic devices, including the APDs.

In this chapter, the dark current low frequency noise characteristics of the planar SAGCM InP/InGaAs APDs are investigated [101][101], including both multiplication shot and flicker noises.

7.1 Low frequency noise measurements

The low frequency noise spectra from 1 Hz to 100 KHz was measured with an HP3561A Dynamic Signal Analyzer (Figure 7.1). A low noise Ithaco 564 current amplifier was used to extend the sensitivity up to -270 dBA^2/Hz. APD14, APD32, APD34 and APD37 are investigated in this chapter, and all of them are from one wafer (P623).

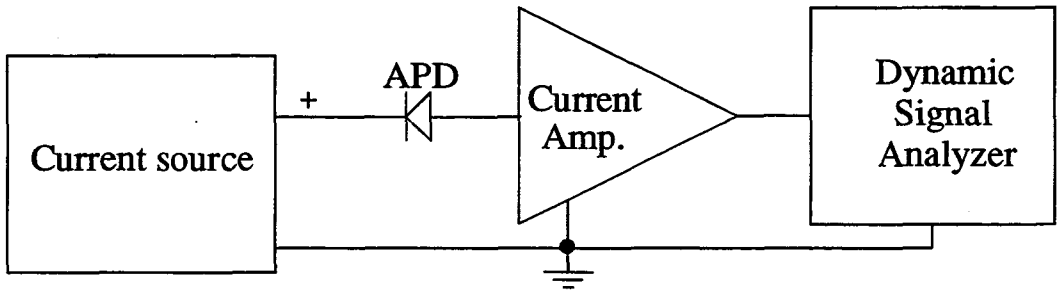

Figure 7.1 APD dark current low frequency noise measurement setup.

7.2 Multiplication shot noise

The multiplication shot noise spectra S_I is of a white noise type, and visible in all the APDs but one, APD37, which has a dominant flicker noise spectra. The multiplication shot noise spectra is measured at some I_d's with bias voltages $V>V_{mesa}$ so that $M>1$. Also I_d are selected to avoid the breakdown region since the very low dynamic resistance there would make measurements much less sensitive.

To understand quantitatively the multiplication shot noise, the results from APD32 and APD14 of S_I versus I_d are shown in Figure 7.2(a). The corresponding noise versus M (derived from the photocurrent measurement) are plotted in Figure 7.2(b). The linear relations in Figure 7.2(b) implies that the multiplication shot noises are proportional to some power of M, but not to I_d. Therefore, if we assume $I_d = I_{do}M$, where I_{do} is the primary dark current, then I_{do} varies with M. There are up to 10 dB differences between the two APDs at same I_d, whereas they are very close at same M. This shows that the shot noise sources are directly related to M rather than I_d, as expected. At a small range of M, S_I can be approximated to be proportional to M^{γ}, and for APD32 and APD14 they are fitted with γ's of 2.75±0.05 and 2.95±0.1, respectively. The corresponding k_{eff} is about 0.5. The error of measuring the low frequency noise spectra (1dB) prevents accurate calculations of F directly. The observed dark current multiplication shot noise is similar to what has been found in Ge APDs [101].

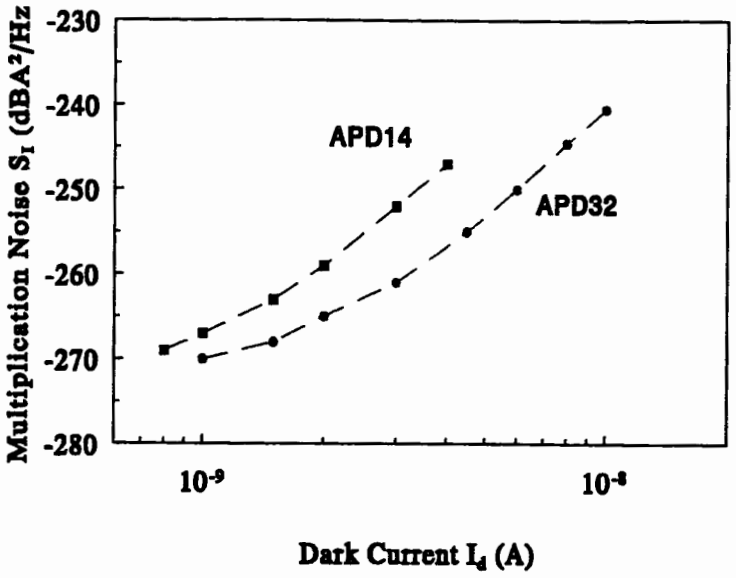

(a)

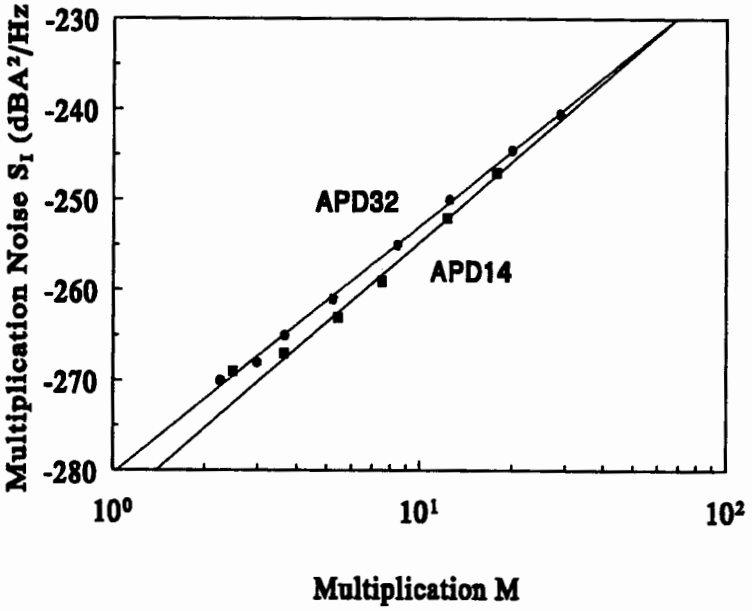

(b)

Figure 7.2 The multiplication shot noises versus (a) the dark currents, and (b) the multiplication gains M for APD32 and APD14. The noises are proportional to M^{γ} with γ 2.75±0.05 and 2.95±0.10 for APD32 and APD14, respectively.

7.3 Flicker noise

Flicker noises S_f are found in two APDs (APD37 and APD34). All the flicker noise spectra are fitted with

$$S_f(f) = b/f^{\alpha} = \kappa I_d^{\beta}/f^{\alpha} \tag{7.1}$$

where f is the frequency, α, β and κ are constants independent of both f and I_d, and $b = \kappa I_d^{\beta}$. A typical flicker noise spectra of APD37 at I_d=5nA is shown in Figure 7.3 with $\alpha = 1.0$ and the $b = 1.5 \times 10^{-22} A^2$. As seen in Figure 7.3, it is not a perfect fit to the flicker noise spectra. Hence, the fitted α's are distributed between 0.80 and 1.10 at different I_d for both APDs without clear correlation to either I_d or M. However, it is still very meaningful and interesting to compare the flicker noise at 10 Hz at different I_d as shown in Figure 7.4(a) for both APDs, or at different M in Figure 7.4(b).

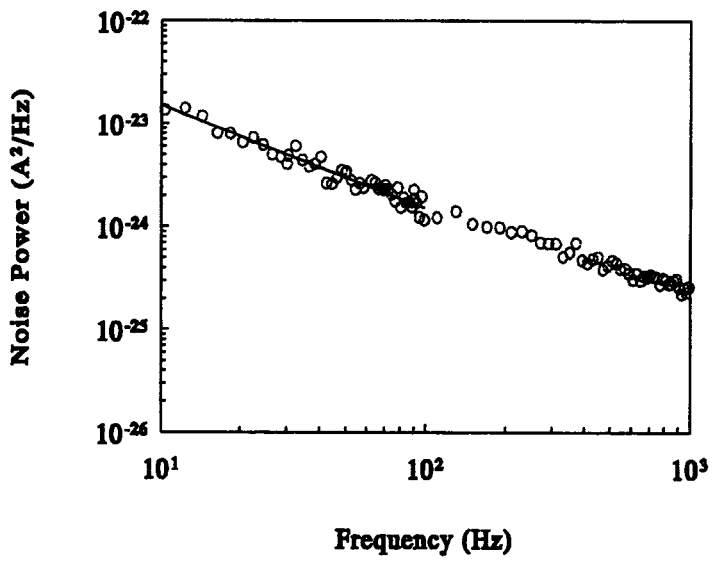

Figure 7.3 A typical (APD37, I_d=5nA) flicker noise spectra. The solid line is fitted to eqn. (7.1) with $\alpha = 1.0$ and $b = 1.5 \times 10^{-22} A^2$.

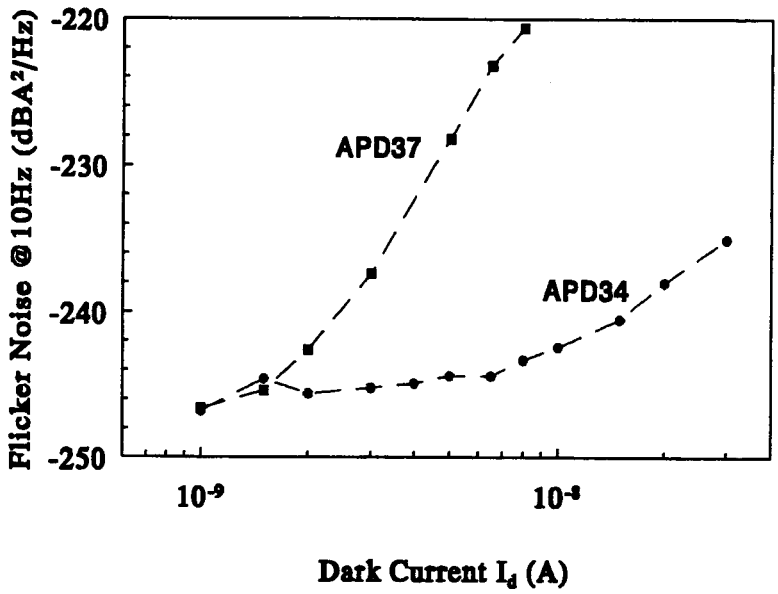

(a)

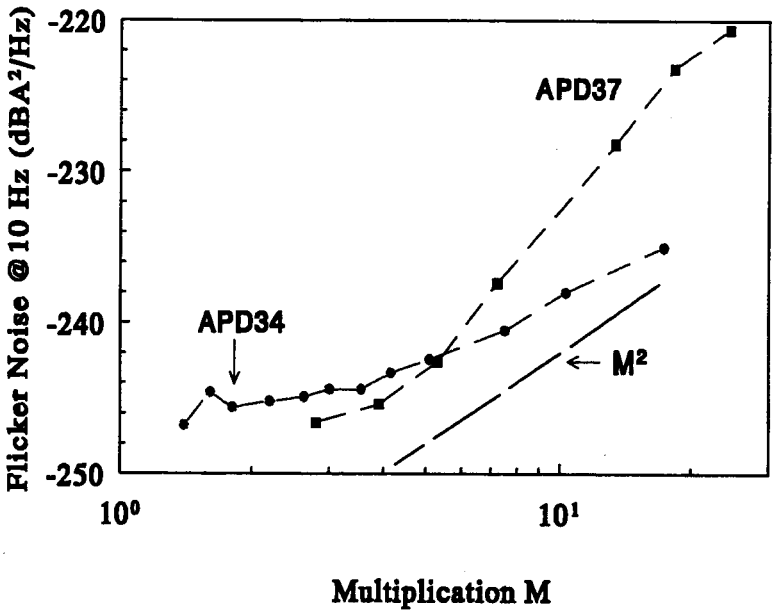

(b)

Figure 7.4 The flicker noises at 10Hz versus (a) the dark currents, and (b) the multiplication gains for APD34 and APD37. The solid line is from eqn. (7.2).

It is very important to note that the flicker noise spectra is found only in some of the APDs, whereas the multiplication shot noise spectra is found in all the APDs (except in the case where the flicker noise is too dominant), even though there are no fundamental differences between their dark current characteristics. This occurs because the dominant I_{do} is the generation-recombination current in the InGaAs layers for all the APDs. In addition, there are substantial differences in S_f for APD34 and APD37 at same I_d. A possible reason for this is that only a small portion of I_d, if any, contributes to the observed flicker noises.

It will be useful to understand what happens if a current with flicker noise spectra goes through an impact multiplication. Defining $S_f(I_{do})$ and $S_f(I_d)$ the flicker noises from I_{do} and I_d, respectively. In addition, it is assumed that $I_d = I_{do}M$. Since the multiplication process does not contribute an excess flicker noise (F=1) as in the case of multiplication shot noise, then,

$$S_f(I_d) = S_f(I_{do})M^2. \tag{7.2}$$

For APD34 at higher gains and APD37 at lower gains, the flicker noises do tend to follow eqn. (7.2). For APD34 at lower gains, it appears that a constant leakage current is the major contributor to the flicker noise. For APD37 at higher gains, the flicker noise increases faster than M^2, and a reasonable explanation is that I_{do} increases with M, too.

In conclusion, we find that the dark current multiplication shot noises are proportional to M^γ with γ about 2.75 - 2.95. The flicker noise is observed in some APDs and is believed to come from some leakage current sources.

Chapter 8 Conclusions and Recommendations

In this thesis, an extensive investigation on a state-of-art photodetector - planar separate absorption, grading, charge, and multiplication (SAGCM) InP/InGaAs avalanche photodiode (APD) with partial charge sheet in device periphery has been conducted. Specifically, the following was accomplished.

Device parameter extraction

A simple, innovative, and non-destructive technique has been invented to extract the two most critical device parameters in the SAGCM APDs, x_d and σ_{active}. To the author's best knowledge, the innovative use of V_{mesa} obtained from simple DC photocurrent measurements in this technique is novel. The technique was tested on two wafers, and the extracted values agreed very well with the independent measurements, such as Hall analysis, SIMS, and reflectance spectroscopy, within both the experimental and extraction errors.

The systematic errors have been considered in detail. The ionization in the absorption layer was found to cause significant errors only when F'_{heter} was higher than 17 V/μm. that is, x_d was increased by ~ 0.03 μm and σ_{active} was decreased by ~ 0.1×10^{12} cm^{-2}. The corresponding V_{br} was about 90 V if x_d is 0.4 to 0.5 μm. This effect was negligible for 90% of the APDs from a wafer. Also, it was found that for further modelling, Pearsall's rather than Osaka's InGaAs ionization rates were more consistent with this model and the experimental results.

The simplification of the zero doping concentration in the multiplication layer was found to cause very small systematic errors. The selection of either Umebu's or Cook's InP ionization rates was found to cause large systematic errors, but in opposite directions.

It has been argued that the best choice for the extraction and further investigations were Osaka's values.

The largest systematic error was contributed by the simplification of no ionization in the charge layer. x_d was increased by less than 0.03 μm and σ_{active} was decreased by less than 0.1×10^{12} cm^{-2}. The combination of this simplification, and the simplification of no ionization in the absorption layer would cause an unacceptable error 0.2×10^{12} cm^{-2} in σ_{active} when V_{br} was larger than 90 V. However, for the overwhelming majority of the APDs, the systematic errors were acceptable, and were dominated by the simplification of no ionization in the charge layer.

The random errors were contributed by the experimental errors of V_{mesa} and V_{br}, and by the fabrication and calibration errors of the device parameters used in the extraction. The uncertainties in V_{mesa} and $t_{undoped}$ were the dominant contributing sources of the random errors, and the over all random error for x_d was about ±0.05 μm, and for σ_{active} about $\pm0.09\times10^{12}$ cm^{-2}.

Photogain

It has been demonstrated both experimentally and physically that for our planar SAGCM InP/InGaAs APDs that the photogain is unity when $V_{ann} < V < V_{mesa}$, and the quantum efficiency did not depend on the bias voltage. The Miller empirical formula for M-V characteristics was shown to be very appropriate to our APDs with r between 0.6 and 1.5, and an empirical relation between the power coefficient r in the Miller empirical formula and experimental V_{br} was obtained. Finally, a physical model of the M-V characteristics was developed and proven to be successful in interpreting the experimental data from our APDs. It was also found that $t_{undoped}$ could be extracted from the experimental M-V characteristics – an improvement to the device parameter technique developed. The inclusions of the ionizations in the charge and absorption layers were not important in modelling the

M-V characteristics.

Temperature dependence of breakdown voltage and photogain

The temperature dependence of the breakdown voltage V_{br} in the SAGCM InP/ InGaAs APDs with a range of device parameters from -40 °C to 110 °C was investigated. The experimental data shows that V_{br} was approximately a linear function of temperature, with a temperature coefficient η_{exp} between 0.13 and 0.16 V/°C. A physical model was developed and it demonstrated that V_{br} indeed varied linearly with temperature with a temperature coefficient η_{the} about 0.155 V/°C. It was also shown that the electric field in the multiplication layer at breakdown was a linear function of temperature. The model could successfully explain the small variation of η_{exp} among the APDs.

This physical model was also successfully applied to p^+-n and SAM InP-based APDs. Good agreement between the physical model predictions and experimental data of published InP-based APDs was obtained. This good agreement demonstrated that the proposed physical model was appropriate to model the temperature dependence of characteristics in any InP-based APDs. It was also demonstrated that the widely used expression for $V_{br}(T)$ with a relative temperature coefficient was only correct for long p^+-n InP-based diodes. The good agreement between the experimental and calculated $V_{br}(T)$ for the InP-based APDs implied that the temperature dependence of the impact ionization coefficients in InP was verified independently for the first time, and Taguchi's InP ionization rates was the best. The temperature dependence of the M-V characteristics was also examined, and the results were satisfactory.

Dark current noise

Low frequency noise (LFN) in dark currents were investigated. It was found that for the SAGCM APDs investigated, the dark current multiplication shot noise was propor-

tional to M^{γ} with γ from 2.75 to 2.95, which was in general agreement with theory. Flicker noise was also observed in some of the SAGCM APDs and it was believed to be due to leakage currents from surface/interface imperfections/defects.

The major contributions from this thesis make it possible 1) to extract critical device parameters fast and non-destructively, which is critical for monitoring fabrication and further detailed modelling; 2) to develop and verify a general theory of breakdown voltages and its temperature dependence; 3) to accurately calculate photogain versus bias voltage and its temperature dependence; 4) to understand dark current noise; 5) to help to understand the degradation sources from low frequency noise spectra; 6) and to lay solid foundation to characterize and model more operating (high frequency) characteristics of APDs, such as bandwidth and multiplication noise.

Appendix A Electric field in SAGCM APD

The electric field F(x) is related to the net doping concentration N(x) by the Poisson equation

$$\frac{d}{dx}F(x) = -\frac{q}{\varepsilon_0 \varepsilon}N(x), \tag{A.1}$$

where ε is the relative dielectric constant and ε_0 is the dielectric constant of vacuum. In the following, the one-dimensional Poisson equation is applied to the central active region. Before deriving the electric field in SAGCM InP/InGaAs APD, a few assumptions and simplifications are made:

- p^+-n is an abrupt junction.
- The voltage drop at the InP/InGaAs heterointerface (0.1-0.4) is ignored.
- The doping concentrations in the multiplication, charge and grading layers are uniform.
- The thickness of the boost layer is ignored.
- The relative dielectric constant of the InGaAsP grading layer is equal to the relative dielectric constant of InP.
- The InP buffer layer is treated as part of the absorption layer.

All the symbols are defined in Figure 3.2, Figure A.1, and Table 3.1.

The electric field as a function of bias voltage V is derived according to the bias range. Let us define V_{mesa} as the bias voltage at which the electric field starts to penetrate the boost layer, V'_{mesa} as the bias voltage at which the electric field starts to penetrate the absorption layer, and $V_{depleted}$ as the bias voltage at which the electric field reaches the n^+ InP substrate. Obviously, $V_{mesa} \le V'_{mesa} \le V_{depleted}$.

$x_1 - x_d = t_{InP}$ $x_2 - x_1 = t_{grading}$ $x_3 - x_2 = t_{undoped}$ $x_0 - x_2 = t_0$ $x - x_2 = t$

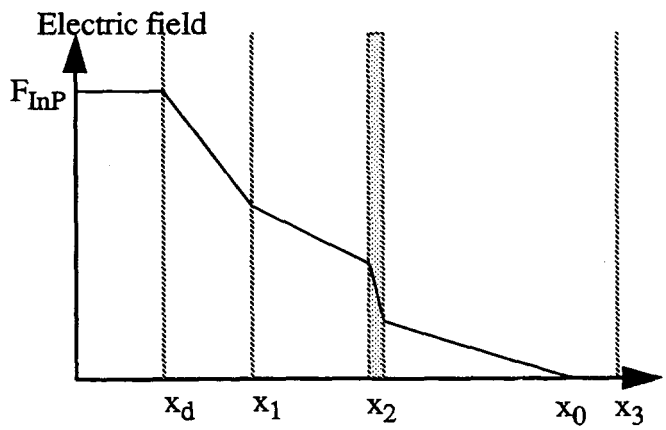

Figure A.1 The electric fields in SAGCM InP/InGaAs APD.

A.1 $V \geq V'_{mesa}$

When the electric field is non-zero in the absorption layer, the electric field F(x) is

$$F(x) = \begin{cases} F_{InP} - \dfrac{qN_D}{\varepsilon_0\varepsilon_1}x & 0 \leq x \leq x_d \\ F_{InP} - \dfrac{qN_D}{\varepsilon_0\varepsilon_1}x_d - \dfrac{q\sigma_{charge}}{\varepsilon_0\varepsilon_1}\dfrac{(x-x_d)}{t_{InP}} & x_d \leq x \leq x_1 \\ F_{InP} - \dfrac{qN_D}{\varepsilon_0\varepsilon_1}x_d - \dfrac{q\sigma_{charge}}{\varepsilon_0\varepsilon_1} - \dfrac{qN_G}{\varepsilon_0\varepsilon_1}(x-x_1) & x_1 \leq x \leq x_2 \\ F_{InP} - \dfrac{qN_D}{\varepsilon_0\varepsilon_1}x_d - \dfrac{q\sigma_{charge}}{\varepsilon_0\varepsilon_1} - \dfrac{qN_G t_{grading}}{\varepsilon_0\varepsilon_1} - \dfrac{q\sigma_{InGaAs}}{\varepsilon_0\varepsilon_2} - \dfrac{q}{\varepsilon_0\varepsilon_2}\int_0^t N(t')\,dt' & 0 \leq t \leq t_0 \leq t_{undoped} \end{cases} \quad \text{(A.2)}$$

with ε_1 and ε_2, the relative dielectric constants for InP and InGaAs, and having values of 12.3 and 12.9 respectively. The bias voltage is given by

$$V + V_{bi} = F_{InP}(x_d + t_{InP} + t_{grading} + t_0) - \frac{qN_D x_d}{\varepsilon_1 \varepsilon_0}(x_d/2 + t_{InP} + t_{grading} + t_0)$$
$$- \frac{q\sigma_{charge}}{\varepsilon_1 \varepsilon_0}(t_{InP}/2 + t_{grading} + t_0) - \frac{qN_G t_{grading}}{\varepsilon_2 \varepsilon_0}(t_{grading}/2 + t_0) \qquad \textbf{(A.3)}$$
$$- \frac{q\sigma_{InGaAs}}{\varepsilon_2 \varepsilon_0} t_0 - \frac{q}{\varepsilon_2 \varepsilon_0} \int_0^{t_0} dt \int_0^{t} N(t')\, dt'$$

where V_{bi} is the zero bias potential and is about 1.0 V, and t_0 has to be found out in two cases:

1. $V \geq V_{depleted}$, (i.e., the absorption layer is completely depleted). In this case, $t_0 = t_{undoped}$, which can be substituted into eqn. (A.3) to derive the bias V.

2. $V \leq V_{depleted}$, the electric field is zero at the location x_0. Thus, t_0 is related to F_{InP} from eqn. (A.2)

$$F_{InP} = \frac{qN_D}{\varepsilon_0 \varepsilon_1} x_d + \frac{q\sigma_{charge}}{\varepsilon_0 \varepsilon_1} + \frac{qN_G t_{grading}}{\varepsilon_0 \varepsilon_1} + \frac{q\sigma_{InGaAs}}{\varepsilon_0 \varepsilon_2} + \frac{q}{\varepsilon_0 \varepsilon_2} \int_0^{t_0} N(t')\, dt' \qquad \textbf{(A.4)}$$

Substituting eqn. (A.4) into eqn. (A.3), t_0 is related to the bias V by

$$V + V_{bi} = \frac{qN_D x_d^2/2}{\varepsilon_0 \varepsilon_1} + \frac{q\sigma_{charge}}{\varepsilon_1 \varepsilon_0}(x_d + t_{InP}/2) + \frac{qN_G t_{grading}}{\varepsilon_2 \varepsilon_0}(x_d + t_{InP} + t_{grading}/2)$$
$$+ \frac{q\sigma_{InGaAs}}{\varepsilon_2 \varepsilon_0}(x_d + t_{InP} + t_{grading}) + \frac{q}{\varepsilon_2 \varepsilon_0}\left[(x_d + t_{InP} + t_{grading} + t_0)\int_0^{t_0} N(t')\, dt' - \int_0^{t_0} dt \int_0^{t} N(t')\, dt'\right] \qquad \textbf{(A.5)}$$

$V = V'_{mesa}$ when t_0=0. Thus

$$V'_{mesa} = \frac{qN_D x_d^2/2}{\varepsilon_0 \varepsilon_1} + \frac{q\sigma_{charge}}{\varepsilon_1 \varepsilon_0}(x_d + t_{InP}/2) + \frac{qN_G t_{grading}}{\varepsilon_2 \varepsilon_0}(x_d + t_{InP} + t_{grading}/2)$$
$$+ \frac{q\sigma_{InGaAs}}{\varepsilon_2 \varepsilon_0}(x_d + t_{InP} + t_{grading}) - V_{bi}. \qquad \textbf{(A.6)}$$

$V = V_{depleted}$ when t_0=$t_{undoped}$. Therefore,

$$V_{depleted} = V'_{mesa} + \frac{q}{\varepsilon_2\varepsilon_0}\left[(x_d + t_{InP} + t_{grading} + t_{undoped})\int_0^{t_{undoped}} N(t')\,dt' - \int_0^{t_{undoped}} dt\int_0^{t} N(t')\,dt'\right] \quad \textbf{(A.7)}$$

Then eqn. (A.5) can be rewritten as

$$V = V'_{mesa} + \frac{q}{\varepsilon_2\varepsilon_0}\left[(x_d + t_{InP} + t_{grading} + t_0)\int_0^{t_0} N(t')\,dt' - \int_0^{t_0} dt\int_0^{t} N(t')\,dt'\right]. \quad \textbf{(A.8)}$$

Obviously, $V'_{mesa} \le V \le V_{depleted}$.

A.2 $V_{mesa} \le V \le V'_{mesa}$

The electric field in the absorption layer is zero but non zero in the grading layer. The electric fields are

$$F(x) = \begin{cases} F_{InP} - \dfrac{qN_D}{\varepsilon_0\varepsilon_1}x & 0 \le x \le x_d \\ F_{InP} - \dfrac{qN_D}{\varepsilon_0\varepsilon_1}x_d - \dfrac{q\sigma_{charge}}{\varepsilon_0\varepsilon_1}\dfrac{(x-x_d)}{t_{InP}} & x_d \le x \le x_1 \\ F_{InP} - \dfrac{qN_D}{\varepsilon_0\varepsilon_1}x_d - \dfrac{q\sigma_{charge}}{\varepsilon_0\varepsilon_1} - \dfrac{qN_G}{\varepsilon_0\varepsilon_1}(x-x_1) & x_1 \le x \le x_2 \\ 0 & 0 \le t \le t_0 \le t_{undoped} \end{cases} \quad \textbf{(A.9)}$$

The bias voltage is given by

$$\begin{aligned} V + V_{bi} = {} & F_{InP}(x_d + t_{InP} + t_{grading}) - \frac{qN_D x_d}{\varepsilon_1\varepsilon_0}(x_d/2 + t_{InP} + t_{grading}) \\ & - \frac{q\sigma_{charge}}{\varepsilon_1\varepsilon_0}(t_{InP}/2 + t_{grading}) - \frac{qN_G(t_{grading}^2/2)}{\varepsilon_2\varepsilon_0}. \end{aligned} \quad \textbf{(A.10)}$$

The V_{mesa} is defined when $F_{InP} = \dfrac{qN_D}{\varepsilon_0\varepsilon_1}x_d + \dfrac{q\sigma_{charge}}{\varepsilon_0\varepsilon_1} + \dfrac{qN_G}{\varepsilon_0\varepsilon_1}t_{grading}$, so that

$$V_{mesa} + V_{bi} = \frac{qN_D(x_d^2/2)}{\varepsilon_0\varepsilon_1} + \frac{q\sigma_{charge}}{\varepsilon_0\varepsilon_1}(x_d + t_{InP}/2) + \frac{qN_G t_{grading}}{\varepsilon_2\varepsilon_0}(x_d + t_{InP} + t_{grading}/2). \quad \textbf{(A.11)}$$

The two punchthrough voltages are related by

$$V'_{mesa} = V_{mesa} + \frac{q\sigma_{InGaAs}}{\varepsilon_2\varepsilon_0}(x_d + t_{InP} + t_{grading}). \quad \textbf{(A.12)}$$

Appendix B Listings of mathematical files

The following files were written with Mathcad 4.0.

B.1 Parameter extraction

Calculations of xd and sigma from room temperature experimental values Vbr and Vmesa for the cases of InP only.
Temperature T is 300 K always, even though it looks like T as an varialbe.

InP impact ionization coefficients from Osaka interpreted by himself in another paper.
Valid between 40 to 60 V/micron

$$\alpha_1(F,T) := 555 \cdot \exp\left(\frac{-310}{F}\right) \qquad \beta_1(F,T) := 198 \cdot \exp\left(\frac{-229}{F}\right)$$

Some device parameters

$\varepsilon 1 := 12.3$	InP dielectric const
$\varepsilon 2 := 12.9$	InGaAs directric const
$\varepsilon 0 := 8.8541878210^{-18}$	Dielectric const in F/micron
$q := 1.6 \cdot 10^{-19}$	electron charge
$V_{bi} := 1.0$	Zero bias potential
$N_D := 10^{15} \cdot 10^{-12} \cdot 0.7$	doping level in InGaAs in 1/micron^3
$N_G := 10^{16} \cdot 10^{-12} \cdot 1.0$	doping level in InGaAs in 1/micron^3
$t_{InP} := 0.17$	Charge layer thickness in micron
$t_{grading} := 0.09$	Grading layer thickness in micron
$\sigma_{InGaAs} := 0.4 \cdot 10^{12} \cdot 10^{-8}$	Doped InGaAs charge sheet density in micron^-2.
$x_{undoped} := 3.8$	undoped layer thickness in micron

Calculations in the case of InP ionization only.

$$\text{Left}(F,w,\sigma,T) := \frac{\alpha_1(F,T)}{\alpha_1(F,T) - \beta_1(F,T)} \cdot \exp\left[\left(\beta_1(F,T) - \alpha_1(F,T)\right) \cdot w\right] - \frac{\beta_1(F,T)}{\alpha_1(F,T) - \beta_1(F,T)}$$

$$\text{BVRIGHT} := (-1) \cdot \frac{q \cdot N_G \cdot t_{grading}}{\varepsilon 2 \cdot \varepsilon 0} \cdot \left(\frac{t_{grading}}{2} + x_{undoped}\right) - \frac{q \cdot \sigma_{InGaAs}}{\varepsilon 2 \cdot \varepsilon 0} \cdot x_{undoped} - \frac{q \cdot N_D \cdot x_{undoped}^2}{\varepsilon 2 \cdot \varepsilon 0 \cdot 2}$$

Guess Values: $Fbr := 60$ $w := 0.3$ $\sigma := 3 \cdot 10^{12} \cdot 10^{-8}$

Given

$$Vmesa + V_{bi} = \frac{q \cdot \sigma}{\varepsilon 1 \cdot \varepsilon 0} \cdot \left(w + \frac{t_{InP}}{2} \right) + \frac{q \cdot N_G \cdot t_{grading}}{\varepsilon 2 \cdot \varepsilon 0} \cdot \left(w + t_{InP} + \frac{t_{grading}}{2} \right)$$

$$BV = \left[Fbr \cdot \left(w + t_{InP} + x_{undoped} + t_{grading} \right) - \frac{q \cdot \sigma}{\varepsilon 1 \cdot \varepsilon 0} \cdot \left(\frac{t_{InP}}{2} + x_{undoped} + t_{grading} \right) \right] + BVRIGHT - V_{bi}$$

$Left(Fbr, w, \sigma, 300) = 0$

$func(Vmesa, BV) := Find(Fbr, w, \sigma)$

Wafer P623 experimental voltages

$$Distance := \begin{bmatrix} 5.0 \\ 8.5 \\ 11.5 \\ 14.5 \\ 18.0 \\ 21.0 \\ 23.5 \\ 26.5 \\ 29.5 \\ 32.5 \\ 35.5 \\ 39.0 \\ 41.5 \\ 44.5 \end{bmatrix} \quad EVmesa := \begin{bmatrix} 16 \\ 16 \\ 18 \\ 19 \\ 21 \\ 22 \\ 23 \\ 24 \\ 24 \\ 24 \\ 22 \\ 21 \\ 20 \\ 14 \end{bmatrix} \quad EVbr := \begin{bmatrix} 85 \\ 79 \\ 74 \\ 69 \\ 63 \\ 58 \\ 55 \\ 51 \\ 48 \\ 45 \\ 43 \\ 39 \\ 29 \\ 46 \end{bmatrix}$$

$j := 0..10$

$M_{j,0} := Distance_{j+1}$ $M_{j,1} := EVmesa_{j+1}$ $M_{j,2} := EVbr_{j+1}$

$M_{j,3} := func(M_{j,1}, M_{j,2})_0$ Fbr

$M_{j,4} := func(M_{j,1}, M_{j,2})_1$ xd

$sigma_j := func(M_{j,1}, M_{j,2})_2$ sigma in micron^-2.

$$M_{j,5} := \left[sigma_j + \left(\sigma_{InGaAs} + N_G \cdot t_{grading} \right) \right] \cdot 10^{-4}$$ total active charge in 1e12 cm^-2.

$$M_{j,6} := M_{j,1} + \frac{q \cdot \sigma_{InGaAs}}{\varepsilon 2 \cdot \varepsilon 0} \cdot \left(M_{j,4} + t_{InP} + t_{grading} \right)$$ Vmesa prime

$$M_{j,7} := M_{j,6} + \frac{q \cdot N_D \cdot x_{undoped}}{\varepsilon 2 \cdot \varepsilon 0} \cdot \left(M_{j,4} + t_{InP} + t_{grading} + \frac{x_{undoped}}{2} \right)$$ Vdepleted

$$M_{j,8} := M_{j,3} - \frac{q \cdot sigma_j}{\varepsilon 1 \cdot \varepsilon 0} - \frac{q \cdot N_G \cdot t_{grading}}{\varepsilon 2 \cdot \varepsilon 0}$$ Fheter

$$M_{j,9} := M_{j,8} - \frac{q \cdot \sigma_{InGaAs}}{\varepsilon 2 \cdot \varepsilon 0}$$ Fheter prime

The results for wafer P623

$$M = \begin{bmatrix}
8.5 & 16 & 79 & 54.963 & 0.403 & 2.752 & 19.716 & 29.266 & 20.473 & 14.869 \\
11.5 & 18 & 74 & 53.653 & 0.454 & 2.784 & 21.999 & 31.739 & 18.692 & 13.089 \\
14.5 & 19 & 69 & 53.393 & 0.465 & 2.86 & 23.062 & 32.843 & 17.32 & 11.717 \\
18 & 21 & 63 & 52.564 & 0.503 & 2.932 & 25.275 & 35.197 & 15.423 & 9.819 \\
21 & 22 & 58 & 52.399 & 0.511 & 3.012 & 26.32 & 36.273 & 14.083 & 8.479 \\
23.5 & 23 & 55 & 52.071 & 0.528 & 3.053 & 27.413 & 37.427 & 13.16 & 7.557 \\
26.5 & 24 & 51 & 51.858 & 0.539 & 3.114 & 28.476 & 38.532 & 12.041 & 6.437 \\
29.5 & 24 & 48 & 52.115 & 0.525 & 3.174 & 28.4 & 38.406 & 11.422 & 5.818 \\
32.5 & 24 & 45 & 52.37 & 0.512 & 3.234 & 28.328 & 38.286 & 10.798 & 5.195 \\
35.5 & 22 & 43 & 53.79 & 0.448 & 3.32 & 25.968 & 35.686 & 10.952 & 5.349 \\
39 & 21 & 39 & 54.894 & 0.406 & 3.434 & 24.729 & 34.289 & 10.384 & 4.781
\end{bmatrix}$$

WRITEPRN(p623) := M write to the file p623.prn

B.2 M-V

Calculations of gain at room temperatuers. Vdepleted<Vbr case. InP ionization only.

InP impact ionization coefficients, the electric field

$$\alpha_1(F,T) := 555 \cdot \exp\left(\frac{-310}{F}\right) \qquad \beta_1(F,T) := 198 \cdot \exp\left(\frac{-229}{F}\right)$$

$$k_1(F,T) := \frac{\alpha_1(F,T)}{\beta_1(F,T)}$$

Some device parameters

$\varepsilon 1 := 12.3$	InP dielectric const
$\varepsilon 2 := 12.9$	InGaAs directric const
$\varepsilon 0 := 8.8541878210^{-18}$	Dielectric const in F/micron
$q := 1.6 \cdot 10^{-19}$	
$V_{bi} := 1.0$	Zero bias potential
$N_D := 10^{15} \cdot 10^{-12} \cdot 0.7$	doping level in InGaAs in 1/micron^3
$N_G := 10^{16} \cdot 10^{-12} \cdot 1.0$	doping level in InGaAs in 1/micron^3
$t_{InP} := 0.17$	Charge layer width in micron
$t_{grading} := 0.09$	Grading layer thickness in micron
$\sigma_{InGaAs} := 0.4 \cdot 10^{12} \cdot 10^{-8}$	Doped InGaAs charge sheet density in micron^-2.
$x_{undoped} := 3.8$	undoped layer width in micron

Calculations in the case of InP ionization only.

$$Left(F,w,\sigma,T) := \frac{\alpha_1(F,T)}{\alpha_1(F,T) - \beta_1(F,T)} \cdot \exp\left[\left(\beta_1(F,T) - \alpha_1(F,T)\right) \cdot w\right] - \frac{\beta_1(F,T)}{\alpha_1(F,T) - \beta_1(F,T)}$$

$$BVRIGHT := (-1) \cdot \frac{q \cdot N_G \cdot t_{grading}}{\varepsilon 2 \cdot \varepsilon 0} \cdot \left(\frac{t_{grading}}{2} + x_{undoped}\right) - \frac{q \cdot \sigma_{InGaAs}}{\varepsilon 2 \cdot \varepsilon 0} \cdot x_{undoped} - \frac{q \cdot N_D \cdot x_{undoped}^2}{\varepsilon 2 \cdot \varepsilon 0 \cdot 2}$$

Guess Values: $Fbr := 60$ $w := 0.3$ $\sigma := 3 \cdot 10^{12} \cdot 10^{-8}$

Given

$$Vmesa + V_{bi} = \frac{q \cdot \sigma}{\varepsilon 1 \cdot \varepsilon 0} \cdot \left(w + \frac{t_{InP}}{2} \right) + \frac{q \cdot N_G \cdot t_{grading}}{\varepsilon 2 \cdot \varepsilon 0} \cdot \left(w + t_{InP} + \frac{t_{grading}}{2} \right)$$

$$BV = \left[Fbr \cdot \left(w + t_{InP} + x_{undoped} + t_{grading} \right) - \frac{q \cdot \sigma}{\varepsilon 1 \cdot \varepsilon 0} \cdot \left(\frac{t_{InP}}{2} + x_{undoped} + t_{grading} \right) \right] + BVRIGHT - V_{bi}$$

$Left(Fbr, w, \sigma, 300) = 0$

$func(Vmesa, BV) := Find(Fbr, w, \sigma)$ device parameter extraction

$EXVmesa := 20.6$ $EXVbr := 70.44$ $IN := READPRN(apd34)$ reading in experimental M-V

$$\begin{bmatrix} Fbr \\ x_d \\ \sigma_{charge} \end{bmatrix} := func(EXVmesa, EXVbr)$$

$$\sigma_{active} := \left[\sigma_{charge} + \left(\sigma_{InGaAs} + N_G \cdot t_{grading} \right) \right]$$

$$Vpmesa := EXVmesa + \frac{q \cdot \sigma_{InGaAs}}{\varepsilon 2 \cdot \varepsilon 0} \cdot \left(x_d + t_{InP} + t_{grading} \right)$$

$$Vdepleted := Vpmesa + \frac{q \cdot N_D \cdot x_{undoped}}{\varepsilon 2 \cdot \varepsilon 0} \cdot \left(x_d + t_{InP} + t_{grading} + \frac{x_{undoped}}{2} \right)$$

$$Fheter(Fbr) := Fbr - \frac{q \cdot \sigma_{charge}}{\varepsilon 1 \cdot \varepsilon 0} - \frac{q \cdot N_G \cdot t_{grading}}{\varepsilon 2 \cdot \varepsilon 0}$$ Fheter

$$Fpheter(Fbr) := Fheter(Fbr) - \frac{q \cdot \sigma_{InGaAs}}{\varepsilon 2 \cdot \varepsilon 0}$$ Fheter prime

$$Fend(Fbr) := Fpheter(Fbr) - \frac{q \cdot N_D \cdot x_{undoped}}{\varepsilon 2 \cdot \varepsilon 0}$$ Fend

$EXVmesa = 20.6$ $EXVbr = 70.44$ APD14

$Fbr = 52.085$ $x_d = 0.527$ $\sigma_{charge} = 2.299 \cdot 10^{4}$

$\sigma_{active} = 2.789 \cdot 10^{4}$ $Vpmesa = 25.009$ $Vdepleted = 35.021$

$Fheter(Fbr) = 17.051$ $Fpheter(Fbr) = 11.448$ $Fend(Fbr) = 7.722$

When Vmesa<V<Vpmesa, the electric field in the multiplication layer is

$$F1_{InP}(v) := \frac{v + V_{bi} + \frac{q \cdot \sigma_{charge}}{\varepsilon 1 \cdot \varepsilon 0} \cdot \left(\frac{t_{InP}}{2} + t_{grading} \right) + \frac{q \cdot N_G \cdot t_{grading}}{\varepsilon 2 \cdot \varepsilon 0} \cdot \frac{t_{grading}}{2}}{\left(x_d + t_{InP} + t_{grading} \right)}$$

When Vpmesa<V<Vu, the depletion width (relative to t(undoped)) is

$$a := \frac{q \cdot N_D \cdot x_{undoped}^2}{\varepsilon 2 \cdot \varepsilon 0 \cdot 2} \qquad b := \frac{q \cdot N_D \cdot x_{undoped}}{\varepsilon 2 \cdot \varepsilon 0} \cdot \left(x_d + t_{InP} + t_{grading}\right)$$

$$c(v) := Vpmesa - v \qquad t(v) := \frac{-b + \sqrt{b^2 - 4 \cdot a \cdot c(v)}}{2 \cdot a}$$

The electric field in the multiplication layer is

$$F2_{InP}(v) := \frac{q \cdot \sigma_{charge}}{\varepsilon 1 \cdot \varepsilon 0} + \frac{q \cdot N_G \cdot t_{grading}}{\varepsilon 2 \cdot \varepsilon 0} + \frac{q \cdot \sigma_{InGaAs}}{\varepsilon 2 \cdot \varepsilon 0} + \frac{q \cdot N_D \cdot x_{undoped}}{\varepsilon 2 \cdot \varepsilon 0} \cdot t(v)$$

When Vdepleted<V<Vbr, the electric field in the multiplication layer is

$$F3_{InP}(v) := \frac{\left[v + V_{bi} + \frac{q \cdot \sigma_{charge}}{\varepsilon 1 \cdot \varepsilon 0} \cdot \left(\frac{t_{InP}}{2} + t_{grading} + x_{undoped}\right)\right] - BVRIGHT}{\left(x_d + t_{InP} + t_{grading} + x_{undoped}\right)}$$

The the electric field in the multiplcaiton layer for V>V1mesa is

$$F_{InP}(v) := F1_{InP}(v) \cdot \Phi(Vpmesa - v) + F2_{InP}(v) \cdot \Phi(v - Vpmesa) \cdot \Phi(Vdepleted - v) \ldots$$
$$+ F3_{InP}(v) \cdot \Phi(v - Vdepleted)$$

Multiplication Gain

$$M(V,T) := \frac{1 - k_1\left(F_{InP}(V), T\right)}{\exp\left[\left(\alpha_1\left(F_{InP}(V), T\right) - \beta_1\left(F_{InP}(V), T\right)\right) \cdot x_d\right] - k_1\left(F_{InP}(V), T\right)}$$

$T := 300$

$EXVmesa = 20.6$ $\quad Vdepleted = 35.021$ $\quad EXVbr = 70.44$

$$sorta(x) := \frac{ceil(x \cdot 5)}{5} \qquad sortb(x) := \frac{floor(x \cdot 5)}{5}$$

$start := sorta(EXVmesa)$ $\quad end := sortb(EXVbr)$

$$endnumber := if\left(rows(IN) < \frac{end - start}{0.2}, rows(IN) - 1, \frac{end - start}{0.2} - 1\right)$$

$j := 0, 1 .. endnumber$

$OUT_{j,0} := sorta(EXVmesa) + 0.2 \cdot j$

$OUT_{j,1} := M(OUT_{j,0}, 300)$

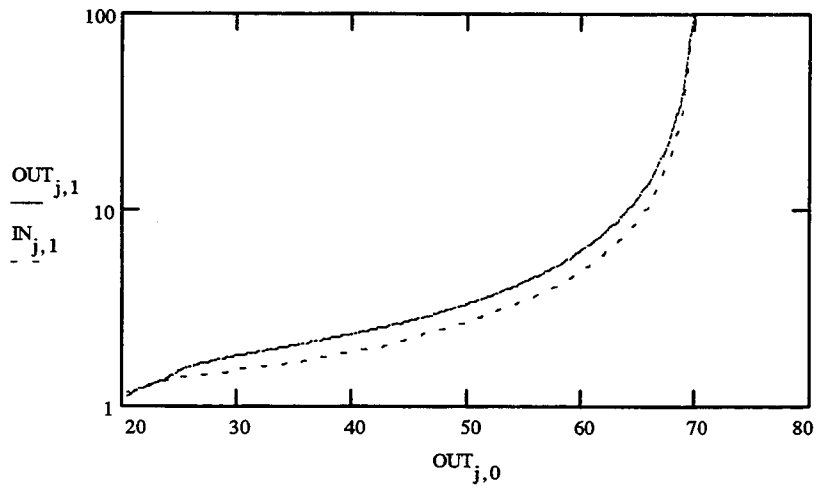

WRITEPRN(tmp) := OUT write to the file tmp.prn

B.3 Temperature dependence of V_{br}

Calculations of Vbr versus T with input xd and sigma with InP only ionization.
This is the complete numerical model.

InP impact ionization coefficients from Taguchi, which was fitted to their own data (25 C to 175 C). The theory was from Okuto-Crowell.

The equations for free path length (in micro) and phonon energy (In eV) in InP.

$E_{R0e} := 46 \cdot 10^{-3}$ $E_{R0h} := 36 \cdot 10^{-3}$ $\lambda_{0e} := 41.7 \cdot 10^{-4}$ $\lambda_{0h} := 41.3 \cdot 10^{-4}$

The equations for free path length (in micro) and phonon energy (In eV) in InP.

$$\lambda_e(T) := \lambda_{0e} \cdot \tanh\left(\frac{E_{R0e}}{2 \cdot k \cdot T}\right) \qquad \lambda_e(300) = 0.003$$

$$\lambda_h(T) := \lambda_{0h} \cdot \tanh\left(\frac{E_{R0h}}{2 \cdot k \cdot T}\right) \qquad \lambda_h(300) = 0.0025$$

$$E_{Re}(T) := E_{R0e} \cdot \tanh\left(\frac{E_{R0e}}{2 \cdot k \cdot T}\right) \qquad E_{Re}(300) = 0.0327$$

$$E_{Rh}(T) := E_{R0h} \cdot \tanh\left(\frac{E_{R0h}}{2 \cdot k \cdot T}\right) \qquad E_{Rh}(300) = 0.0216$$

The calculations of threshold energies

$$E_g(T) := 1.421 - \frac{3.63 \cdot 10^{-4} \cdot T^2}{T + 162} \qquad E_g(300) = 1.3503$$

$$E_{ie}(T) := E_g(T) \cdot \frac{1.84}{E_g(300)} \qquad E_{ie}(300) = 1.84$$

$$E_{ih}(T) := E_g(T) \cdot \frac{1.65}{E_g(300)} \qquad E_{ih}(300) = 1.65$$

$$\alpha_1(F,T) := \frac{F}{E_{ie}(T)} \cdot \exp\left[0.217 \cdot \left(\frac{E_{ie}(T)}{E_{Re}(T)}\right)^{1.14} - \left[\left[0.217 \cdot \left(\frac{E_{ie}(T)}{E_{Re}(T)}\right)^{1.14}\right]^2 + \left(\frac{E_{ie}(T)}{F \cdot \lambda_e(T)}\right)^2\right]^{0.5}\right]$$

$$\beta_1(F,T) := \frac{F}{E_{ih}(T)} \cdot \exp\left[0.217 \cdot \left(\frac{E_{ih}(T)}{E_{Rh}(T)}\right)^{1.14} - \left[\left[0.217 \cdot \left(\frac{E_{ih}(T)}{E_{Rh}(T)}\right)^{1.14}\right]^2 + \left(\frac{E_{ih}(T)}{F \cdot \lambda_h(T)}\right)^2\right]^{0.5}\right]$$

Some device parameters

$\varepsilon 1 := 12.3$	InP dielectric const
$\varepsilon 2 := 12.9$	InGaAs directric const
$\varepsilon 0 := 8.8541878210^{-18}$	Dielectric const in F/micron
$q := 1.6 \cdot 10^{-19}$	electron charge
$V_{bi} := 1.0$	Zero bias potential
$N_D := 10^{15} \cdot 10^{-12} \cdot 0.7$	doping level in InGaAs in 1/micron^3
$N_G := 10^{16} \cdot 10^{-12} \cdot 1.0$	doping level in InGaAs in 1/micron^3
$t_{InP} := 0.17$	Charge layer width in micron
$t_{grading} := 0.09$	Grading layer thickness in micron
$\sigma_{InGaAs} := 0.4 \cdot 10^{12} \cdot 10^{-8}$	Doped InGaAs charge sheet density in micron^-2.
$t_{undoped} := 3.2$	undoped layer width in micron

Calculations in the case of InP ionization only.

$w1 := 0.562 \qquad \sigma 1 := 2.72 \cdot 10^{4} \qquad$ APD14

Guess Values: $Fbr1 := 55$

Given

$$\left(\beta_1(Fbr1,T) - \alpha_1(Fbr1,T)\right)\cdot w1 = \ln\left(\frac{\beta_1(Fbr1,T)}{\alpha_1(Fbr1,T)}\right)$$

$Fbr(T) := Find(Fbr1)$

For Vdeplete<Vbr

$$Vbr(T) := Fbr(T)\cdot\left(w1 + t_{InP} + t_{grading} + t_{undoped}\right) - \frac{q\cdot\sigma 1}{\varepsilon 1\cdot\varepsilon 0}\cdot\left(\frac{t_{InP}}{2} + t_{grading} + t_{undoped}\right) - V_{bi} \cdots$$
$$+ (-1)\cdot\left[\frac{q\cdot N_G\cdot t_{grading}}{\varepsilon 2\cdot\varepsilon 0}\cdot\left(\frac{t_{grading}}{2} + t_{undoped}\right) + \frac{q\cdot\sigma_{InGaAs}}{\varepsilon 2\cdot\varepsilon 0}\cdot t_{undoped} + \frac{q\cdot N_D\cdot t_{undoped}^{2}}{\varepsilon 2\cdot\varepsilon 0\cdot 2}\right]$$

For Vdepleted>Vbr

$$Vbru(T) := Fbr(T)\cdot\left(w1 + t_{InP} + t_{grading}\right) - \frac{q\cdot\sigma 1}{\varepsilon 1\cdot\varepsilon 0}\cdot\left(\frac{t_{InP}}{2} + t_{grading}\right) - \frac{q\cdot N_G\cdot t_{grading}}{\varepsilon 2\cdot\varepsilon 0}\cdot\left(\frac{t_{grading}}{2}\right) - V_{bi} \cdots$$
$$+ \frac{t_{undoped}}{2\cdot\left(\frac{q\cdot N_D\cdot t_{undoped}}{\varepsilon 2\cdot\varepsilon 0}\right)}\cdot\left(Fbr(T) - \frac{q\cdot\sigma 1}{\varepsilon 1\cdot\varepsilon 0} - \frac{q\cdot N_G\cdot t_{grading}}{\varepsilon 2\cdot\varepsilon 0} - \frac{q\cdot\sigma_{InGaAs}}{\varepsilon 2\cdot\varepsilon 0}\right)^{2}$$

$j := 0, 1 .. 10 \qquad T_j := 233 + 10\cdot j \qquad The1_j := Vbr(T_j) \qquad The2_j := Vbru(T_j)$

$j := 11, 12 .. 13 \qquad T_j := 348 + 15\cdot(j - 11) \qquad The1_j := Vbr(T_j) \qquad The2_j := Vbru(T_j)$

expeimental Vbr

$$APD34 := \begin{bmatrix} 60.75 \\ 62.25 \\ 63.6 \\ 65.1 \\ 66.6 \\ 67.95 \\ 69.3 \\ 70.6 \\ 71.8 \\ 73.2 \\ 74.4 \\ 76 \\ 77.6 \\ 79 \end{bmatrix} \qquad APD32 := \begin{bmatrix} 45.9 \\ 47.7 \\ 49.5 \\ 51.15 \\ 52.65 \\ 54.3 \\ 55.8 \\ 57.3 \\ 58.65 \\ 60 \\ 61.5 \\ 63.3 \\ 65.4 \\ 67.05 \end{bmatrix} \qquad APD14 := \begin{bmatrix} 34.6 \\ 36.4 \\ 38.3 \\ 40.2 \\ 41.9 \\ 43.7 \\ 45.3 \\ 46.8 \\ 48.4 \\ 49.95 \\ 51.3 \\ 53.4 \\ 55.2 \\ 57.15 \end{bmatrix}$$

$j := 0, 1 .. 13$

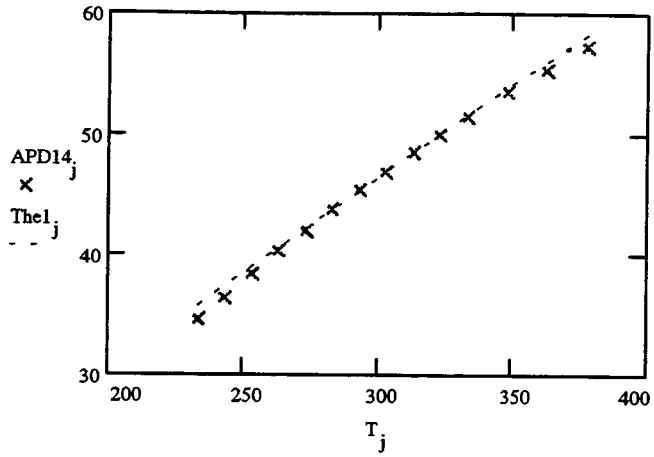

WRITEPRN(tmp) := augment(T, The1) write to the file tmp.prn

References

[1] J. M. Senior, "Optical fibre communications," 2nd edn., Prentice Hall, 1992.

[2] J. C. Palais, "Fibre optic communications," 3rd edn., Prentice Hall, 1992.

[3] J. Gowar, "Optical communication systems," 2nd edn., Prentice Hall, 1993.

[4] K. C. Kao and G. A. Hockham, "Dielectric fibre surface waveguides for optical frequencies," *Proc. IEE*, Vol. 113, pp. 1151-1158, 1966.

[5] R. J. Mears, L. Reekie, I. M. Jauncey, and D. N. Payne, "Low-noise erbium-doped fibre amplifier at 1.54 μm," *Electron. Lett.*, Vol. 23, pp. 1026-1028, 1987.

[6] E. Desurvire, J. R. Simpson, and P. C. Becker, "High-gain erbium-doped travelling-wave fibre amplifier," *Opt. Lett.*, Vol. 12, pp. 888-890, 1987.

[7] B. E. A. Saleh and M. C. Teich, "Fundamentals of photonics," John Wiley, 1991.

[8] H. Beneking, "Gain and bandwidth of fast near-infrared photodetectors: a comparison of diodes, phototransistors, and photoconductive devices," *IEEE Trans. Electron. Dev.*, Vol. ED-29, pp. 1420-1431, 1982.

[9] S. R. Forrest, "Optical detectors: three contenders," IEEE Spectrum, May issue, pp. 76-84, 1986.

[10] C. Rolland, L. E. Tarof, and A. Somani, "Multigigabit networks: the challenge," *IEEE LTS*, May issue, pp. 16-26, 1992.

[11] Y. Akahori, Y. Akastu, A. Kohzen, and J. Yoshida, "10-Gb/s high-speed monolithically integrated photoreceiver using InGaAs p-i-n PD and planar doped InAlAs/InGaAs HEMTs," *IEEE Photon. Technol. Lett.*, Vol. PTL-4, pp. 754-756, 1992.

[12] T. Kaneda, "Silicon and germanium avalanche photodiodes", in W. T. Tsang (ed.), *Semiconductors and semimetals*, Vol. 22D, Academic Press, 1985.

[13] S. R. Forrest, "Optical detectors for lightwave communication," S. E. Miller and I. P. Kaminow (ed.), Optical fibre telecommunications, 2nd ed., Academic Press, 1988.

[14] J. C. Campbell, "Photodetectors for long-wavelength lightwave systems," in C. Lin (ed.), Optoelectronic technology and lightwave communications systems, Van Nostrand Reinhold, 1989.

[15] N. Susa, Y. Mamauchi, and H. Kanbe, "Punch-through type InGaAs photodetector

fabricated by vapor-phase epitaxy," *IEEE J. Quan. Electron.*, Vol. QE-16, pp. 542-545, 1980.

[16] K. Nishida, K. Taguchi, and Y. Matsumoto, "InGaAsP heterojunction avalanche photodiodes with high avalanche gain," *Appl. Phys. Lett.*, Vol. 35, pp. 251-252, 1979.

[17] Y. Takanishi, M. Kawashima, and Y. Horikoshi, "Required donor concentration of epitaxial layers for efficient InGaAsP avalanche photodiodes," *Jpn. J. Appl. Phys.*, Vol. 19, pp. 693-701, 1980.

[18] N. Susa, H. Nakagome, O. Mikami, H. Ando, and H. Kanbe, "Characteristics in InGaAs/InP avalanche photodiodes with separate absorption and multiplication regions", *IEEE J. Quan. Electron.*, Vol. QE-17, pp. 243-250, 1981.

[19] V. Diudiak, S. H. Groves, C. E. Hurwitz, and G. W. Iseler, "Low dark-current, high gain GaInAsP/InP avalanche photodetectors," *IEEE J. Quan. Electron.*, Vol. QE-17, pp. 260-263, 1981.

[20] O. K. Kim, S. R. Forrest, W. A. Bonner, R. G. Smith, "A high gain InGaAs/InP avalanche photodiodes with no tunneling leakage current," *Appl. Phys. Lett.*, Vol. 39, pp. 402-404, 1981.

[21] S. R. Forrest, O. K. Kim, and R. G. Smith, "Optical response time of InGaAs/InP avalanche photodiodes," *Appl. Phys. Lett.*, Vol. 41, pp. 95-98, 1982.

[22] T. Shirai, T. Mikawa, T. Kaneda, and A. Miyauchi, "InGaAs avalanche photodiodes for 1 μm wavelength region," *Electron. Lett.*, Vol. 19, pp. 535-536, 1983.

[23] J. C. Campbell, A. G. Dentai, W. S. Holden, and B. L. Kasper, "Hihg-performance avalanche photodiode with separate absorption, grading, and multiplication regions," *Electron. Lett.*, Vol. 19, pp. 818-820 (1983).

[24] M. Kobayashi, S. Yamazaki, and T. Kaneda, "Planar InP/InGaAsP/InGaAs buried structure APD," *Appl. Phys. Lett.*, Vol. 45, pp. 759-761, 1984.

[25] K. Taguchi, T. Torikai, Y. Sugimoto, K. Makita, and H. Ishihara, "Planar-structure InP/InGaAsP/InGaAs avalanche photodiodes with preferential lateral extended guarding ring for 1.0-1.6 μm wavelength optical communication use," *J. Lightwave Technol.*, Vol. 6, pp. 1643-1655, 1988.

[26] J. C. Campbell, W. S. Holden, G. J. Qua, and A. G. Dental, "Frequency response of InP/InGaAsP/InGaAs avalanche photodiodes with separate absorption 'grading' and

multiplication regions," *IEEE J. Quan. Electron.*, Vol. QE-21, pp. 1743-1746, 1985.

[27] J. C. Campbell, W. T. Tsang, G. J. Qua and B. C. Johnson, "High-speed InP/InGaAsP/InGaAs avalanche photodiodes grown by chemical beam expitaxy," *IEEE J. Quan. Electron.*, Vol. QE-25, pp. 496-500, 1988.

[28] F. Capasso, H. M. Cox, A. L. Hutchinson, N. A. Olsson, and S. G. Hummel, "Pseudo-quaternary GaInAsP semiconductor: A new GaInAs/InP graded gap superlattice and its abdications to avalanche photodiodes," *Appl. Phys. Lett.*, Vol. 45, pp. 1192-1195, 1984.

[29] J. N. Hollenhorst, "High frequency performance of planar InGaAs/InP APDs," in *SPIE Conf. Proc., Vol. 995, High frequency analog communications*, pp. 53-60, 1990.

[30] F. Capasso, A. Y. Cho, and P. F. Foy, "Low-dark-current low-voltage 1.3-1.6 μm avalanche photodiode with high-low electric profile and separate absorption and multiplication regions by molecular beam epitaxy," *Electron. Lett.*, Vol. 20, pp. 635-637, 1984.

[31] P. P. Webb, R. J. McIntyre, J. Scheibling, and M. Holunga, "Planar InGaAs/InP APD fabrication using VPE and Si implantation techniques," in *Opt. Fibre Commun. Conf. 1988 Tech. Digest Series*, Vol. 1, p. 129, 1988.

[32] F. Osaka, T. Mikawa, "Excess noise design of InP/InGaAsP/InGaAs avalanche photodiodes," *IEEE J. Quan. Electron.*, Vol. QE-22, pp. 471-478, 1986.

[33] T. Shiba, E. Ishimura, K. Takahashi, H. Namizaki, and W. Susaki, "New approach to the frequency response analysis of an InGaAs avalanche photodiode," *J. Lightwave Technol.*, Vol. 6, pp. 1502-1505, 1988.

[34] M. Ito, T. Mikawa, and O. Wada, "Optimum design of δ-doped InGaAs avalanche photodiode by using quasi-ionization rates," *J. Lightwave Technol.*, Vol. 8, pp. 1046-1050, 1990.

[35] R. Kuchibhotla, J. C. Campbell, "Delta-doped avalanche photodiodes for high bit-rate lightwave receivers," *J. Lightwave Technol.*, Vol. 9, pp. 900-905, 1991.

[36] L. E. Tarof, D. G. Knight, K. E. Fox, C. J. Miner, N. Puetz, and H. B. Kim, "Planar InP/InGaAs avalanche photodiodes with partial charge sheet in device periphery," *Appl. Phys. Lett.*, Vol. 57, pp. 670-672, 1990.

[37] L. E. Tarof, "Planar InP/InGaAs avalanche photodetectors with n^- multiplication

layer exhibiting a very high gain-bandwidth product," *IEEE Photon. Technol. Lett.*, Vol. PTL-2, pp. 643-646, 1990.

[38] L. E. Tarof, "Planar InP/InGaAs avalanche photodetector with a gain-bandwidth product in excess of 100 GHz," *Electron. Lett.*, Vol. 27, pp. 34-35, 1991.

[39] R. Kuchibhotla, J. C. Campbell, C. Tsai, W. T. Tsang, and F. S. Choa, "InP/InGaAsP/InGaAs SAGM avalanche photodiode with delta-doped multiplication region," *Electron. Lett.*, Vol. 27, pp. 1361-1363, 1991.

[40] L. E. Tarof, J. Yu, R. Bruce, D. G. Knight, T. Baird, and B. Oosterbrink, "High frequency performance of separate absorption grading, charge, and multiplication InP/InGaAs avalanche photodiodes," *IEEE Photon. Technol. Lett.*, Vol. PTL-5, pp. 672-674, 1993.

[41] L. E. Tarof, J. Yu, T. Baird, R. Bruce, D. G. Knight, "Temperature measurements of separate absorption grading, charge, and multiplication (SAGCM) InP/InGaAs avalanche photodiodes (APDs)," *IEEE Photon. Technol. Lett.*, PTL-5, pp. 1044-1046, 1993.

[42] J. Yu, L. E. Tarof, R. Bruce, D. G. Knight, K. Visvanatha and T. Baird, "Noise performance of separate absorption grading, charge, and multiplication InP/InGaAs avalanche photodiodes," *IEEE Photon. Technol. Lett.*, Vol. PTL-6, pp. 632-634, 1994.

[43] R. Chin, N. Holonyak, G. E. Stillman, J. Y. Tang, and K. Hess, "Impact ionization in multilayer heterojunction structures," *Electron. Lett.*, Vol. 16, pp. 467-468, 1980.

[44] F. Capasso, W. T. Tsang, and G. F. Williams, "Staircase solid-state photomultipliers and avalanche photodiodes with enhanced ionization rates ratio," *IEEE Trans. Electron. Devices*, Vol. ED-30. pp. 381-390, 1983.

[45] F. Capasso, W. T. Tsang, A. L. Hutchinson, and G. F. Williams, "Enhancement of electron impact ionization in a superlattice: A new avalanche photodiode with a large ionization rate ratio," *Appl. Phys. Lett.*, Vol. 40, pp. 38-40, 1982.

[46] T. Kagawa, H. Iwamura, and O. Mikami, "Dependence of the GaAs/AlGaAs superlattice ionization rate on Al content," *Appl. Phys. Lett.*, Vol. 54, pp. 33-35, 1989.

[47] F. Osaka, T. Mikawa, and O. Wade, "Electron and hole impact ionization rates in InP/GaInAs superlattice," *IEEE J. Quan. Electron.*, Vol. QE-22, pp. 1986-1991, 1986.

[48] K. Mohammed, F. Capasso, J. Allam, A. Y. Cho, and A. L. Hutchinson, "New high-

speed long-wavelength $Al_{0.48}In_{0.52}As/Ga_{0.47}In_{0.53}As$ multiquantum well avalanche photodiodes," *Appl. Phys. Lett.*, Vol. 47, pp. 597-599, 1985.

[49] T. Kagawa, Y. Kawamura, H. Asai, M. Naganuma, and O. Mikami, "Impact ionization rates in an InGaAs/InAlAs superlattice," *Appl. Phys. Lett.*, Vol. 55, pp. 993-995, 1989.

[50] T. Kagawa, Y. Kawamura, H. Asai, and M. Naganuma, "InGaAs/InAlAs superlattice avalanche photodiode with a separated photoabsorption layer," *Appl. Phys. Lett.*, Vol. 57, pp. 1895-1897, 1990.

[51] T. Kagawa, H. Asai, and Y. Kawamura, "An InGaAs/InAlAs superlattice avalanche photodiode with a gain bandwidth product of 90 GHz," *IEEE Photon. Technol. Lett.*, Vol. PTL-3, pp. 815-817, 1991.

[52] T. Kagawa, Y. Kawamura, and H. Iwamura, "InGaAsP/InAlAs superlattice avalanche photodiode," *IEEE J. Quan. Electron.*, Vol. QE-28, pp. 1419-1423, 1992.

[53] T. Kagawa, Y. Kawamura, and H. Iwamura, "A wide-bandwidth low-noise InGaAsP/InAlAs superlattice avalanche photodiode with a flip-chip structure for wavelength of 1.3 and 1.5 μm," *IEEE J. Quan. Electron.*, Vol. QE-29, pp. 1387-1392, 1993.

[54] Y. Miyamo, K. Hagimoto, M. Ohhata, T. Kagawa, N. Tsuzuki, H. Tsunetsuga, and I. Nishi, "10-Gb/s strained MQW DFB-LD transmitter module and superlattice APD receiver module using GaAs MESFET IC's," *J. Lightwave Tech.*, Vol. 12, pp. 332-342, 1994.

[55] A. G. Chynoweth, "Charge multiplication phenomena," in R. K. Willardson and A. C. Beer (eds.), *Semiconductors and semimetals*, Vol. 4, Academic Press, 1968.

[56] G. E. Stillman and C. M. Wolfe, "Avalanche photodiodes," in R. K. Willardson and A. C. Beer (eds.), *Semiconductors and semimetals*, Vol. 12, Academic Press, 1977.

[57] F. Capasso, "Physics of avalanche photodiodes," in W. T. Tsang (ed.), *Semiconductors and semimetals*, Vol. 22D, Academic Press, 1985.

[58] R. J. McIntyre, "Multiplication noise in uniform avalanche diodes," *IEEE Trans. Electron. Devices*, Vol. ED-1. pp. 164-168, 1966.

[59] R. J. McIntyre, "The distribution of gains in uniformly multiplying avalanche photodiodes: Theory," *IEEE Trans. Electron. Devices*, Vol. ED-19, pp. 703-713, 1972.

[60] P. P. Webb, R. J. McIntyre, and J. Conradi, "Properties of avalanche photodiodes,"

RCA Review, Vol. 35, pp. 234-278, 1974.

[61] J. C. Campbell, B. C. Johnson, G. J. Qua and W. T. Tsang, "Frequency response of InP/InGaAsP/InGaAs avalanche photodiodes," *J. Lightwave Tech.*, Vol. 7, pp. 778-784, 1989.

[62] R. B. Emmons, "Avalanche photodiode frequency response," *J. Appl. Phys.*, Vol. 33, pp. 3705-3714, 1967.

[63] R. Kuvas and C. A. Lee, "Quasistatic approximation for semiconductor avalanches," *J. Appl. Phys.*, Vol. 41, pp. 1743-1755, 1970.

[64] J. N. Hollenhorst, "Frequency response theory for multilayer photodiodes," *J. Lightwave Technol.*, Vol. 8, pp. 531-537, 1990.

[65] G. Kahraman, B. E. A. Saleh, W. L. Sargeant, and M. C. Teich, "Time and frequency response of avalanche photodiodes with arbitrary structure," *IEEE Trans. Electron. Devices*, Vol. ED-39, pp. 553-560, 1992.

[66] B. C. Roy and N. B. Chakrabarti, "Pulse response of avalanche photodiodes," *J. Lightwave Technol.*, Vol. 10, pp. 169-181, 1992.

[67] S. R. Forrest, "Performance of $In_xGa_{1-x}As_yP_{1-y}$ photodiodes with dark current limited by diffusion, generation-recombination, and tunneling," *IEEE J. Quan. Electron.*, Vol. QE-17, pp. 217-226, 1981.

[68] A. Zemel and M. Gallant, "Current-voltage characteristics of MOCVD InP/InGaAs p-i-n photodiodes: the influence of finite dimensions and heterointerfaces," *J. Appl. Phys.*, Vol. 64, pp. 6552-6561, 1988.

[69] N. Susa, H. Nakagome, H. Ando, and H. Kanbe, "Characteristics in InGaAs/InP avalanche photodiodes with separate absorption and multiplication regions," *IEEE J. Quan. Electron.*, Vol. QE-17, pp. 243-250, 1981.

[70] S. R. Forrest, O.K. Kim, and R. G. Smith, "Analysis of the dark current and photoresponse of InGaAs/InP avalanche photodiodes," *Solid-State Electronics*, Vol. 26, pp. 951-968, 1983.

[71] A.S. Grove, "Physics and technology of semiconductor devices," Wiley, 1967.

[72] J. L. Moll, "Physics of semiconductors," McGraw-Hill, 1964.

[73] Y. Liu, S. R. Forrest, J. Hladky, M. J. Lange, G. H. Olsen, and D. E. Ackley, "A Pla-

nar InP/InGaAs avalanche photodiode with floating guard ring and double diffused junction," *J. Lightwave Technol.*, Vol. 10, pp. 182-192, 1992.

[74] P. Webb, R. J. McIntyre, J. Scheibling, and M. Holunga, "Planar InGaAs/InP avalanche photodiode fabrication using vapor-phase epitaxy and silicon implantation techniques," *Proc. Opt. Fibre Commun. Conf. Tech. Series,* Vol. 1, pp. 129-130, 1988.

[75] L. E. Tarof, "Separate absorption, grading, charge, and multiplication avalanche photodiodes," *PH. D thesis*, Carleton University, Ottawa, 1993.

[76] L. E. Tarof, C. J. Minor, and A. J. SpringThorpe, "Epitaxial layer thickness measurement by reflection spectroscopy," *J. Electronic materials,* Vol. 18, pp. 361-365, 1989.

[77] L. E. Tarof, C. J. Minor, and C. Blaauw, "Epitaxial layer thickness measurement of double structures using reflectance spectroscopy," *J. Appl. Phys.*, Vol. 68, pp. 2927-2938, 1990.

[78] C. L. F. Ma, J. M. Deen, and L. E. Tarof, "Device parameters extraction in separate absorption, grading, charge and multiplication InP/InGaAs avalanche photodiodes," submitted to *IEEE Trans. Electron. Devices.*

[79] M. Gallant and A. Zemel, "Long minority hole diffusion length and evidence for bulk radiative recombination limited lifetime in InP/InGaAs/InP double heterostructures," *Appl. Phys. Lett.*, Vol. 52, pp. 1686-1688, 1988.

[80] L. E. Tarof, J. Yu, R. Bruce, D. G. Knight, T. Baird, K. Visvanatha, D. McGhan, B. Emmerstorfer, C. L. F. Ma, C. M. Martian and C. J. Miner, "Design and whole wafer performance of separate absorption, grading, charge, and multiplication InP/InGaAs avalanche photodiodes," in *SPIE Conf. Proc. Vol. 2149, Technol. Optical Communications,* paper #34, 1994.

[81] C. L. F. Ma, M. J. Deen, and L. E. Tarof, "A fast and accurate method of extracting two critical device parameters of separate absorption grading, charge, and multiplication InP/InGaAs avalanche photodiodes," *Proc. 24th European Solid State Device Research Conf.*, 1994.

[82] T. P. Pearsall, "Impact ionization rates for electrons and holes in GaInAs,", *Appl. Phys. Lett.*, Vol. 36, pp. 218-220, 1980.

[83] I. Umebu, A. N. M. M. Choudhur, and P. N. Robson, "Ionization coefficients measured in abrupt InP junctions," *Appl. Phys. Lett.*, Vol. 36, pp. 302-303, 1980.

[84] L. W. Cook, G. E. Bulman, and G. E. Stillman, "electron and hole impact ionization coefficients in InP determined by photomultiplication measurements", *Appl. Phys. Lett.*, Vol. 40, pp. 589-591, 1982.

[85] C. A. Armiento and S. H. Groves, "Impact ionization in (100)-, (110), and (111)-oriented InP avalanche photodiodes," *Appl. Phys. Lett.*, Vol. 43, pp. 198-200, 1983.

[86] F. Osaka, T. Mikawa, and T. Kaneda, "Impact ionization coefficients of electrons and holes in (100)-oriented $Ga_{1-x}In_xAs_yP_{1-y}$," *IEEE J. Quan. Electron.*, Vol. QE-21, pp. 1326-1338, 1985.

[87] J. Conradi, "Temperature effects in Silicon avalanche diodes," *Solid-State Electronics*, Vol. 17, pp. 99-106, 1974.

[88] M. H. Woods, W. C. Johnson, and M. A. Lampert, "Use of a Schottey barrier to measure impact ionization coefficients in semiconductors," *Solid-State Electronics*, Vol. 16, pp. 381-394, 1973.

[89] S. L. Miller, "Avalanche breakdown in Germanium," *Phys. Rev.*, Vol. 99, pp. 1234-1241, 1955.

[90] S. L. Miller, "Ionization rates for holes and electrons in Silicon," *Phys. Rev.*, Vol. 105, pp. 1246-1249, 1957.

[91] G. A. Baraff, "Distribution functions and ionization rates for hot electrons in semiconductors," *Phys. Rev.*, Vol. 128, pp. 2507-2517, 1962.

[92] Y. Okuto and C. R. Crowell, "Energy-conservation considerations in the characterization of impact ionization in semiconductors," *Phys. Rev.*, Vol. 6, pp. 3076-3081, 1972.

[93] C. R. Crowell and S. M. Sze, "Temperature dependence of avalanche multiplication in semiconductors," *Appl. Phys. Lett.*, Vol. 9, pp. 242-244, 1966.

[94] H. C. Casey, Jr. and M. B. Panish, "Heterostructure lasers part B: Materials and operating characteristics," Academic Press, 1978.

[95] C. W. Kao and C. R. Crowell, "Impact ionization by electrons and holes in InP," *Solid-State Electronics*, Vol. 23, pp. 881-891, 1980.

[96] Y. Takanashi and Y. Horikoshi, "Temperature dependence of ionization coefficients for InP and 1.3 μm InGaAsP avalanche photodiodes," *Jpn. J. Appl. Phys.*, Vol. 20, pp. 1907-1913, 1981.

[97] K. Taguchi, T. Torikai, Y. Sugimot, K. Makita, and H. Ishihara, "Temperature dependence of impact ionization coefficients in InP," *J. Appl. Phys.*, Vol. 59, pp. 476-481, 1986.

[98] H. F. Chau and D. Pavlidis, "A physics-based fitting and extrapolation method for measured impact ionization coefficients in III-V semiconductors," *J. Appl. Phys.*, Vol. 72, pp. 531-538, 1992.

[99] C. L. Anderson and C. R. Crowell, *Phys. Rev.*, "Threshold energies for electron-hole pair production by impact ionization in semiconductors," Vol. B5, pp. 2267-2272, 1972.

[100] T. P. Pearsall, *Appl. Phys. Lett.*, "Threshold energies for impact ionization by electrons and holes in InP," Vol. 35, pp. 168-170, 1979.

[101] M. S. Tyagi, "Zener and avalanche breakdown in Silicon alloyed p-n junctions," *Solid-State Electronics*, Vol. 23, pp. 99-128, 1968.

[102] J. Yu, L. E. Tarof, T. Baird, D. McGhan, R. Bruce, D. G. Knight, "Temperature measurements of separate absorption grading, charge, and multiplication (SAGCM) InP/InGaAs avalanche photodiodes (APDs)," in *SPIE Conf. Proc. Vol. 2149, Technol. Optical Communications*, paper #35, 1994.

[103] C. L. F. Ma, M. J. Deen, L. E. Tarof, and J. Yu, "Modelling of breakdown voltage and its temperature dependence in separate absorption, grading, charge, and multiplication InP/InGaAs avalanche photodiodes," *IEDM*, pp. 583-586, 1994.

[104] C. L. F. Ma, M. J. Deen, L. E. Tarof, and J. Yu, "Temperature dependence of breakdown voltages in separate absorption, grading, charge, and multiplication InP/InGaAs avalanche photodiodes," to be published in *IEEE Trans. Electron. Devices*, May, 1995.

[105] R. G. Smith and S. R. Forrest, "Sensitivity of avalanche photodetector receivers for long-wavelength optical communications," *Bell System Technical J.*, Vol. 61, pp. 2929-2946, 1982.

[106] C. L. F. Ma, M. J. Deen, and L. E. Tarof, "DC and noise characteristics of InP-based avalanche photodiodes for optical communication applications," *Proc. 1993 Canadian Conf. Electric. Comp. Engineering*, pp. 1270-1273, 1993.

[107] C. L. F. Ma, M. J. Deen, and L. E. Tarof, "Dark current noise of separate absorption,

grading, charge, and multiplication InP/InGaAs avalanche photodiodes," *European Solid-state Device Research Conference*, pp. 727-730, 1994.

[108] H. Kanbe, G. Grosskopf, O. Mikami, and S. Machida, "Dark current noise characteristics and their temperature dependence in Germanium avalanche photodiodes," *IEEE J. Quan. Electron.*, Vol. QE-17, pp. 1534-1539, 1981.